Enabling Studies on the Effects of Gravity Through Ground-Based Research

The Use and Limitations of the Random Positioning Machine

Lasse Bruun

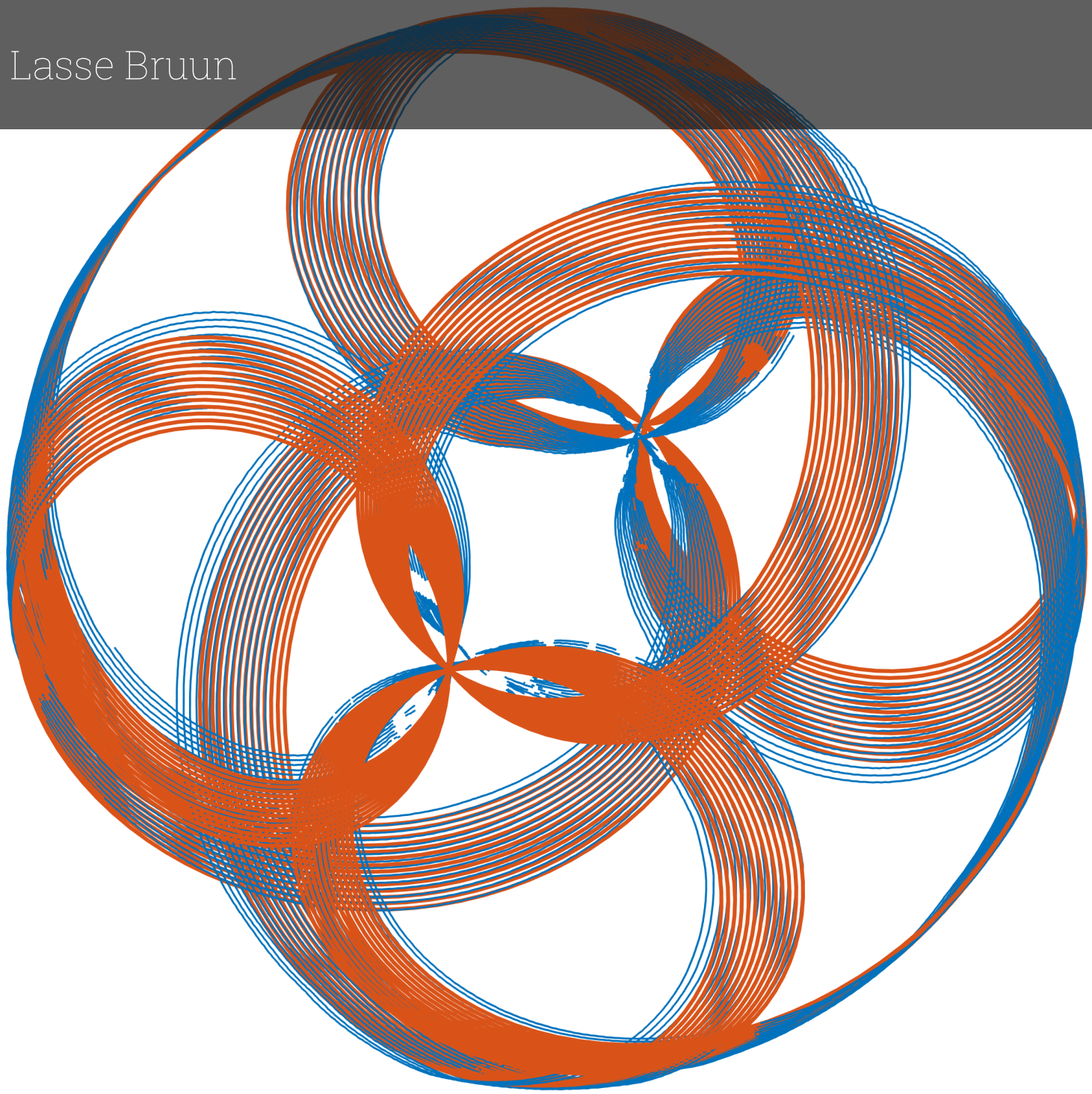

Enabling Studies on the Effects of Gravity Through Ground-Based Research

The Use and Limitations of the Random Positioning Machine

by

Lasse Bruun

in partial fulfilment of the requirements for the degree
Master of Science in Aerospace Engineering
at the
Delft University of Technology, the Netherlands.

To be defended publicly on Friday, December 8, 2023 at 14:00 CET.

Student number:	4676645	
Thesis duration:	March 30, 2023 – November 30, 2023	
Thesis committee:	Prof. L. G. Petersen,	MIT, external supervisor
	Dr. S. Speretta,	TU Delft, internal supervisor
	Dr. J. Heiligers,	TU Delft, chair
	Dr. I. Uriol Balbin,	TU Delft, external committee member

This thesis and its research was written and conducted at the Aerospace Physiology Laboratory at Massachusetts Institute of Technology, USA, under the supervision of Prof. Lonnie G. Petersen.

Cover: Modelled and recorded trajectory of the inner frame of the Random Positioning Machine.

Summary

Access to microgravity and space has given us humans considerable knowledge about our world and has been driving many technological developments. Access to space is limited and crew time to do experiments on board a space station is even more limited. We have therefore developed several other ways in which we can simulate the effects of microgravity and expand our knowledge of the influence of gravity on life. One of these is the Random Positioning Machine (RPM), which can simulate microgravity by rotating two frames and thereby manipulating the gravity vector to point uniformly in all directions and over time gravity will cancel out. This will create a state of simulated microgravity on a system on the RPM if its reaction to gravity is slower than the change in direction of the gravity vector. Other important aspects of the RPM is that it is able to simulate hypogravity levels, such as the Moon or Mars gravity, which can be used in preparation for future manned missions, it can simulate long-duration effects of microgravity, making it possible to conduct studies that alternative platforms might not be able to support.

Even though the RPM has been around for more than 20 years and used across many disciplines, there still exists no exact model to describe its motion and give information on its performance. This thesis answers those questions and allows scientists to better understand the RPM and why it can be said to simulate microgravity from a mathematical viewpoint.

When rotating, additional accelerations will appear and depending on your rotational rate of the two frames and the position of the sample, these will be detrimental to your simulation of microgravity. The expression for the acceleration at any given point *P* in the RPM can be seen in Equation 1. The acceleration consists of five terms, which are the acceleration of the global frame, i.e. gravity on Earth, the contributions of the centripetal, Coriolis and Euler acceleration terms, and the relative acceleration between the point and the global frame, which can be found by applying the same equation again at this new point. Only the final expression is shown and it depends on the rotational rates of the two frames, the position of the sample and the change in rotational rate of the two frames. These terms are all converted to be expressed in terms of the global static reference frame. This model is validated through motion capture recordings and data from two sensors on the RPM.

$$\begin{aligned} {}_G\boldsymbol{a}_P = \boldsymbol{a}_G &+_G [{}_O\boldsymbol{\omega}_I \times ({}_O\boldsymbol{\omega}_I \times_O \boldsymbol{P}_P)]_O +_G [{}_O\dot{\boldsymbol{\omega}}_I \times_O \boldsymbol{P}_P]_O \\ &+_G \boldsymbol{\omega}_O \times ({}_G\boldsymbol{\omega}_O \times_G \boldsymbol{P}_I) + 2\, {}_G\boldsymbol{\omega}_O \times_G [{}_O\boldsymbol{\omega}_I \times_O \boldsymbol{P}_P]_O +_G \dot{\boldsymbol{\omega}}_O \times_G \boldsymbol{P}_I \end{aligned} \tag{1}$$

There are many ways to control the two frames but it is shown that two poles are generated when the outer frame crosses the vertical position. This limits the use of the RPM and can become problematic as you want the highest quality of simulated microgravity by uniformly distributing gravity in all directions. Instead of developing a very advanced algorithm that hinders the outer frame from moving through the vertical position, it is suggested to add a third frame to the structure. This allows for more uniformly distributed gravity and is a simple method to overcome pole bias. Following the same principles for the two-framed RPM, the governing equations for the performance of the three-framed RPM can be seen in Equation 2 to Equation 4.

This new dynamical model of the RPM can help utilise its full potential, making microgravity more accessible to researchers, and allow them to understand some of the limitations of the RPM.

$$
{}_G\boldsymbol{a}_P = \begin{bmatrix} 0 \\ 0 \\ -g \end{bmatrix} + [{}_O\boldsymbol{a}_P]_G + {}_G\,\boldsymbol{\omega}_O \times ({}_G\boldsymbol{\omega}_O \times {}_G\,\boldsymbol{P}_I) + 2\,{}_G\boldsymbol{\omega}_O \times ({}_M\boldsymbol{\omega}_P \times {}_M\,\boldsymbol{P}_P + {}_O\,\boldsymbol{\omega}_P \times {}_O\,\boldsymbol{P}_P) \\
+ {}_G\,\dot{\boldsymbol{\omega}}_O \times {}_G\,\boldsymbol{P}_I \tag{2}
$$

$$
[{}_O\boldsymbol{a}_P]_G = [{}_M\boldsymbol{a}_P]_G + {}_G\,[{}_O\boldsymbol{\omega}_M \times ({}_O\boldsymbol{\omega}_M \times {}_O\,\boldsymbol{P}_I)]_O + {}_G\,[2\,{}_O\boldsymbol{\omega}_M \times ({}_M\boldsymbol{\omega}_P \times {}_M\,\boldsymbol{P}_P)]_O \\
+ {}_G\,[{}_O\dot{\boldsymbol{\omega}}_M \times {}_O\,\boldsymbol{P}_I]_O \tag{3}
$$

$$
[{}_M\boldsymbol{a}_P]_G = {}_G\,[{}_M\boldsymbol{\omega}_I \times ({}_M\boldsymbol{\omega}_I \times {}_M\,\boldsymbol{P}_I)]_M + {}_G\,[{}_M\dot{\boldsymbol{\omega}}_I \times {}_M\,\boldsymbol{P}_I]_M \tag{4}
$$

Contents

Abbreviations

CNES Centre National d'Etudes Spatiales.

DLR German Aerospace Center.

EMG Electromyography.
ESA European Space Agency.
EURECA European Retrievable Carrier.

fps Frames per Second.

HU Hindlimb Unloading.

IMU Inertial Measurement Unit.
ISS the International Space Station.

JAXA Japan Aerospace Exploration Agency.

LEO Low Earth Orbit.

NASA the National Aeronautics & Space Administration.
NCCRD National Centre for Combustion Research and Development.

RPM Random Positioning Machine.
RWV Rotating Wall Vessel.

SANS Spaceflight Associated Neuro-ocular Syndrome.

UAV Unmanned Aerial Vehicle.

VIIP Visual Impairment and Intracranial Pressure.

ZARM Center of Applied Space Technology and Microgravity.

List of Symbols

Sign	Description	Value	Unit
a	Acceleration	-	$\mathrm{m\,s^{-2}}$
g	Earth's gravitational acceleration	9.81	$\mathrm{m\,s^{-2}}$
l	Trajectory of a defined point	-	-
$\boldsymbol{P}$	Vector from centre of rotation to point P	-	m
R	Rotational matrix	-	-
t	Time	-	s
V	Velocity	-	$\mathrm{m\,s^{-1}}$
Ω	Angular velocity of a reference frame	-	$\mathrm{rad\,s^{-1}}$
α	Angular acceleration	-	$\mathrm{rad\,s^{-2}}$
η	Factor to weigh the rotation rate towards a certain direction	-	-
μ	Mean	-	-
ω	Angular velocity	-	$\mathrm{rad\,s^{-1}}$
σ	Angle between the middle and outer frame or the outer and global reference frame	-	rad
τ	Angle between the outer frame and the global reference frame	-	rad
θ	Angle between inner frame and outer or middle frame	-	rad

1

Introduction

The next big step for human exploration is to again set foot on the Moon before going to Mars. Such long travels affect human physiology and injure astronauts' health even after returning to Earth. One example of this is Spaceflight Associated Neuro-ocular Syndrome (SANS), which was reported in 2011 as Visual Impairment and Intracranial Pressure (VIIP) syndrome [1] and is seen as a crucial research area before sending humans to Mars [2]. Studies have since the discovery indicated that some damages to the brain and eye structure induced during long-term spaceflight may only be partially reversible upon return to Earth [3]–[5]. Research in SANS not only holds the promise of enabling manned missions to Mars but also extends its benefits to our terrestrial lives. The development of visual assessment techniques and machine learning algorithms within SANS research can be harnessed to enhance eye screenings for individuals on Earth, presenting a more cost-effective approach. This holds tremendous potential to improve early detection and enhance patient outcomes of conditions such as diabetic retinopathy, glaucoma, or age-related macular degeneration [6]. By utilizing the mobile, cost-effective assessment techniques developed for SANS, it can be possible to detect and prevent these vision impairments that affect millions of people on Earth, leading to improved quality of life with better visual health.

Leveraging the advancements made in SANS research paves the way for a healthier future, benefiting both life on Earth and our ambitious explorations beyond our own planet's boundaries. However, the neuro-ocular system is not the only system affected by the lack of gravity. Astronauts experience changes to a large variety of systems including the cardiovascular system, the immune system, the musculoskeletal system, the hematologic system and the gastrointestinal system to name a few [7]. These changes can be related to diseases on Earth and studying them can help develop therapies for bone-related diseases, rehabilitation techniques for muscle-related injuries and diseases, lead to improved treatments of heart-related conditions and advancements in immunology for the benefit of the people on Earth. The unique feature of space, that creates these exceptional opportunities, is microgravity. Not only does it affect human physiology, but it actually seems to accelerate the ageing of the human body [8]. This can be exploited to study age-related diseases at a much higher pace.

Technological developments constantly drive new and improved research, such as microphysiological systems, also known as "organs-on-chips" or "tissue chips", which offer some advantages to study human physiology compared to 2D cell culture systems and animal models [9]. These systems are developed specifically so diseases can be studied in space to improve life on Earth and are a manifestation of the usefulness of microgravity for humans on Earth. The progression in organoid research and stem cell cultures also serves as a good platform to study human physiology in reduced gravity. Access to space is very limited and can be costly both regarding time and money. Hence, instead of looking up towards space only, what if we used ground-based facilities to accommodate even more studies, increasing the research sample size and research output through cheaper and more accessible options? As global life expectancy continues to rise and the average age of the human population increases, the significance of cardiovascular and age-related diseases is progressively amplified, as millions of lives

are restricted by these health conditions. Understanding how we can mimic the effects of gravity, and the lack thereof, therefore becomes crucial not only in preparation for our next big adventure to the Moon and beyond but also for our daily lives on Earth.

Conducting extensive studies on board the the International Space Station (ISS) faces significant constraints, primarily due to cost limitations and limited availability, but also due to the very small sample size. In light of these challenges, it becomes imperative to explore alternative platforms for advancing our knowledge of gravity's effect on life.

Being able to perceive these effects and understanding our possibilities for manipulating gravity provide an exceptional basis for studying a large variety of diseases and phenomena at a much higher pace than ever before. This accelerated pace holds the promise of significantly expediting our pace of discovery beyond what was previously achievable. It is therefore essential to understand which platforms are available to study the effects of gravity and their potential contributions to future studies related to gravity.

While certain platforms can provide access to microgravity, fewer still offer the capability to simulate hypogravity levels akin to those found on the Moon or Mars. These few platforms therefore provide immense importance as they not only support the safe exploration of the Moon and Mars but also significantly enrich our understanding of the gravity dose-response relationship on terrestrial phenomena. One of the most promising platforms remains the Random Positioning Machine (RPM), which can simulate required gravity levels and has a long history of use. Not only is it possible to study various gravity levels, the RPM also allows for long-duration studies as its constant rotation improves the simulated gravity level. In relation to long-duration studies, opportunities in real microgravity are especially scarce. Limited crew time or costly satellite missions can stop experiments that otherwise could have revealed interesting aspects of gravity.

In preparation for the Gateway space station orbiting the Moon, life support systems need testing. During operation, astronauts will be present only in periods, whereas at other times there might not be any humans on board and some life support systems can be switched off. Designing experiments to evaluate the impact of extended periods of system inactivity is a challenge given the limited crew time available on the ISS. In this regard, the RPM offers a practical solution for conducting initial tests on these critical systems, ensuring their reliability and functionality even after long periods of inactivity of the systems.

A different area where the RPM can also be used, is in cell-based therapy and tissue engineering. The unique feature of dispersing gravity uniformly in all directions provided by the RPM has enormous potential for new cell therapy developments and advancements in translational medicine. This has already been shown for osteoarthritis therapy [10], where scaffold-free chondrocyte spheroids were derived, but can potentially be extended to other cell-based therapies and scaled to be more commonly used. The RPM has for example also been shown to be used for bone tissue [11] and holds the potential for new techniques in translational regenerative medicine.

Yet, it remains unknown how the RPM can be scaled and there exists no dynamical model of the RPM explaining its movement, and the related gravity level and trajectory of the gravity vector. These two performance parameters are crucial to understanding how the use of the RPM can be expanded and optimised to improve life on Earth. Considerable benefits can be achieved in preclinical trials either in combination with organ-on-chips in pharmacology or through cell-based therapy in tissue engineering. The utilization of the RPM can reduce the need for animal trials in the future. However, benefits can also come from ongoing cancer research, where RPMs are already used, or through enhancing our knowledge of the effects of gravity on human physiology. The work in this thesis will serve as a key to unlock new possibilities for the utilization of the RPM, extending its applications beyond its traditional role, and be the next step towards controlling gravity to enhance research on the surface of Earth. This thesis introduces a range of novel perspectives on the RPM, aimed at broadening its capabilities and facilitating its adoption across various scientific domains, thereby democratizing access to gravitational research in the hypogravity regime.

Chapter 2 outlines the available platforms we have to perform gravitational research. This literature

study results in choosing to further study the RPM. A short introduction to its history is outlined together with the research questions at the end of this chapter. The kinematic model of the RPM together with information on the experimental setup are described in Chapter 3. The following chapter, Chapter 4 covers the analysis and validation of the model. It is then used to evaluate different control algorithms in Chapter 5. This covers both previously used but also newly developed algorithms. In this chapter, the problem of pole bias is discovered and suggestions on how to overcome this problem is suggested. This is followed by the results on the sizing and lowest resulting g-levels in Chapter 6. Finally, this thesis is completed with a discussion and conclusion in Chapter 7.

2

Platforms for Gravitational Research

Our world transformed with the launch of Sputnik 1. In an instant, our perspective on life shifted, extending far beyond Earth's immediate surface. With this historic launch, we gained access to an entirely unique environment, one we invested heavily in mastering over the ensuing years. Since then, our presence in space has expanded, leading to significant research endeavours that have enriched life on Earth. However, space exploration comes at a steep cost, and our capacity for it remains limited. Therefore, it becomes increasingly beneficial to explore alternatives for simulating the effects of weightlessness. In the following pages, various methods will be explored for replicating the effects of weightlessness here on Earth and are divided into free fall environments in Section 2.1 and ground-based simulations and analogues in Section 2.2.

2.1. Free Fall Environments

There are two distinct categories in which platforms for microgravity studies can be placed. The first is within the free-fall environment and the second is ground-based analogues and simulations. As the name implies, one will have actual free fall conditions while the other uses analogues and simulations to achieve the effects of microgravity. The free fall environments cover orbital flights, suborbital flights, sounding rockets, parabolic flights, drop towers and Unmanned Aerial Vehicles (UAVs), which are presented in this order.

2.1.1. Orbital Flights

There are primarily two different types of orbital flights available for performing gravity-related research. Automated experiments can be designed for use on satellites or experiments can be carried out on a space station where there is a possibility of direct human interaction. There are very different restrictions and requirements related to each of these platforms, and for some studies, one might be preferred over the other.

Of the space stations, the ISS has proved to be a very important platform for research. Since 1999 more than 3600 scientific papers by more than 6000 researchers across the world have been published, all emerging from the research conducted on board the ISS [12]. All this research has benefited both life in space and on Earth, however, the availability and cost of sending experiments to space for the crew to perform are limiting factors in many cases. Experiments meant for the space station need to follow both mass and volume requirements, time constraints both before launch and regarding crew time, environmental requirements and limited availability for returning of experiments [13], which makes Earth analogues more attractive to many researchers.

There is a significant amount of hardware and facility-class payloads on board the ISS that can be used for a wide range of research purposes. From the *Minus Eighty Degree Laboratory Freezer for the ISS* to the *Fluids and Combustion Facility* and from the *Window Observational Research Facility* to the *Multi-use Variable-g Platform* [14]. The latter can be used to study a variety of g-levels up to $2g$, which

allows to have control samples that experience the same loads and stresses during launch and landing. Facilitating the generation of artificial gravity was implemented in the Mouse Habitat Cage Unit that can be installed in the Centrifuge-Equipped Biological Experiment Facility. Here rodents can experience artificially created $1g$ simultaneously with another group experiencing microgravity. That allows for both groups to encounter the same stresses during launch and landing, and only differ between microgravity and artificial $1g$ environment on board the ISS [15], [16].

The second orbiting platform is based on satellites, where experiments must be automated to some extent as human interaction is limited to the communication type of that specific satellite. There exist different kinds of satellites that can be used for research from the Russian FOTON satellite to CubeSats. Originally developed as a platform for technology demonstration and biological experiments, the CubeSats offer a valuable asset when looking at future missions in deep space. Biological CubeSats have been used since the GeneSat-1 in 2006 but the selection of the biological material can be limited by the prelaunch procedures [17]. However, this platform is being considered as an option to go beyond Low Earth Orbit (LEO), which is especially useful for research related to future manned missions to the Moon and Mars [18]. The main difference going from LEO to deep space is the amount of radiation present. In deep space, there will no longer be any protection generated by Earth's magnetic field and the van Allen belt but instead, experiments will be subjected to ionisation by high-energy particles. The new BioSentinel 6U CubeSat is an attempt to go beyond LEO and investigate the frequency of DNA double-strand breaks and the efficiency of their repair by studying the budding yeast *Saccharomyces cerevisiae* [19]. Once leaving LEO, new perturbations become relevant for the overall acceleration level in the vehicle. When increasing the orbit and moving further from the Earth, the solar radiation stays almost constant whereas other perturbations to the acceleration level decrease such as the aerodynamic perturbations, the magnetic disturbances and the perturbations due to the gravity gradient. This means the solar radiation pressure becomes the most dominant external perturbation already in a geosynchronous orbit. The final value depends on the spacecraft and its area but on the European Retrievable Carrier (EURECA) the solar radiation accounted for a disturbance of $2 \cdot 10^{-8} g$ [20]. Other examples of satellites include the Russian FOTON satellites and their Bion satellite program, which has sent both rats and monkeys into orbit [21]. The microgravity level of the FOTON satellites did not exceed $10^{-5} g$ [22].

With the growing interest in space tourism, another alternative platform for microgravity research could be SpaceX's orbital flights. This allows three days in microgravity, with the potential to include research on the flight. This provides a longer duration of microgravity compared to suborbital flight but might be more accessible in the future compared to the ISS.

2.1.2. Suborbital Flights

In recent years, there has been a development and increase in the options for suborbital flights due to the interest in space tourism. The main use of manned suborbital flights is to allow people to experience microgravity and see the Earth from an increased height however, it also opens up a platform for new research related to microgravity. Companies such as Virgin Galactic and Blue Origin but also companies like Masten Space Systems, Exos Aerospace and UP Aerospace can all provide operations with suborbital flights based on rockets [23]. The benefits of Virgin Galactic and Blue Origin are that they support humans on suborbital flights. This means it will be possible to access the experiment during the flight, while they will also be retrievable shortly after landing, within 8 hours for Blue Origin's New Shephard [24]. However, it might be more cost-efficient to design an experiment that does not need any interaction with people, which means that humans will not necessarily be on board these flights. In that case, it is possible to use any of the aforementioned companies to reach microgravity for several minutes. The flights reach a height of around $85 - 120$ km above the surface of the Earth before returning back to the surface. The maximum loads during a flight can be as low as $5g$ based on a nominal New Shephard Flight Profile [24].

The increased duration of microgravity compared to parabolic flights can be useful in certain cases, for example when an equilibrium in fluids takes longer than 35 s. Other improvements are the reduced g-jitter compared to parabolic flights through the atmosphere that causes minor variations in g-level, and their relatively low cost making it an option for testing propellant components [25]. The components can be placed on the booster and initiated after separation, which allows no interference towards the

crew capsule while providing access to the ambient conditions. It is even possible to use the capsule as a centrifuge to simulate lunar gravity [26]. The g-jitter term summarises the disturbing accelerations that occur due to external or internal perturbations. These can arise due to the atmosphere, movement of people inside, manoeuvers, or vibrations from instruments.

Suborbital flights have been used to investigate how plant transcriptomes are affected in microgravity, with different gravity profiles both leading up to microgravity and after. The different gravity profiles resulted in different responses to stimuli, variations in light reaction and photosynthesis among other things. However, also some similarities were spotted across the different flight types including e.g. oxidative stress and regulation of central carbon [27]. For this a Virgin Galactic flight, a Blue Origin flight, a parabolic flight and a flight with an F-104 Starfighter were compared, their flight profiles can be seen in Figure 2.1. Suborbital flights can also serve as a step towards orbital flight for experiments. As a way to progressively understand the challenges of a wax-based hybrid chemical propulsion system, experiments were first performed at parabolic flights, then suborbital flights and finally on board the ISS [28]. This illustrates the applicability of suborbital flights acting as a natural step towards orbital flight.

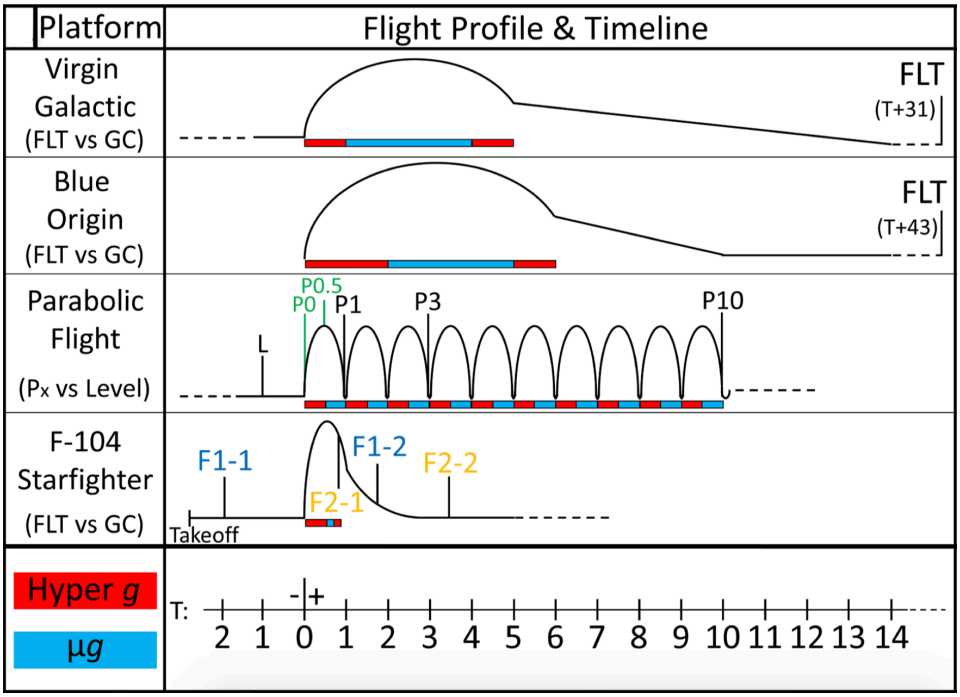

Figure 2.1: Flight profiles of various free-fall flights [27].

2.1.3. Sounding Rockets

The first time sounding rockets were used in microgravity research was in the mid-1970s when the National Aeronautics & Space Administration (NASA) started its Space Processing Applications Rocket program. Around the same time, Germany initiated the TEXUS program, which European Space Agency (ESA) has been using since the 1980s as a more cost-effective tool in developing and preparing experiments for orbital research laboratories. The TEXUS platform was used for material and fluid sciences, and later also biological experiments [29]. Today, sounding rockets still make a valuable platform for research with 18 launches in 2022 by NASA and 174 launches since 2012 [30]. A wide range of rockets is available from ESA, NASA and Japan Aerospace Exploration Agency (JAXA) with NASA's most powerful rocket being able to reach an altitude of around 1500 km with a 114 kg payload [31] to ESA MAXUS that can reach 700 km with a 700 kg payload [32] and JAXA's most powerful SS-520 that can reach 800 km with a 140 kg payload [33].

Sounding research rockets are similar to suborbital flights however, they can reach longer durations of microgravity of up to 20 min [34] but do not support humans. This impacts the safety requirements for experiments, that are less stringent. The experiments can also be accessed up until 1 hr before launch,

allowing more time-sensitive experiments to be performed with this platform. The experiments will also be available around 1 hr after touchdown. However, during reentry 40 to $50g$ can be expected with the German Aerospace Center (DLR) TEXUS and MAXUS sounding rockets, whereas this value is around $13g$ during launch [35]. This exceeds tolerable g-levels for human involvement, and generally sounding rockets have a rougher landing than suborbital flights.

Gravity levels of $\leq 10^{-4}g$ can be achieved for a payload up to a size of 64 cm in diameter. The experiments on board can be operated and monitored using the accompanying telemetry and telecommand support. This makes it possible to e.g. add substances during an experiment. It is possible to control both the temperature and pressure in the experimental payload area. A time frame of around six months to three years from the experiment has been approved to launch with an ESA rocket can be expected [35]. Sounding rockets can be a more cost-effective alternative to biosatellites and other orbital flights [36], and open up for experiments with less stringent safety requirements. The specific missions are designed in collaboration with the researcher's goals, which leads to new possibilities and makes sounding rockets a very agile platform [37].

2.1.4. Parabolic Flights

Experiencing weightlessness close to the surface of the Earth can be achieved by parabolic flights. After pulling up in a hypergravity manoeuvre, the pilot can pull down to make the aircraft enter a parabolic trajectory in which low levels of gravity are achieved. When pulling up, another parabola can be achieved. Usually, $10-40$ parabolic manoeuvres are completed during one flight. Each reduced gravity manoeuvre is preceded and followed by hypergravity of around $1.8g$. The reduced gravity environment lasts for $20-30$ s and allows verification of technological advancements as well as giving insight into some physiological phenomena happening in this gravity regime [38]. The first 30 parabolic flight campaigns by ESA can be divided into physical science experiments, combustion physics, cosmic and atmospheric physics, plasma crystal physics, material science experiments, life science experiments and technology tests [39]. From this list, it is clear that parabolic flights are a diverse platform which allows research in a reduced gravity environment of many different disciplines.

Aircraft of various sizes can be used for parabolic flight manoeuvres as shown in Table 2.1, which contains a list of operators and their platforms. The acceleration levels in parabolic flights are not entirely zero due to turbulence and vibrations, but it shows a microgravity environment close to real microgravity. In a parabolic flight, gravity levels of about $10^{-2}g$ can be achieved for experiments attached to the floor, whereas free-floating experiments experience $10^{-3}g$ [40]. However, it is also possible to change the inclination of the aircraft during the parabolic movement and thereby reach Moon or Mars gravity levels. This has been done to, for example, evaluate the traction of planetary rovers [41].

Table 2.1: Parabolic flight operators [42], [43].

Operator	Platform	Maximum altitude (ft)
Canadian Space Agency/National Research Council	Falcon-20	20,000
Ecuadorian Civilian Space Agency/Ecuadorian Air Force	T-39 Sabreliner	16,000
European Space Agency/CNES/Novespace (France)	Airbus A310	28,000
Roscosmos (Russia)	Ilyushin Il-76	30,000
Universitat Politecnica de Catalunya/Aero Club Barcelona Sabadell (Spain)	Mudry CAP 10B	3,800
Zero Gravity Corporation (USA)	Boeing 727	32,000
Swiss Air Force	F-5E Tiger II	27,000
Pauls Parabelflüge (Austria)	Cessna Grand Caravan	-
Delft University of Technology/the Dutch National Aerospace Laboratory (the Netherlands)	Cessna Citation II	42,000
Diamond Air Services (Japan)	MU-300	-

Three pilots operate Novespace's parabolic flights concurrently. One is in charge of the pitch of the aircraft to control the parabolic trajectory, the second pilot keeps the aircraft level by focusing on the roll angle. The job of the third pilot is to regulate the throttles and monitor flight parameters [44].

A great advantage of parabolic flights is the ability for researchers to be on board and being able to make small adjustments to the experimental set-up between parabolas. This is also one of the reasons it is useful for physiological studies, as test subjects can take part in the flight campaign. Typically, a flight campaign stretches over three days with around 30-40 parabolas over the course of 4 hours. After a few parabolas, there is a break of 4-8 min with a constant $1g$ to evaluate the experiment and make corrections, then more parabolas will be performed [22]. These breaks can be adjusted to match certain experimental requirements. Integration of the experiments begins up to two weeks prior to the test days and includes safety meetings. The test area depends on the aircraft but can be significant on the bigger ones such as the A310. ESA, DLR and the French space agency Centre National d'Etudes Spatiales (CNES) support up to six flight campaigns per year, and usually it takes 8 months from proposal to flight.

2.1.5. Drop Tower

The last research platform to generate the sensation of weightlessness through a free-fall environment is the drop tower. Several towers around the world exist, which can be used to achieve weightlessness for a short duration. The Bremen Drop Tower can provide 4.7 s of weightlessness a maximum of three times a day. Using the catapult mode, which launches the experiment upward before it falls back down, allows for weightlessness for 9.3 s [45]. The capsule in the tower is 800 mm in diameter and 2.4 m tall and can support more than 200 kg [22]. The experiment can be accessed up until two hours before the drop and is available 45 min after the drop. NASA's Zero Gravity Research Facility can provide 5.18 s of weightlessness during a 132 m fall no more than twice every day [46]. The number of drops per day is limited by the time it takes to prepare the test tube or shaft to the correct pressure. In order to achieve gravity levels in the order of $10^{-6}g$ the tubes or shafts have very low pressures to minimise aerodynamic forces. Increasing the height of a drop tower is not the best way to increase the time of weightlessness. Doubling the height of the fall will increase the time in weightlessness by only a factor of $\sqrt{2}$, whereas using the catapult mode will double the time in weightlessness [47].

At the Bremen drop tower, 20 experiments per year are achievable with around 400 drops in total. It takes between 4 weeks and 12 months from contact with the drop tower to run the experiment and the experiments must be able to handle $100g$ during the deceleration phase. Launching with the catapult system generates around $30g$, whereas a simple drop manoeuvre only goes from $1g$ to $0g$ [35]. Two various approaches are taken to reach low gravity levels. Either the tube/shaft can be evacuated, which is a significant time constraint or a capsule in a capsule approach can be adopted. This last approach allows the inner capsule to fall relative to the outer and experience fewer aerodynamic forces in a low-pressure environment.

However, the limited number of drops per day has led to the development of the new GraviTower at the Center of Applied Space Technology and Microgravity (ZARM) at the location of the Bremen drop tower. This new drop tower was inaugurated in 2022 and does not require a vacuum chamber as it utilises an airtight slider accelerated by a hydraulic winch, enabling a significant increase in the number of drops in a day. With only 45 s between flights, up to 1000 flights can be achieved in one day. This allows more repetitions of experiments at a faster time scale, leading to larger data sets. Microgravity is achieved for a couple of seconds, but the acceleration and deceleration can be adjusted to the experimental set-up and can be as low as $2g$. Unlike the Bremen tower, it is possible to access an experiment immediately after the drop [48]. The GraviTower can also be programmed to simulate hypogravity levels such as those encountered on the Moon or Mars. The gravity levels can vary from 0.1 to $0.4g$ [49]. As mentioned, several drop towers exist across the world. A small list of drop towers is presented in Table 2.2. The number of operating drop towers changes as some universities or research institutes build their own while others decommission theirs. These are typically smaller in size and provide microgravity in a duration of less than 2.5 s. A newly built drop tower at Leibniz University Hannover uses a linear electric drive and brake system to control the acceleration level of a vertically movable vacuum chamber, which contains the experiment in a partial vacuum inside. This yields high repetition rates and very low gravity levels of $10^{-6}g$ [50]. Automatic adjustment of the experiment between runs allows for optimised use,

as the evacuation of the vacuum chamber is not required. If manual changes of the experimental set-up are needed between two runs on the drop tower, 1-2 hr for evacuation is required [51], which is in contrast to the drop tower at ZARM, which readily allows to perform changes to the experimental set-up between drops. This method, featuring a linear electric drive and brake system, has inspired NASA to improve their drop towers with the new Electro-Motive Drop Tower, utilising this new technique to increase the number of runs per day and accommodate hypergravity levels. Once completed, the new drop tower should provide microgravity for up to $10\,$s at $10^{-5}g$, support gravity levels up to $0.5g$ and increase the number of runs to 20 runs per day [52].

Table 2.2: Drop tower facilities.

Operator	Country	Microgravity duration	Microgravity quality [g]	Tests per day
Bremen Drop Tower (ZARM)	Germany	$9.3\,$s	10^{-6}	3
GraviTower (ZARM)	Germany	$2.5\,$s	10^{-6}	1000
Leibniz University Hannover [53]	Germany	$4\,$s	10^{-6}	300
Zero Gravity Research Facility (NASA) [46]	USA	$5.18\,$s	$<10^{-5}$	2
2.2 Second Drop Tower (NASA) [54]	USA	$2.2\,$s	10^{-3}	12
Portland State University [55]	USA	$2.1\,$s	$<2\cdot^{-4}$	-
Queensland University of Technology [56]	Australia	$2.0\,$s	$<10^{-4}$	10-15
Hokkaido Aerospace Science and Technology Incubation Center [57]	Japan	$2.3\,$s	10^{-3}	-
National Microgravity Laboratory, Chinese Academy of Science (NMLC) [58], [59]	China	$3.5\,$s	$<2\cdot10^{-4}$	2-4
NCCRD [60]	India	$2.5\,$s	$\leq 10^{-4}$	8-10

2.1.6. Unmanned Aerial Vehicle

Finally, it can be mentioned that very recent developments have been made in developing a new system that utilises the abilities of UAV. Using a drone to raise a platform for microgravity research, and releasing the platform, will generate 5-$12\,$s of microgravity and can be performed multiple times every day. This is a new platform to simulate microgravity that is expected to be introduced commercially in 2023 [61]. It is not reported what gravity levels are achieved during operation or if hypogravity levels can be established for experiments.

Another method is to use the UAVs themselves as a platform with a small payload containing the experiment. The UAVs follow a flight path inducing a microgravity environment on an experiment aboard based on the same steps as a drop tower. An initial period is used to accelerate the UAV, and then a microgravity period occurs where the UAV enters a parabolic movement while counteracting the aerodynamic forces to ensure microgravity level, this is followed by the braking phase and landing. UAVs can be used in more places than drop towers, making them more flexible, however, this method is still in its early stages and has not been used to successfully generate a microgravity environment for research purposes yet. The size of an experiment is very limited by the size of the UAV and the payload it can bring. Together with the controls only being able to control one direction, allowing disturbances such as wind gusts and aerodynamic forces to affect the overall quality of the gravity level, which can reach around $10^{-2}g$ for $1.6\,$s [62]. Further work is needed before this method can be used for microgravity research.

An overview of the discussed free-fall platforms and their microgravity quality and duration can be seen

in Figure 2.2.

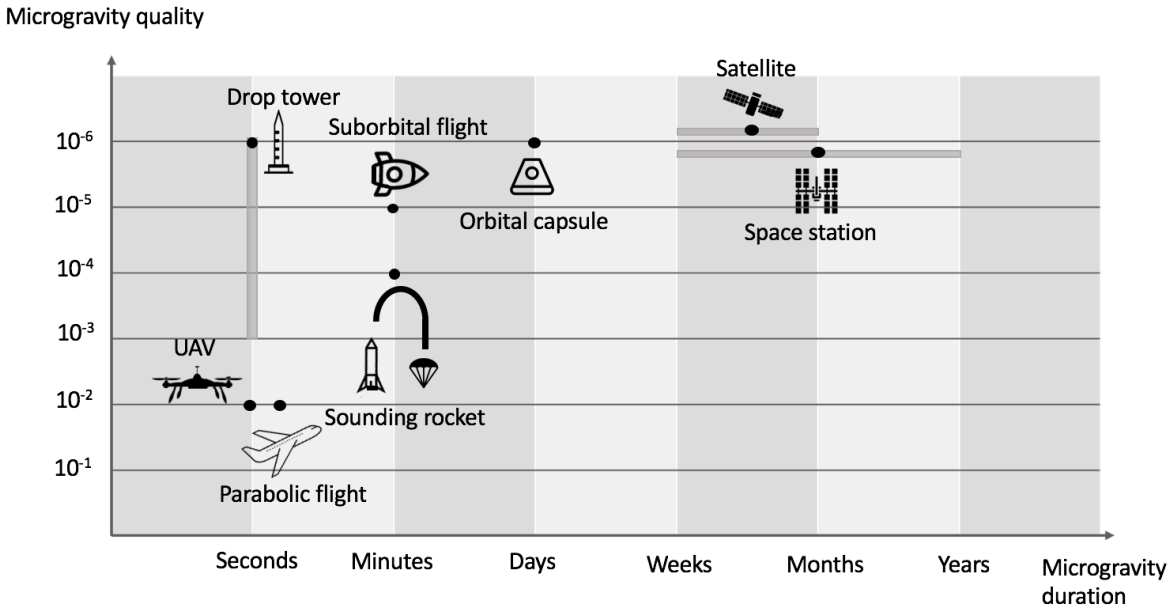

Figure 2.2: Overview of the various platforms to experience free-fall.

2.2. Ground Based Simulations

The ground-based simulations all have in common, that gravity is not removed, rather it is manipulated in a way that simulates certain effects similarly to true microgravity. This can either be done through analogues or by simulating microgravity through rotation or the use of magnets. There can be great benefits in these methods as experiment duration can be longer while using more accessible technologies at a lower cost.

2.2.1. Head Down Tilt Bed Rest

Bed rest studies are associated with the simulation of the inactivity of the muscles during microgravity. The studies can be extended by introducing a head-down tilt of 6° in order to simulate the cephalad fluid shifts seen in space, which is visualised in Figure 2.3. Human adult subjects are used for up to one year to study the musculoskeletal and cardiovascular systems. This includes studies on bone loss, muscle and cardiac atrophy, orthostatic intolerance, and reduced muscle strength and exercise capacity. Depending on what is being studied and the duration of the study, it can take 1 or even up to 2 years to fully recover [63].

The head-down tilt bed rest is however not an ideal simulating platform. The arterial pressures and fluid shifts are similar to those in space due to the head tilt, but gravity will still affect the body on Earth. This means that there will be compression on the surface of the skin where the person lies down, as well as the inside of the body will still experience the weight from the chest pressing towards the back, introducing compression over a large part of the body tissue, which will not naturally occur in space.

In a study on the effects of spaceflight on the brain structure using grey matter maps, 27 astronauts were scanned with T2-weighted MRI scans [64]. These results were compared to a bed rest study. In general, the findings were similar in terms of the distribution of grey matter in the brain scans but there were also differences in the observed grey matter changes in the cerebellum. This indicates that some effects might be similar between real spaceflight and bed rests on the brain structure, whereas the two methods also impose unique changes that the other one does not introduce.

Changes in optical coherence tomography caused by the cephalad fluid shifts, in relation to a study on SANS, have been spotted in head-down tilt bed rest studies as well as in spaceflight studies [4]. This

indicates that head-down tilt studies are reasonable analogues to studying cephalad fluid shift-induced changes.

Although it is a reasonable simulator for bone loss, muscle and cardiac atrophy, orthostatic intolerance, and reduced muscle strength and exercise capacity, previous studies have contributed to many developments and testing of countermeasures for maintaining the health of astronauts in space. This method has proven to be a less reliant simulator for other long-term spaceflight-induced changes when it comes to spinal dysfunction and radiation hazards [63].

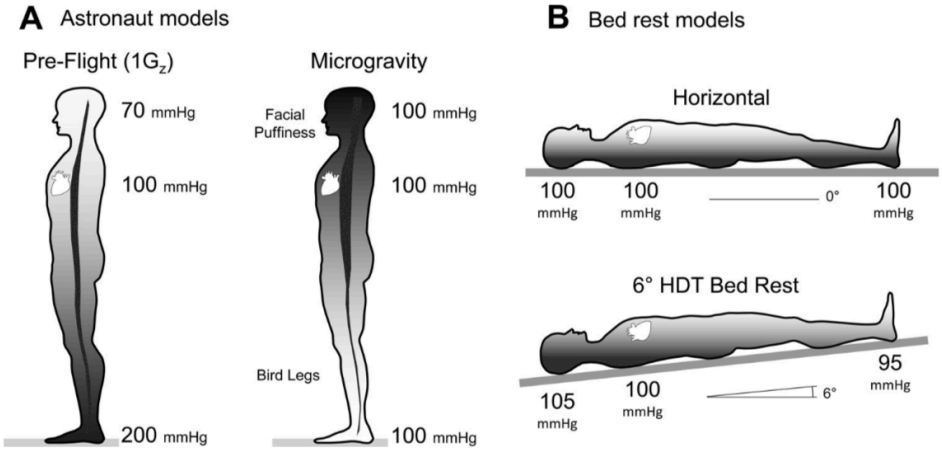

Figure 2.3: Hypothetical blood pressures in the human body of **A:** astronauts on ground and in space and **B:** participants of a bed rest experiment [63].

2.2.2. Wet and Dry Immersion

Wet and dry immersion build on the same principle: the former was developed in the early days of human spaceflight but it proved uncomfortable to stay in the water for extended periods of time [65]. Based on this fact, wet immersion is mainly used for short-duration studies of less than 24 hrs. For longer-duration studies, dry immersion is used. This is a method developed in Russia where the test subjects are immersed in thermoneutral water covered with an elastic waterproof fabric [66]. Both wet and dry immersions are depicted in Figure 2.4. It is furthermore mentioned that immersion analogues do not act as a supporting structure for the body, unlike the bed rest analogues, which is one of the most important differences between these analogues. This means the compression of the body skin mentioned earlier does not appear here. The duration of the two types of studies also differ. The longest dry immersion has been 56 days whereas the longest bed rest study lasted 370 days. Some of the same effects can be seen in both head-down tilt bed rests and dry immersions, however, the intensity and rate of neuromuscular changes are much more rapid in the dry immersion analogue compared to the bed rest analogue [66].

At the beginning of the experiments in dry immersion, the subject feels comfortable but after 2-3 days their heads start feeling heavy and nasal congestion may be observed and is suggested to be caused by cephalad fluid shift [68]. Countermeasures studied with dry immersions are generally passive, whereas countermeasures studied in bed rest studies are more related to diet or fluid shift [69] and exercise countermeasures.

When looking at the reviews, dry immersion is a reasonable analogue to simulate microgravity, however, most of the studies have historically been conducted by Russians or in Russia, and only men have been used in the studies due to the difficulty of urination for women under these conditions [66]. This might be due to the fact that it is significantly easier to perform bed rest studies, which can be a reason for these studies being preferred over dry immersion. It is also possible to have a larger test group at a lower cost as more space is needed for dry immersion and the energy to keep the water at the correct temperature is more substantial.

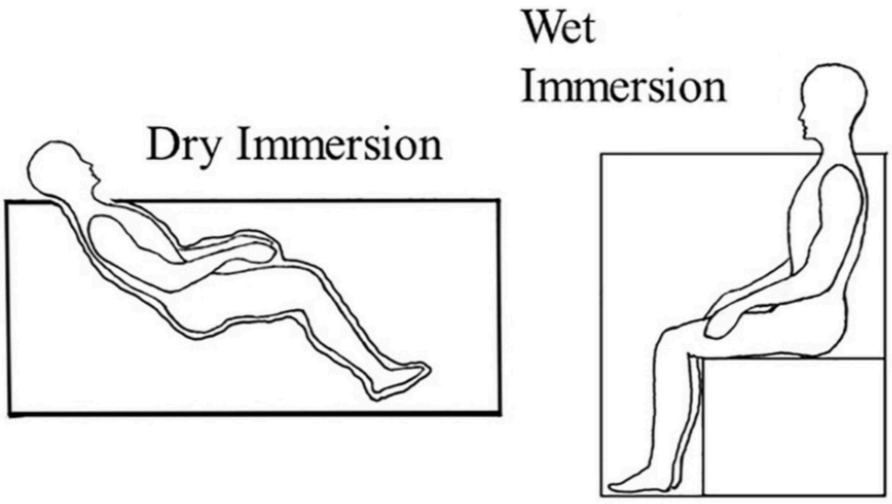

Figure 2.4: Depiction of wet and dry immersion [67].

2.2.3. Clinostat

The clinostat is a simple option to mimic microgravity on Earth: it does not eliminate nor alter gravity, but by constant rotation, the effects of gravity are thought to be neglectable for specific phenomena. However, the results depend on the orientation of the rotation in the three-dimensional space [70]. Clinostats support long-duration experiments on the ground and are generally used to study plants. Clinostats come with different rotational speeds and axes: classical slow-rotating ones have 1-2 revolutions per minute whereas the fast-rotating ones can reach 50-100 revolutions per minute, each with their own benefits. The samples are rotated either around one axis (1-D or 2-D clinostats) or two axes (3-D clinostat) [71]. The 3-D clinostats are similar to the RPMs as both are based on rotation around two axes, however, the rotational rates are different as the clinostat uses constant rotation rates whereas RPMs can vary in their rotation. The 1 and 2-D clinostat are shown in the following chapter in Figure 2.10. The 3-D clinostats will be covered more in the following section on the RPM.

The slow rotation allows to establish a region where centrifugal forces are below a certain threshold but the slow rotation might cause mechanostimuli in the biological samples, which plants can react to. In such cases, it can be better to increase the rotational rate. The fast-rotating clinostats can be used to look into sedimentation in a e.g. fluid or semisolid culture medium. During the fast rotation, the medium will achieve a stable state of rotation around the sample, where the sedimentation of the cell or plant sample becomes smaller than the movement of the medium. In this case, the medium stabilises around the rotating sample and will effectively eliminate gravity [72]. When rotating quickly, the system will no longer perceive the gravity vector and will not experience the same stresses that might affect the same biological sample in a slow-rotating clinostat.

Positioning the axis of rotation of a single-axis clinostat allows control of the experienced gravity and makes it possible to introduce hypogravity levels. The experienced gravity is equal to $g\,sin\,\alpha$, where α is the angle between the rotation axis and the horizontal and g is the gravitational acceleration. By tilting the axis $10°$, one achieves the gravity of the Moon, and with a bigger tilt one can achieve the gravity level at the surface of Mars. The single-axis clinostat has the advantage of being very simple and straightforward to use with its constant rotation while also minimising the expenses of setting up an experiment.

Despite the similarities generated in aspects of some biological samples grown on a clinostat, there are spotted great differences between biological samples on a clinostat and in true microgravity [36]. Hence the use of the clinostat is limited and it is very important to evaluate whether a system can and should be examined on the clinostat or if the system will show a different response compared to true microgravity.

Concerns about the rotation direction's effect on the test sample in a clinostat led to the development of the RPM, which is made exclusively to not impose any constant force in any certain direction [72].

2.2.4. Random Positioning Machine

The RPM is an advancement from the clinostat using the same principle of rotation as a multiple axes rotating clinostat. However, the goal of the RPM is to negate the effects of gravity over time by manipulating the gravity vector tip to point in all directions of the sample, so the resulting gravity level approaches microgravity. This is done using algorithms that change rotation rates or direction randomly to avoid the effects of always turning in the same direction [73]. The RPM are shown in several figures in later chapters but is a small machine with two individually rotating frames and a platform at the centre to support experiments.

The clinostat can rotate both too slowly and cause a dynamic stimulation in the plants, or too fast and cause unwanted effects due to the increased centrifugal force [74, and references herein]. In a comparison of the clinostat with the RPM and real spaceflight experiments, the plastid position in columella cells in *Arabidopsis* of the spaceflight flown specimens were more similar to the RPM experiment than the clinostat experiment [36]. Indicating that the RPM is better for studying gravitational effects in flowering plants compared to the clinostat.

The RPM also generally has the advantage that it can be used as a clinostat as well. In case rotation is only desired in one axis, the other one can simply remain static, in which case it will work as a clinostat. One of the most widely studied cell models for gravity sensing and growth in plants is the *Chara* rhizoid, which has been studied on sounding rockets, the space shuttle and on clinostats. In an effort to evaluate the simulated microgravity quality of the different operating modes of the RPM, the *Chara* rhizoid was placed at different operating modes of the RPM, which includes clinostatic operations as well as on the sounding rocket MAXUS. The experiment showed that fast rotation of the RPM was necessary in order to achieve results similar to those obtained in the sounding rockets. The rotation rates both in 2-D and 3-D mode should be around 60 rpm [75]. This study on Chara rhizoids indicates that the vibrations generated due to the rotation impacted the growth in the 3-D rotation and therefore the 2-D option would be better for simulating microgravity. From this, one needs to carefully evaluate the biological system before choosing a platform for simulating microgravity. There might be unwanted effects for specific biological systems during certain experimental configurations.

There have also been studies giving organism-specific recommendations to the use of ground-based platforms, which here is limited to consider clinostats, RPMs and magnetic levitation. It was shown that for several cell types, either a clinostat or RPM would be the preferred platform, whereas magnetic levitation only proved to be a better simulator of microgravity for Drosophila behaviour [76].

The gravity level of a run on the RPM is, depending on the settings, within the range of parabolic flights and sounding rockets at around $10^{-3}g$ but the RPM can be used for an extended time period. The longer the run on the RPM, the less prone the average g-level is to change due to variation of the rotation. One important thing to note is, however, that the biological response time to changes in the gravity vector should be longer than the rotation of the gravity vector. If this is not the case, then gravity will affect the sample and although it still reaches a mean gravity level close to zero over a long period of time, the effects of this simulation will be misleading as the biological system will react to the gravity vector before its direction is updated. This can for example be a combustion system. It would not make sense to put such an experiment on the RPM and expect it to simulate microgravity.

2.2.5. Rotating Wall Vessel

Rotating Wall Vessels (RWVs) also known as rotating bioreactors or rotating cell culture system was developed at NASA and designed for cell cultures or aquatic organisms [76]. Cells are kept in suspension in a medium in the RWV and through the rotation, they experience a constant free fall and thereby simulated microgravity while oxygen is delivered along an axial oxygenator [77], [78]. It utilises the same principles as a clinostat by rotating around one axis but the RWV creates a very low shear stress environment [79]. The RWV can be seen in Figure 2.5.

There are three fundamental aspects, that impact the use of the RWV and should be followed to optimise

its use. The first is to minimise the terminal velocity by selecting microcarrier beads and culture media that have almost the same density. Secondly, the rotation introduces both Coriolis and centrifugal forces that depend on the terminal velocity. These are minimised when the velocity is minimised. The last aspect is the mass transportation of nutrients to the cell in suspension [78]: if the RWV is rotated too slowly, the cell will be constantly at the bottom of the medium close to the wall, whereas a too fast rotation forces the cell to stay close to the outer wall due to the centrifugal force. These two situations set a physical limitation to the rotational rates, as the cell should not hit the wall.

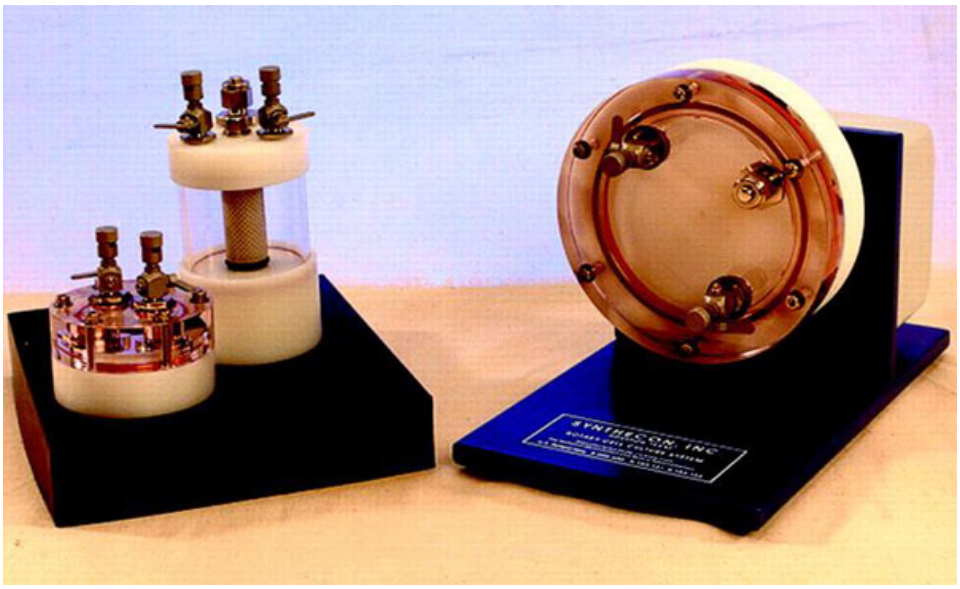

Figure 2.5: A Rotating Wall Vessel by NASA [80].

The use of RWVs covers a large variety of mainly cells and tissues [81] but also zebrafish [82]. They have been used for several decades in biological research and are readily available from Synthecon. Although the RWVs are similar to clinostats, they act as specialized clinostats based on the idea to ideally create a mixed fluid environment with low shear to suspend cell cultures or allow tissue growth [77].

2.2.6. Magnetic Levitation

Gravity can be compensated magnetically at the molecular scale by creating a magnetic force that counteracts it. This has some great advantages as it has unlimited experimentation time, it is ground-based and it is easy to adjust the gravity level [83]. However, there are fundamental constraints related to the use of magnetic fields. It is impossible to compensate for gravity at all points in space, even though the space is small, but it is possible to compensate for gravity at several points within that space. That could be a horizontal plane or a vertical line where gravity is perfectly balanced by the counteracting magnetic force.

To create the magnetic field for levitation, one would need a strong source such as the Bitter solenoid or a superconducting solenoid magnet. When it comes to levitating biological material, a vertical bore magnet is needed [76]: this is placed inside the solenoid, and where the bore passes through the solenoid centre, the magnetic field will be the strongest. At the top of the bore, the magnetic field will push the material away, which can result in simulated microgravity when the magnetic force matches the gravitational force. The magnetic force then decreases gradually while moving towards the bottom of the bore. At the bottom, it will pull the sample towards the surface of Earth and the experienced force will be $2g$ as seen in Figure 2.6. This figure is based only on one type of magnetic field, but in reality, there can be more than one point where near $0g$ is achieved. The interesting aspect of diamagnetic levitation is its ability to counteract gravity throughout the volume of a specimen, similar to how gravity is counteracted when orbiting Earth [76]. The gravitational-induced phenomena that occur inside the body are better replicated by the diamagnetic levitation and there are no stresses inside the test volume that are caused by gravity. Moving away from $0g$ point, the gravitational level typically increases by $0.01g$

per millimeter. An example of a drawback with levitation is when looking at *Arabidopsis* seedlings: although the plant levitates, the root is bent in the direction of gravity, unlike what is seen in spaceflight. This indicates that although biological samples are similar to those of water, there are processes that need a stronger magnetic field to study simulated microgravity. It is simply not enough to be able to levitate the biological sample.

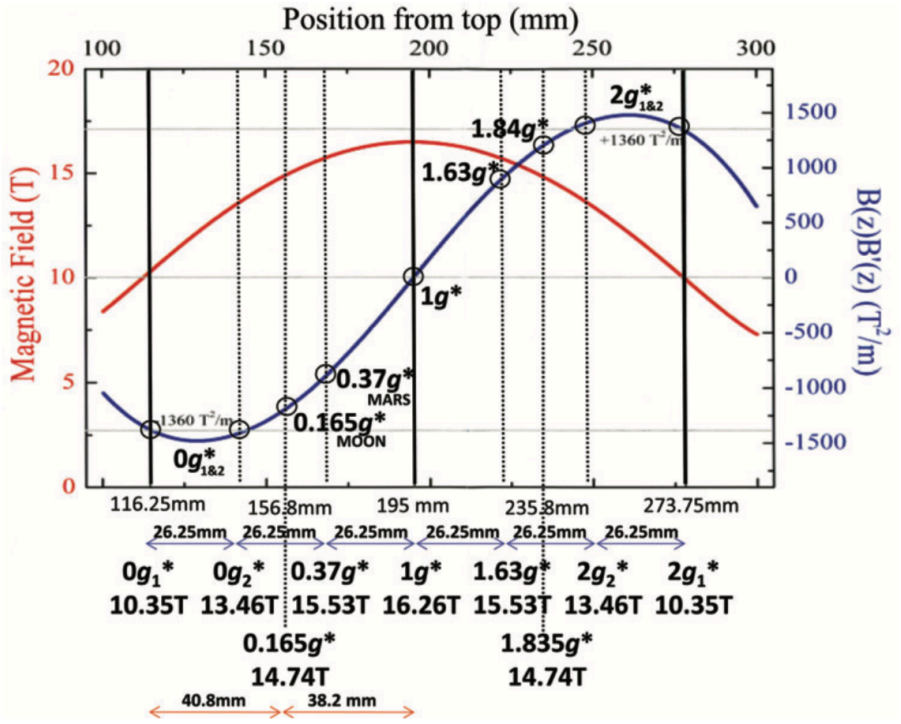

Figure 2.6: Gravitational level generated by magnetic levitation inside a magnetic bore on water [76].

An effort has been made to improve magnetic levitation by increasing the area where low g-level is achieved [84]. It proved possible to make a volume of $4004\,\mu L$ where the net force resulted in a gravity level less than 1% of Earth's. This can be achieved when superimposing a strong uniform magnetic field $\boldsymbol{B_0}$ with a weak field $\boldsymbol{B_1}$ that has an almost constant field-gradient $\boldsymbol{\Delta B_1}$. That way one achieves an approximately uniform field $\boldsymbol{B = B_0 + B_1 \approx B_0}$ with a fairly constant field-gradient $\boldsymbol{\Delta B \approx \Delta B_1}$. The strong uniform field can be generated in the traditional way with a superconducting solenoid magnet, whereas the improvement comes from combining this with a gradient-field Maxwell coil to produce the desired field properties. The volume, however, is still relatively small and limits the samples that can levitate at the centre of the coil. The achieved volume of low gravitational pull is furthermore more isotropic than using regular methods. When using this approach to create a Mars gravity level of $0.38g$, the volume increases to around $20\,000\,\mu L$. This indicates that once this technology matures and experiences further developments, the test area might increase, making it possible to study the long-term effects of simulated microgravity in larger test samples.

Although this method has been used previously to levitate a mouse, or at least partially levitate a mouse as seen in Figure 2.7 [85], the gradually changing levitating force will become a problem as the magnetic field needs to be strong enough to fully levitate a larger sample in the zero-g environment at the top of the bore. In Figure 2.6 shown earlier, it can be seen that the bore is only able to simulate microgravity for a small area around $2.6\,cm$ from the top. Moving away from this area results in an increase in g-level of $0.01g$ per millimetre and does not indicate a good use for larger samples. There are also other complexities related to the use of magnetic levitation including the requirement to cool magnets to keep the test area around room temperature, to provide light as well as the cost of operating these types of systems [86]. Combining this with the relatively large space it requires to set up this platform, this platform still needs some development to fully reach its potential.

This should also be seen in the light of the previously mentioned study, which showed that gravitational effects in the included cell types are better studied using clinostats and RPMs rather than a magnetic levitator. Another study also showed that magnetic fields cannot be used to mimic the effects of microgravity in gravitactic unicellular organisms due to the magnetic field itself [87]. Having very strong magnetic fields affects the biological sample and can invalidate the results, thus it can be problematic for a large range of systems to be studied on ground using this platform due to the strong effects the magnetic field introduces.

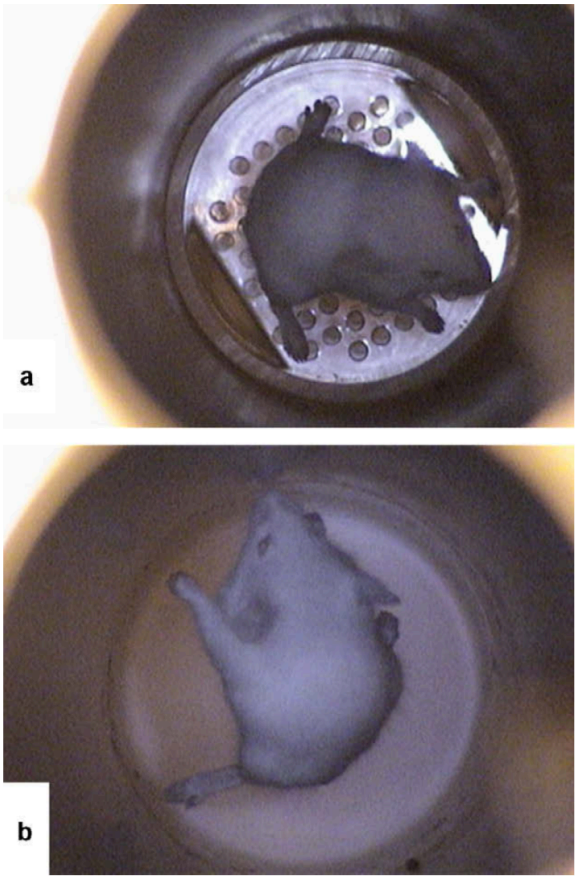

Figure 2.7: A mouse inside the cage of the magnet in **A** and the mouse levitated without the cage in **B** [85].

2.2.7. Hindlimb Unloading

Hindlimb Unloading (HU) has been around for a long time and relates to simulating microgravity in rodents, especially rats. The HU model is used for various purposes that originate from studying musculoskeletal responses to a simulated space environment but are now also used for other purposes, e.g. to study muscle atrophy [88] or the effects of cephalad fluid shifts on the rat's eyes [89], [90]. This model has proven to resemble the loss of muscles as seen in space, hence it seems like a good alternative to study the skeletal muscle system of rodents on Earth when experimentation in space is not available [91]. The principle of HU is to lift the rat mechanically by the rear parts, such that the experienced gravity is reduced compared to normal. A sketch of how the HU is done can be seen in Figure 2.8.

HU does not eliminate the presence of gravity and the inner organs still exert pressure on each other in HU unlike when in space, where the organs flow around freely. However, some of the important advantages are that experiments can be scheduled without considering certain crew schedules and modifications to the experiments can be done easily and with low cost. Furthermore, experiments can be repeated and extended on a routine basis, there exist no further safety aspects as there would be in space, and finally, the tissue can be taken from the anaesthetised animal at any time during the experiment [92]. These are some of the most important aspects of why ground-based analogues are

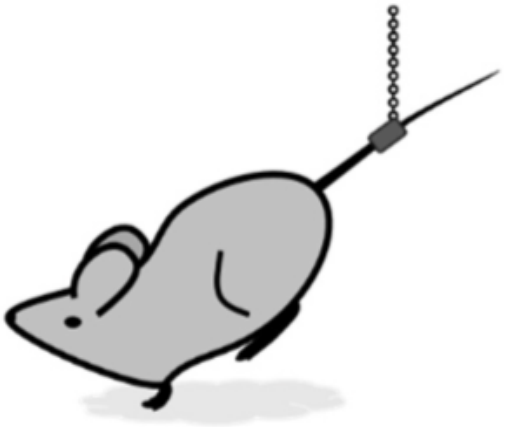

Figure 2.8: Hindlimb unloading of rats [13].

advantageous in relation to studying the effects of space and being able to precisely design experimentation in space. The development of the HU model considered various physiological responses including differential muscle atrophy, cephalad fluid shift, freedom to move, eat, and groom using the forelimbs, unloading the hindlimbs without paralysis to ensure recovery was possible, and the final aspect is a regular weight gain in growing rats or minimal weight loss in adults during the experiments [92]. It was found that unloading the hindlimbs of a rat leading to a head-down tilt of 30° proved to be a good model for spaceflight effects in rats. Even though it is a good model for certain aspects, the normal weight gain and reduced weight loss are not met by this model when using a harness to unload the rats, instead, it was sought to use traction tape for the tail, which proved to have an improved effect on the weight during a two-week experiment [93] and is the method that is widely used today.

2.3. Platform Overview

Looking across the variety of platforms, some clear limitations apply to the individual platforms. Both when it comes to sizing of experiments, duration or accessibility. Each platform can be used for certain studies and depending on the system, some platforms might be preferred over others either due to limited crew time on the ISS, cost or restrictions of the experiment. The free-fall environments are summarised in Table 2.3 and the ground-based platforms are summarised in Table 2.4.

Table 2.3: Summary of the free fall environments.

	UAV	**Drop Tower**	**Parabolic Flight**	**Sounding Rockets**	**Suborbital Flight**	**Orbital Flight**
Microgravity level [g]	10^{-2}	10^{-6}	10^{-2}	$\leq 10^{-4}$	$<10^{-5}$	10^{-6}
Duration	<12 s	<10 s	$20-30$ s	Up to 20 minutes	3 minutes	Days to months
Hypogravity potential	Yes	Yes	Yes	No	Yes	Yes
Hypergravity potential	No	No	Yes	No	No	Yes

Table 2.4: Summary of the ground-based microgravity platforms.

	HDT Bed Rest	**Wet and Dry Immersion**	**Clinostat**	**RPM**	**RWV**	**Magnetic Levitation**	**Hindlimb Unloading**
Simulated microgravity level	Analog	Analog	$<10^{-3}g$	$<10^{-3}g$	N/A	$<10^{-2}g$	Analog
Duration	Up to 1 year	<2 months	Unlimited	Unlimited	Unlimited	Unlimited	Months
Hypogravity potential	Yes	No	Yes	Yes	Yes	Yes	No
Hypergravity potential	No	No	Yes	Yes	No	Yes	No

Choosing the correct platform depends heavily on the situation. However, there is a large potential in utilising ground-based platforms, which exceeds just the benefit towards space applications. One such platform is the RPM, which very little is known about when it comes to its performance. This causes many people to use it suboptimally and can affect the outcome of studies and lead to misunderstandings of real processes happening in microgravity. It is furthermore one of the few platforms that can simulate both microgravity and hypogravity over a long duration and offers great opportunities if used correctly. Up until today no complete model of the RPM existed to help answer questions on how the RPM can be used in research. Typical questions would be how big a payload can be, how big the RPM can be built and at what rates a sample should be rotating. These are some of the questions that will be answered in this thesis, whereas the initial research questions for the thesis are listed at the end of the following section. The mathematical model developed is used to find the limitations of the RPM while also showing new possibilities that can enable studies in the gravity dose response of biological samples. This is highly relevant for future missions to the Moon and Mars but can also be directly beneficial to life on Earth through the accelerated ageing processes occurring in microgravity. In the following section, more information on the RPM will follow before the model is developed.

2.4. History of the Random Positioning Machine

Gravity has always been a constant factor throughout the development of life on Earth however, for a long time there has also been an interest in understanding its influence and how it affects life to change the effective gravity. Back in 1806, Thomas Andrew Knight [94] placed plant seeds on a water wheel to study the effects on the growth of the resulting gravity. He managed to show that the plants orient themselves in the direction of the resulting gravity, and not solely by Earth's gravity. His experiment can be seen in Figure 2.9.

Figure 2.9: The set-up of Thomas A. Knight's waterwheel experiment taken from Davy [95].

Since then a lot has happened, and with the space missions in the 1950s and '60s, new interest in studying the effects of gravity rose. In 1958 Muller [96] suggested that rotational devices should be used to study the effects of microgravity on humans. The interest in altering gravity kept increasing, and today there are several platforms to study the effects of altering gravity across the entire gravity spectrum e.g. centrifuges, drop towers and parabolic flights to name just a few.

After these early attempts to understand the effect of gravity, the clinostat was developed. It is a device that can rotate around one axis at a fixed rotational rate and simulate some specific effects of microgravity. There exist different types of clinostats as seen in Figure 2.10, and they can come at different rotational speeds ranging from 1-2 rotations per minute up to 50-100 rotations per minute [71]. These are generally referred to as the slow and fast rotating clinostats, each good for its own application. The slow rotation allows to establish a region where centrifugal forces are below a certain threshold but the slow rotation might cause mechanostimuli in the biological samples, which the plants can react to. In such cases, it can be better to increase the rotational rate. The fast-rotating clinostats can be used to look into sedimentation in an e.g. fluid or semisolid culture medium. During the fast rotation, the medium will achieve a stable state of rotation around the sample, where the sedimentation of the cell or plant sample becomes smaller than the movement of the medium. In this case, the medium stabilises around the rotating sample and will effectively eliminate gravity [72]. When rotating quickly the system will no longer perceive the gravity vector, and will not experience the same stresses that might affect the same biological sample in a slow rotating clinostat. However, there can also exist 3-D clinostats, that rotate around two axes. Generally, clinostats have been used to study plant gravitropism and what effect simulated microgravity has on plants. Despite the similarities generated in aspects of some biological samples grown on a clinostat, there are spotted great differences between biological samples on a clinostat and in true microgravity [36].

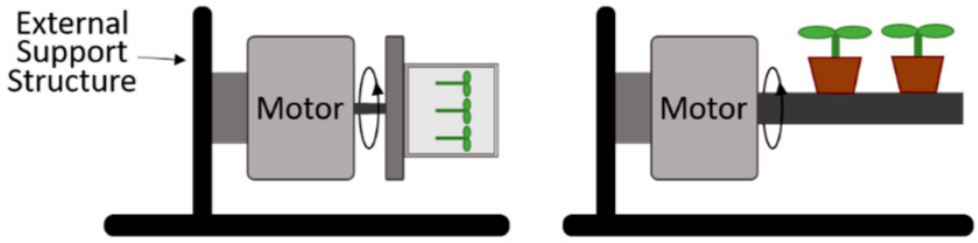

Figure 2.10: Examples of 1-D clinostat to the left and 2-D clinostat to the right [13].

In the 1990's however, some more advanced controls of the 3-D clinostats were introduced in Japan. Here Hoson and colleagues proposed to randomly change the rotational direction ranging from 2 to -2 revolutions per minute with a change in rotation rate every 30-60 s [74], [97]. This was the first time, the random aspect was introduced into the clinostat. This improved the trajectory of the gravity vector, forcing it to point in more directions as seen in Figure 2.11. One problem encountered here was the large acceleration leading to damaging torques on the O-rings. As Hoson et al. proposed, this could be solved by gradually changing the rotational rates.

At Fokker Space in the Netherlands a few years later, another type of RPM was built, based on a purely random algorithm. The movement would change at random time steps to random rotational rates in order to generate simulated microgravity. This RPM was converted into a desktop-sized version to allow it to be used in an incubator, where the environment can be carefully controlled [98]. The environment has a significant impact on the cells that would be the payload of the RPM, which is why there was a need to control variables such as temperature and humidity for studies on cells. Currently, it is the only one still commercially available, however now it is available through Yuri gmbh, which acquired it from Airbus Defence and Space Netherlands B.V. This RPM has been widely used in gravity-related research and has been validated through several studies comparing simulated microgravity with true microgravity. Not only have the RPM proven useful for space-related research, but other fields have also used the RPM as a versatile tool. This includes studies on cancer research and tissue engineering [10], [81], [99].

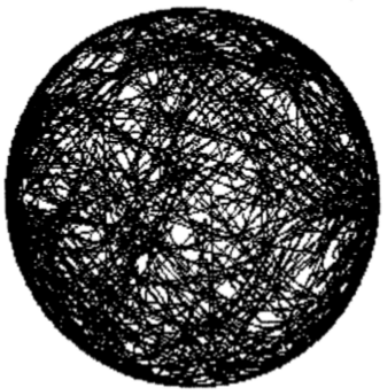

Figure 2.11: Motion of a sample on the 3-D clinostat during 3 hours [74].

In more recent years, a new approach was developed by Wuest et al. [100], [101]. Here they used a constant rotational rate with the direction being inverted at random time steps. This was shown as a new way to control the RPM, and this could be used to simulate microgravity effects in some systems. As will be shown later, it is very important to be careful when selecting the rotational speed, especially in this case as the resulting gravity level varies significantly between different rates.

Yet another control algorithm was developed by Wubshet et al. [102]: this is based on a surjective map comprised of the two angles that describe the orientation of the gravity vector based on the rotating frames. The orientation of the gravity vector will cover a sphere, and in order to have a uniformly distributed orientation, a non-uniform distribution of angles is needed. This can be achieved by the use of Archimedes' theory [103]. Rather Wubshet et al. create a reference trajectory of all points in the sphere that have an equal likelihood of being visited. Then it follows that random points are taken and projected onto the surface of the unit sphere. Here neighbouring points are being merged to form a trajectory. The geodesic curvature and distance between points on this trajectory determine the angular velocity and acceleration that the RPM is following. To limit the angular acceleration only points close to the current point of the trajectory are included as possibilities for the next point. An example of a trajectory created by the algorithm is shown below in Figure 2.12.

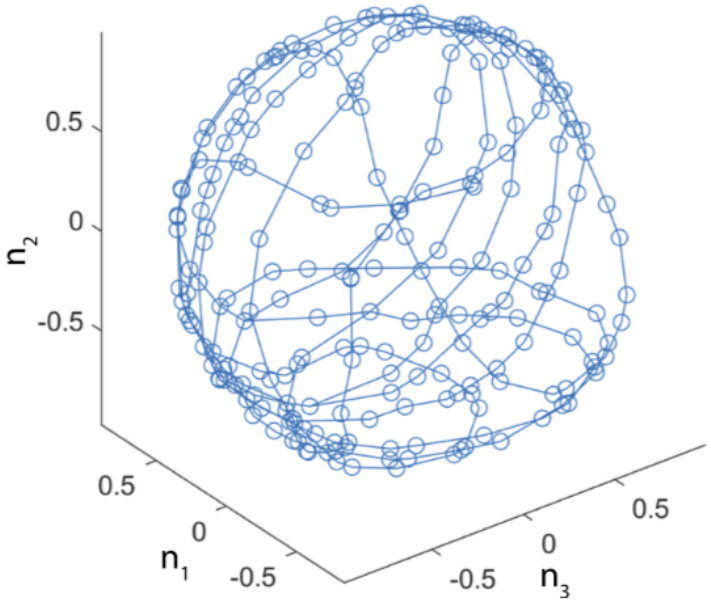

Figure 2.12: RPM trajectory design presented by Wubshet et al. Wubshet, Arreguin-Martinez, Nail, *et al.* [102].

These various methods show that there exists not just one algorithm to control the movement of the frames and manipulate the gravity vector to eliminate the effects of microgravity but several different approaches have already been demonstrated. The best approach to take is difficult to determine, and there exist many other unexplored approaches that might improve the experiments. The various algorithms may have their own strengths and weaknesses and might only work for certain systems, so the correct controls depend heavily on the payload. Depending on the size, for example, additional accelerations may be introduced further from the centre of rotation, resulting in a suboptimal simulated microgravity environment. When developing a control algorithm, these aspects must be considered to achieve a good environment on the RPM. With future missions to Mars and the Moon, where the gravity level is different and not easily accessible, it can prove useful to use RPMs to simulate these hypogravity levels for research purposes. Developing a customized RPM in-house can offer much greater control of the movement of the RPM and can be (re)-designed for multiple systems. Scientists can benefit from understanding the limitations of the RPM, which can be used to better design research on the RPM.

This chapter gives only a brief overview of the RPM, many studies have been done using the RPM and there also exist some, which look into more technical aspects of the RPM. However, understanding where the RPM comes from, and how it was developed can help in the following chapter, which covers more technical aspects of the RPM. The following research questions were established to guide the work and further expand our knowledge of how the RPM can be used.

- How can the rotational rates for predicting the resulting g-level be modelled?
  - What are the best combinations of rotational rates for an RPM to simulate microgravity using constant velocities?
    - How do the combinations of rotational rates relate to g-level?
    - To what extent can the g-level be improved using alternative control algorithms?
  - How would the model change when considering Moon and Mars gravity levels?
  - To what extent are the optimal combinations useful in a real experiment on the RPM?
- What effect does moving away from the centre of rotation have on the residual g-level?
  - At what point will the residual forces be so significant that microgravity is no longer achieved?
  - How would the RPM be scaled if multiple g-levels should be simulated during the same?
- To what extent does the experimental data match the theoretical model?

3

Materials and Methods

This chapter aims to outline the governing equations for modelling the motion of the RPM. This includes the kinematics of the two individual rotating frames in Section 3.1 where velocities and accelerations are included. Section 3.2 covers miscellaneous aspects of the model and an explanation of how to track the gravity vector tip. Changing the position of the sample on the RPM is briefly considered in Section 3.3. To validate the model, a motion capture system and two Inertial Measurement Units (IMUs) are used on the RPM. The experimental setup concludes this chapter in Section 3.4.

3.1. Kinematics of the RPM

The RPM is built by having two individually rotating frames connected to a platform, that can support experiments. An example of a typical RPM is the only commercially available RPM from Yuri gmbh, this can be seen in Figure 3.1. The frames are controlled by an algorithm that, by rotation, allows the distribution of the gravity vector in all directions. Doing this over time can make the sample on the experimental platform experience a state of simulated microgravity, as long as the rotation is faster than the sample's response time to gravity [104]. With careful control, it is also possible to simulate hypogravity levels, such as the Moon's or Mars' gravity. This is particularly useful for studies related to future human space missions, as these include sending humans to the surface of the Moon and Mars. This section covers the kinematics of the RPM and results in a mathematical expression for its performance.

3.1.1. Initial Considerations

Considering the two axes freely rotate as shown in Figure 3.2, it is clear, that the outer frame rotates with ω_O around the local x_O - axis, which is coincident with the static global x_G -axis. The inner frame rotates with ω_I around the local y_I -axis that is the same as the y_O -axis (not y_G -axis). The origins of all reference frames are in the centre of rotation but are drawn at a distance for clarity. With the reference frames defined, it is possible to look at the kinematics of the two frames and relate this to the rotation. This will yield some governing equations for the movement, that can be used to generate a model of the RPM that can predict the performance of RPMs. This will prove to be a valuable tool in outlining the limitations for ground-based studies using RPMs. As there will be rotating axes, the first step is to show the rotational matrices relevant to the model. Throughout, subscript *O* is used for the outer frame's reference frame, *G* indicates the global, stationary reference frame and finally, *I* marks the reference frame of the inner frame. Subscript *P* emphasises the point P in the inner frame. As seen in Equation 3.1 and 3.2, the rotation is dependent on the angle, the sample makes with the global reference frame. Below, σ indicates the angle of rotation of the outer frame about x_O and θ indicates the angle of the inner frame in relation to the outer frame. These two equations are valid when performing a positive (counterclockwise) rotation around the respective axis. This can be visualised by taking the right hand and holding the thumb in the positive direction of the axis of rotation, then curling the other fingers towards the palm will reveal the positive rotational direction. That means, for the x-axis, that one would curl the fingers from the z towards the y-axis, showing the positive rotation. However, when

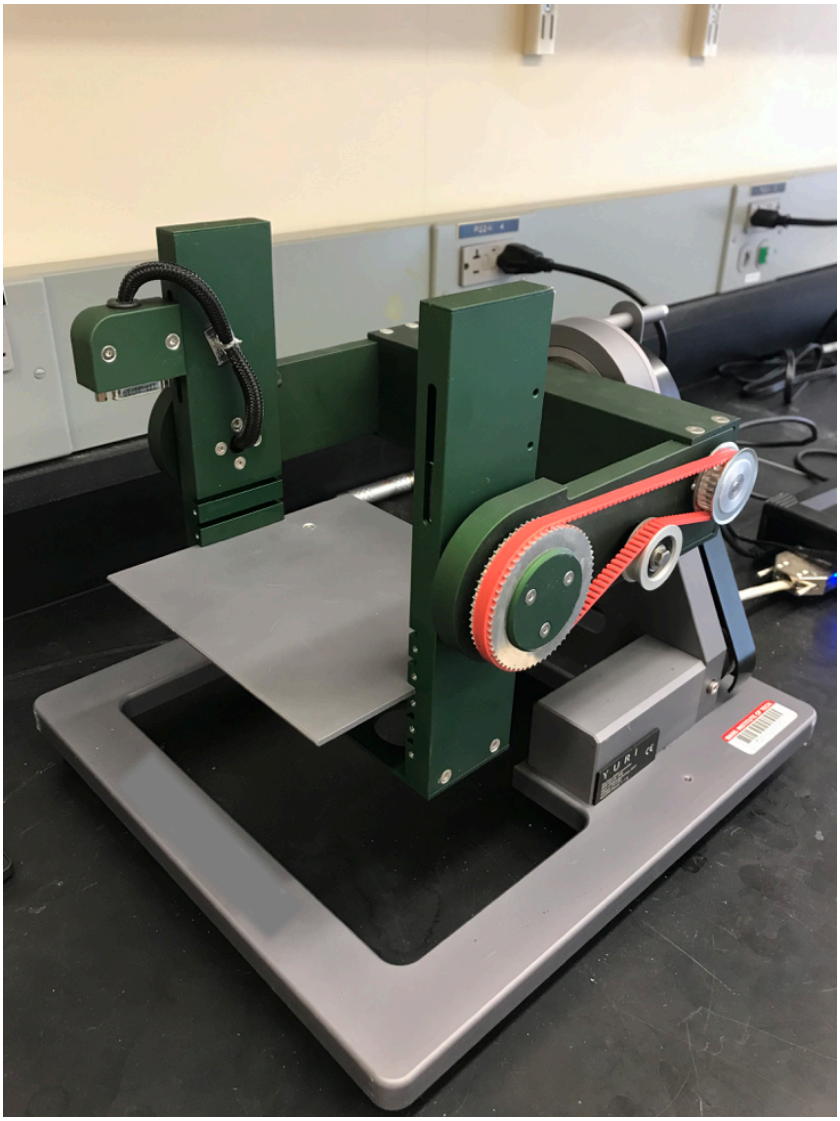

Figure 3.1: RPM from Yuri.

it is necessary to rotate the opposite way, the sign of the angles can be switched, allowing rotation from the inner frame to the global reference frame. These equations are shown in Equation 3.3 and Equation 3.4. This is equivalent to switching the signs of the sines.

$$R_x = \begin{bmatrix} 1 & 0 & 0 \\ 0 & cos\,\sigma & -sin\,\sigma \\ 0 & sin\,\sigma & cos\,\sigma \end{bmatrix} \tag{3.1}$$

$$R_y = \begin{bmatrix} cos\,\theta & 0 & sin\,\theta \\ 0 & 1 & 0 \\ -sin\,\theta & 0 & cos\,\theta \end{bmatrix} \tag{3.2}$$

$$R_{x_{opp}} = \begin{bmatrix} 1 & 0 & 0 \\ 0 & cos\ (-\sigma) & -sin\ (-\sigma) \\ 0 & sin\ (-\sigma) & cos\ (-\sigma) \end{bmatrix} = \begin{bmatrix} 1 & 0 & 0 \\ 0 & cos\,\sigma & sin\,\sigma \\ 0 & -sin\,\sigma & cos\,\sigma \end{bmatrix} \tag{3.3}$$

$$R_{y_{opp}} = \begin{bmatrix} cos\ (-\theta) & 0 & sin\ (-\theta) \\ 0 & 1 & 0 \\ -sin\ (-\theta) & 0 & cos\ (-\theta) \end{bmatrix} = \begin{bmatrix} cos\,\theta & 0 & -sin\,\theta \\ 0 & 1 & 0 \\ sin\,\theta & 0 & cos\,\theta \end{bmatrix} \tag{3.4}$$

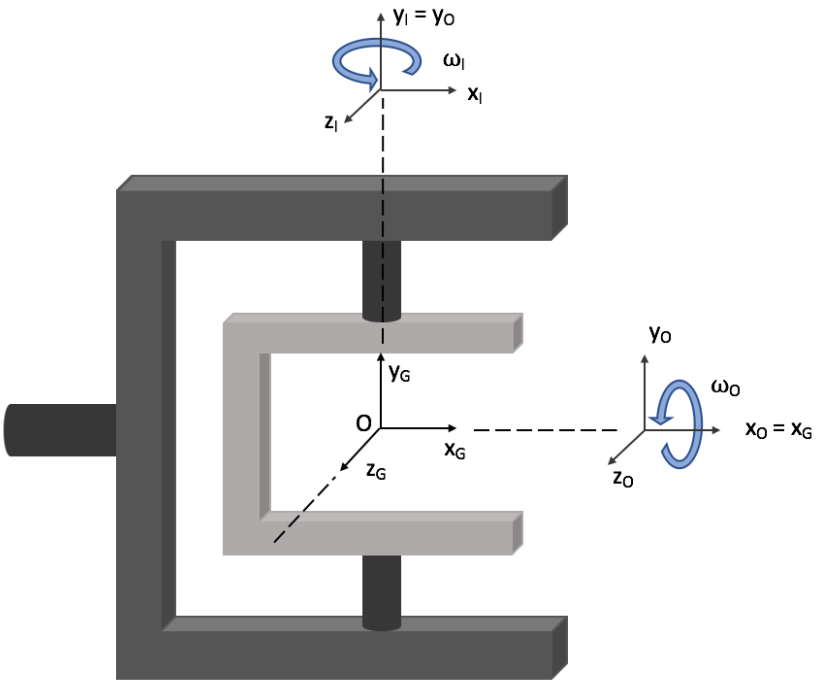

Figure 3.2: Reference frame for the RPM.

3.1.2. Angular Velocity

With the coordinate system defined, the next step is to define the motion of the frames. The angular velocity can be written as shown in Equation 3.5 to 3.7. There will be a contribution from both frames and as the model should support non-constant rotational rates, the rotation matrix is needed to ensure the correct contribution of the rotation of both frames at any instant. This means that the angles σ and θ are modelled as functions of time, to be used in the model.

$$\boldsymbol{\omega}_G = \boldsymbol{\omega}_O + \boldsymbol{R}_{x_{opp}} \cdot \boldsymbol{\omega}_I \tag{3.5}$$

$$\boldsymbol{\omega}_G = \begin{bmatrix} \omega_O \\ 0 \\ 0 \end{bmatrix} + \begin{bmatrix} 1 & 0 & 0 \\ 0 & cos\,\sigma & sin\,\sigma \\ 0 & -sin\,\sigma & cos\,\sigma \end{bmatrix} \begin{bmatrix} 0 \\ \omega_I \\ 0 \end{bmatrix} \tag{3.6}$$

$$\boldsymbol{\omega}_G = \begin{bmatrix} \omega_O \\ 0 \\ 0 \end{bmatrix} + \begin{bmatrix} 0 \\ \omega_I\,cos\,\sigma \\ -\omega_I\,sin\,\sigma \end{bmatrix} = \begin{bmatrix} \omega_O \\ \omega_I\,cos\,\sigma \\ -\omega_I\,sin\,\sigma \end{bmatrix} \tag{3.7}$$

The frames will rotate at a constant rate during the validation process due to the control limitations of the current RPM, however, this is not always the case when using a different algorithm. Therefore, the rate of change of the angular velocity is defined as the difference between two subsequent angular velocities divided by the time step as defined in Equation 3.8. This equation holds for both the inner and outer frame. In the model, the last element of the array is noted as zero, thereby assuming no change in velocity between the second to last and last element. This will have no consequence for the results of the model, which has several thousands of elements.

$$\dot{\boldsymbol{\omega}}\,(i) = \frac{\boldsymbol{\omega}\,(i) - \boldsymbol{\omega}\,(i-1)}{dt} \tag{3.8}$$

3.1.3. Angular Acceleration

The next step is to define the angular accelerations during rotation. To determine these, the angular velocities and rate of change of the angular velocities are important aspects. From the perspective of a static x_G, y_G, z_G reference frame, any time derivative of vector $\boldsymbol{A}$ can be described by the rate of

change of $\boldsymbol{A}$ observed in the rotating x_O, y_O, z_O frame plus the contribution caused by the rotating frame itself. $\boldsymbol{A}$ can be defined in the three axes as shown below in Equation 3.9, where $\boldsymbol{i}$, $\boldsymbol{j}$ and $\boldsymbol{k}$ are the unit vectors.

$$\boldsymbol{A} = A_x\boldsymbol{i} + A_y\boldsymbol{j} + A_z\boldsymbol{k} \tag{3.9}$$

The time derivative of $\boldsymbol{A}$ needs to account for both the change in magnitude but also the change in direction. Taken from the static frame, the direction of the vector only changes due to the rotation $\boldsymbol{\Omega}$, which leads to the following expression for the derivative of $\boldsymbol{A}$ in Equation 3.10.

$$\dot{\boldsymbol{A}} = \dot{A}_x\boldsymbol{i} + \dot{A}_y\boldsymbol{j} + \dot{A}_z\boldsymbol{k} + A_x\dot{\boldsymbol{i}} + A_y\dot{\boldsymbol{j}} + A_z\dot{\boldsymbol{k}} \tag{3.10}$$

The time derivative of the unit vector only displays a change in direction due to $\boldsymbol{\Omega}$ and not in its magnitude, hence $\dot{\boldsymbol{i}} = \frac{d\boldsymbol{i}}{dt}$ becomes an indication of the change in direction. Rotating the axis by $\boldsymbol{\Omega}\ dt$ yields a change in direction $d\boldsymbol{i}$ perpendicular to the initial direction as shown in Figure 3.3.

The directional change can then be described by the three expressions shown in Equation 3.11.

$$\dot{\boldsymbol{i}} = \boldsymbol{\Omega} \times \boldsymbol{i} \qquad \dot{\boldsymbol{j}} = \boldsymbol{\Omega} \times \boldsymbol{j} \qquad \dot{\boldsymbol{k}} = \boldsymbol{\Omega} \times \boldsymbol{k} \tag{3.11}$$

Completing the derivative considering both the magnitude and direction of the vector leads to the expression shown in Equation 3.12. The derivative is the sum of the derivatives observed from the rotating x_O, y_O, z_O frame and the cross product of $\boldsymbol{\Omega}$ and the vector $\boldsymbol{A}$.

$$\dot{\boldsymbol{A}} = \left(\dot{\boldsymbol{A}}\right)_{x_O y_O z_O} + \boldsymbol{\Omega} \times \boldsymbol{A} \tag{3.12}$$

This equation states that the derivative of a vector $\boldsymbol{A}$ observed from the static x_G, y_G, z_G reference frame can be described by the derivative of the same vector in the x_O, y_O, z_O frame plus the contribution caused by changing the direction. When there is no rotation present, the equation simply boils down to the time derivative of the vector in the given frame.

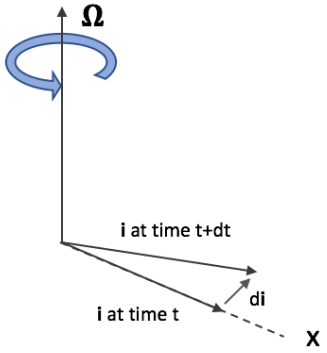

Figure 3.3: Change in direction of unit vector $\boldsymbol{i}$ due to rotation $\boldsymbol{\Omega}$.

This result can be used to evaluate the angular acceleration of the frames. The angular acceleration of the outer frame is shown in Equation 3.13, and the inner frame is shown in Equation 3.14. For the outer frame, the change of direction of $\dot{\boldsymbol{\omega}}_O$ always occurs in the same direction about the global x_G -axis, which means that $\boldsymbol{\Omega} = \boldsymbol{0}$ as the second term in Equation 3.12 yields $\boldsymbol{\omega}_O \times \boldsymbol{\omega}_O = \boldsymbol{0}$. For the inner frame, the rotation will be equal to the outer frame's rotation, i.e. $\boldsymbol{\Omega} = \boldsymbol{\omega}_O$.

$$\begin{aligned}(\dot{\boldsymbol{\omega}}_O)_{x_G,y_G,z_G} &= (\dot{\boldsymbol{\omega}}_O)_{x_O,y_O,z_O} + \boldsymbol{\omega}_O \times \boldsymbol{\omega}_O = (\dot{\boldsymbol{\omega}}_O)_{x_O,y_O,z_O} \\ &= \begin{bmatrix} \dot{\omega}_O \\ 0 \\ 0 \end{bmatrix}\end{aligned} \tag{3.13}$$

$$\begin{aligned}(\dot{\boldsymbol{\omega}}_I)_{x_G,y_G,z_G} &= \boldsymbol{R}_{x_{opp}} \cdot (\dot{\boldsymbol{\omega}}_I)_{x_O,y_O,z_O} + \boldsymbol{\omega}_O \times \left(\boldsymbol{R}_{x_{opp}} \cdot \boldsymbol{\omega}_I\right) \\ &= \begin{bmatrix} 0 \\ \dot{\omega}_I \cos\sigma \\ -\dot{\omega}_I \sin\sigma \end{bmatrix} + \begin{bmatrix} \omega_O \\ 0 \\ 0 \end{bmatrix} \times \begin{bmatrix} 0 \\ \omega_I \cos\sigma \\ -\omega_I \sin\sigma \end{bmatrix} \\ &= \begin{bmatrix} 0 \\ \omega_O\,\omega_I \sin\sigma + \dot{\omega}_I \cos\sigma \\ \omega_O\,\omega_I \cos\sigma - \dot{\omega}_I \sin\sigma \end{bmatrix}\end{aligned} \tag{3.14}$$

The angular acceleration α for the sample connected to the inner frame is defined in Equation 3.15.

$$\boldsymbol{\alpha}_G = \dot{\boldsymbol{\omega}}_G = (\dot{\boldsymbol{\omega}}_O)_{x_G,y_G,z_G} + (\dot{\boldsymbol{\omega}}_I)_{x_G,y_G,z_G} \tag{3.15}$$

3.1.4. Definition of a Point P

As the intention is to include a point P, that lies at a certain distance away from the centre of rotation, at which a sample can be placed, this point needs to be defined and supported by the model. The vector $\boldsymbol{P}$ is given in terms of the x_I,y_I,z_I frame, and needs to be converted to the global frame as shown in Equation 3.16 before moving to the following steps. This is done by using the rotational matrices previously shown, to allow for constant determination of the vector $\boldsymbol{P}$ at any instant.

$$\boldsymbol{P}_G = \begin{bmatrix} x_P \\ y_P \\ z_P \end{bmatrix}_G = \boldsymbol{R}_x \cdot \boldsymbol{R}_y \cdot \begin{bmatrix} x_P \\ y_P \\ z_P \end{bmatrix}_I \tag{3.16}$$

3.1.5. Velocity at Point P

With the point P established, it is now possible to look at the velocities and accelerations of this point during the operation of the RPM. This is done by setting up all the components related to the velocity and acceleration expressed in terms of the global frame. In any given dynamical system the velocity can be defined as shown in Equation 3.17. In order not to mix the general expression up with the specific notation of the RPM, A and B will be used as two points in C, the original coordinate system. A small sketch is shown in Figure 3.4. A rod connecting the origin and point A rotates with angular velocity ω_A and the same goes for a rod from point A to B, that independently rotates by ω_B. In the equation, the component for the translational velocity of the reference frame ${}_C\boldsymbol{V}_A$ will be found, as well as the relative velocity of point B with respect to A observed from the rotating frame i.e. like there was no rotation. This is explicitly stressed out in the equation. The final contribution comes from the cross-product of the angular velocity and the vector P describing point B from the origin.

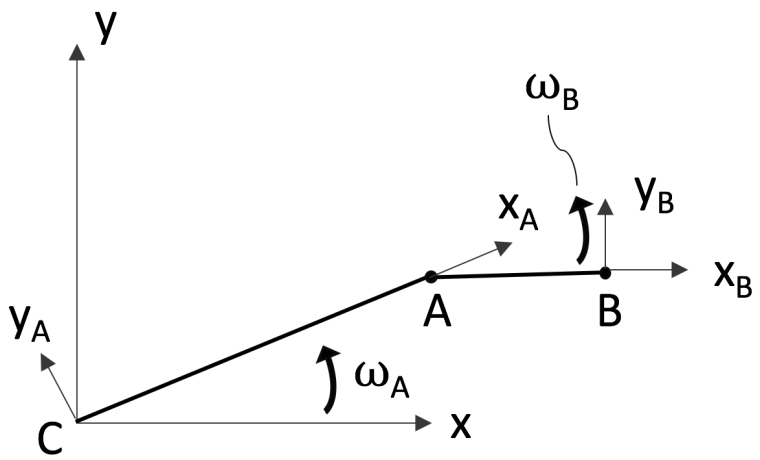

Figure 3.4: Sketch of a general system with two rotating frames.

The first term in the equation reads “velocity of B in C”, and this notation is used throughout. Setting up the equations shows that the velocity ${}_C\boldsymbol{V}_A$ has to be determined by applying the same equation again at point A. Hence, Equation 3.18 show the equation for the relative velocity of ${}_O\boldsymbol{V}_A$. In this equation, lowercase c describes the rotating frame of x_A and y_A, which rotates together with the rod going from the origin to point A. If one had more rotating systems at the end of B, the same equations should be applied again to find the correct velocity.

$${}_C\boldsymbol{V}_B = {}_C\,\boldsymbol{V}_A + {}_A\,\boldsymbol{V}_B|_{\omega_B=0} + {}_C\,\boldsymbol{\omega}_B \times_A \boldsymbol{P}_B \tag{3.17}$$

$${}_C\boldsymbol{V}_A = {}_C\,\boldsymbol{V}_c + {}_c\,\boldsymbol{V}_A|_{\omega=0} + {}_C\,\boldsymbol{\omega}_A \times_c \boldsymbol{P}_A \tag{3.18}$$

Combining these two equations yields the final result for the system. In this case ${}_C\boldsymbol{V}_c = 0$, ${}_c\boldsymbol{V}_A|_{\omega=0} = 0$, ${}_A\boldsymbol{V}_B|_{\omega_B=0} = 0$, hence the equation can be simplified to Equation 3.19.

$${}_C\boldsymbol{V}_B = {}_C\,\boldsymbol{\omega}_B \times_A \boldsymbol{P}_B + {}_C\,\boldsymbol{\omega}_A \times_c \boldsymbol{P}_A \tag{3.19}$$

The same approach can be used when looking at the RPM. The velocity of point P in the global reference frame and all its components can be seen in Equation 3.20. This includes the translational velocity of the global frame (which is ${}_G\boldsymbol{V}_O = \boldsymbol{0}$), as well as contributions from the two rotating frames following the steps shown in the above equations.

$$ {}_G\boldsymbol{V}_P = {}_G\boldsymbol{V}_O + {}_O\boldsymbol{V}_P + {}_G\boldsymbol{\omega}_O \times_G \boldsymbol{P}_P \tag{3.20} $$

Here the relative velocity ${}_O\boldsymbol{V}_P$ can be determined by applying the same equation again at this new point. This leads to the following equations in Equation 3.21. There is no translational velocity of the inner frame, or of point P with respect to the rotating inner frame, hence the equation can be simplified to a cross-product. This is implemented to Equation 3.20 which leads to the final expression shown in Equation 3.22.

$$ {}_O\boldsymbol{V}_P = {}_O\boldsymbol{V}_I + {}_I\boldsymbol{V}_P + {}_O\boldsymbol{\omega}_P \times_O \boldsymbol{P}_P \tag{3.21} $$

$$ {}_G\boldsymbol{V}_P = {}_G\boldsymbol{V}_O + {}_O\boldsymbol{V}_I + {}_I\boldsymbol{V}_P + {}_O\boldsymbol{\omega}_P \times_O \boldsymbol{P}_P + {}_G\boldsymbol{\omega}_P \times_G \boldsymbol{P}_P $$

$$ {}_G\boldsymbol{V}_P = 0 + 0 + 0 + {}_O\boldsymbol{\omega}_P \times_O \boldsymbol{P}_P + {}_G\boldsymbol{\omega}_P \times_G \boldsymbol{P}_P = {}_O\boldsymbol{\omega}_P \times_O \boldsymbol{P}_P + {}_G\boldsymbol{\omega}_P \times_G \boldsymbol{P}_P \tag{3.22} $$

To use these equations in the model, the individual components are transformed using the rotation matrices, so they are all expressed in terms of the x_G, y_G, z_G frame. The velocity of the moving frame used to find the Coriolis acceleration is Equation 3.21, which is reduced to Equation 3.23 where ${}_O\omega_P = {}_O\omega_I$ as every point on the experimental platform rotate with the same angular velocity.

$$ \boldsymbol{V}|_{moving\,frame} = {}_O\boldsymbol{V}_P = {}_O\boldsymbol{V}_I + {}_I\boldsymbol{V}_P + {}_O\boldsymbol{\omega}_P \times_O \boldsymbol{P}_P = 0 + 0 + {}_O\boldsymbol{\omega}_P \times_O \boldsymbol{P}_P \tag{3.23} $$

$$ \boldsymbol{V}|_{moving\,frame} = {}_O\boldsymbol{\omega}_P \times_O \boldsymbol{P}_P $$

3.1.6. Acceleration at Point P

When it comes to acceleration, there are several factors contributing to the overall acceleration of point P. These include the centripetal acceleration, Coriolis acceleration, the Euler acceleration, the relative acceleration due to the rotation of the frames, and finally, the acceleration of the global reference frame as outlined in Equation 3.24. The general definition of the centripetal, Coriolis and Euler accelerations are shown below. As the RPM is placed on the surface of Earth, the acceleration of the *G*-frame $\boldsymbol{a}_G$ is constant and also shown below.

$$ {}_G\boldsymbol{a}_P = \boldsymbol{a}_G + {}_O\boldsymbol{a}_P + ({}_G\boldsymbol{a}_P)_{centripetal} + ({}_G\boldsymbol{a}_P)_{Coriolis} + ({}_G\boldsymbol{a}_P)_{Euler} \tag{3.24} $$

$$ \boldsymbol{a}_G = \begin{bmatrix} 0 \\ 0 \\ -g \end{bmatrix} \qquad \boldsymbol{a}_{Coriolis} = 2\,\boldsymbol{\omega} \times \boldsymbol{V}|_{moving\,frame} $$

$$ \boldsymbol{a}_{centripetal} = \boldsymbol{\omega} \times (\boldsymbol{\omega} \times \boldsymbol{P}) \qquad \boldsymbol{a}_{Euler} = \dot{\boldsymbol{\omega}} \times \boldsymbol{P} $$

The relative acceleration is, like the velocity, noted as ${}_O\boldsymbol{a}_P$ and is again taken with respect to an observer in the moving frame. This relative acceleration consists of the same five elements for the next frame and is shown in Equation 3.25.

$$ {}_O\boldsymbol{a}_P = \boldsymbol{a}_I + {}_I\boldsymbol{a}_P + ({}_O\boldsymbol{a}_P)_{centripetal} + ({}_O\boldsymbol{a}_P)_{Coriolis} + ({}_O\boldsymbol{a}_P)_{Euler} \tag{3.25} $$

$$ {}_O\boldsymbol{a}_P = \boldsymbol{a}_I + {}_I\boldsymbol{a}_P + \boldsymbol{\omega} \times (\boldsymbol{\omega} \times \boldsymbol{P}) + 2\,\boldsymbol{\omega} \times \boldsymbol{V}|_{moving\,frame} + \dot{\boldsymbol{\omega}} \times \boldsymbol{P} $$

The translational acceleration of the inner frame is $\boldsymbol{a}_I = \boldsymbol{0}$, the relative velocity $\boldsymbol{V}|_{moving\,frame}$ is zero, making the Coriolis contribution zero, finally the relative acceleration ${}_I\boldsymbol{a}_P$ is also zero. This makes it possible to simplify the expression to just two terms comprising the Euler term and the centripetal acceleration contribution as seen in Equation 3.26.

$$ {}_O\boldsymbol{a}_P = {}_O\boldsymbol{\omega}_I \times ({}_O\boldsymbol{\omega}_I \times_O \boldsymbol{P}_P) + {}_O\dot{\boldsymbol{\omega}}_I \times_O \boldsymbol{P}_P \tag{3.26} $$

Now it is possible to set up the equation for the resulting acceleration at point P in the inner frame. To find the relative velocity for the Coriolis contribution, the correct velocity was defined in Equation 3.21, with only the term ${}_O\boldsymbol{\omega}_P \times_I \boldsymbol{P}_P$ contributing. The complete expression for the acceleration can be seen in Equation 3.28. The subscripts outside of the parentheses indicate that the entire term is calculated in one frame and rotated, such that all components are expressed in terms of the x_G, y_G, z_G frame.

$$ {}_G\boldsymbol{a}_P = \boldsymbol{a}_G +_O \boldsymbol{a}_P + \boldsymbol{\omega} \times (\boldsymbol{\omega} \times \boldsymbol{P}) + 2\,\boldsymbol{\omega} \times_O \boldsymbol{V}_P + \dot{\boldsymbol{\omega}} \times \boldsymbol{P} \tag{3.27} $$

$$ \begin{aligned} {}_G\boldsymbol{a}_P = \boldsymbol{a}_G &+_G [{}_O\boldsymbol{\omega}_I \times ({}_O\boldsymbol{\omega}_I \times_O \boldsymbol{P}_P)]_O +_G [{}_O\dot{\boldsymbol{\omega}}_I \times_O \boldsymbol{P}_P]_O \\ &+_G \boldsymbol{\omega}_O \times ({}_G\boldsymbol{\omega}_O \times_G \boldsymbol{P}_I) + 2\,{}_G\boldsymbol{\omega}_O \times_G [{}_O\boldsymbol{\omega}_I \times_O \boldsymbol{P}_P]_O +_G \dot{\boldsymbol{\omega}}_O \times_G \boldsymbol{P}_I \end{aligned} \tag{3.28} $$

With the acceleration defined, all the necessary equations are available to generate a model describing the kinematics of the RPM. This can be used to investigate the resulting gravity level and other aspects of the moving RPM. However, before the model is complete, several more aspects need to be covered, such as the trajectory and control algorithms of the RPM.

3.2. Modelling the Movement

It is very important to understand the kinematics of the frames, as well as their motion with respect to the gravity vector. It should ideally point equally in all directions and result in a very low residual g-level but in reality, this is very difficult to achieve. When changing the rotational rates of the two frames, not only does the trajectory of the gravity vector change but also the resulting gravity level. However, a more “complete” trajectory of the gravity vector, covering more directions, is not necessarily equivalent to a lower g-level. This is why it is so important to understand the kinematics and their results before using an RPM for scientific research. Different experimental systems may require different controls, here *systems* refers to the various natures of samples being placed on the RPM e.g. plant cells, cancer cells, tissue or organoids. Some control algorithms work better than others, but only at certain rotational rates. This is why the kinematics of the RPM can be difficult to understand.

Even small changes to the rotational rate of either frame can result in completely different results when using constant rotational rates of both frames. However, it is also possible to adjust the controls using more advanced algorithms: this could be randomly changing rotational rates at random time steps, or using any more advanced continuous function to control the frames, one might even want to use a mix of algorithms to control the two frames individually. Only the imagination sets the limit on how to control the RPM, yet each control algorithm might have its own advantages and disadvantages depending on the system. As the RPM does not immediately reach the rotational rates but needs to accelerate at the beginning, the model is adapted accordingly, this is covered in Subsection 3.2.1. Details on the trajectory of the gravity vector are covered in Subsection 3.2.2. These trajectories are visualised with the unit sphere throughout this thesis.

3.2.1. Modelling Aspects

When the RPM starts a run, it accelerates to the required rotational rates. This can take a few seconds, which has an effect on the model, especially in the beginning, where the resulting g-level becomes more accurate when incorporating time for the acceleration compared to having the RPM instantly rotating at the correct rates. This acceleration is assumed to be constant and linear from rest to the required rotational rate. The time it takes to accelerate the frames varies between the different rates, however, to reach $120°\text{s}^{-1}$ the modelled acceleration time is $5\,\text{s}$. The acceleration is modelled equally for the inner and outer frames. Although they might vary a little bit when having two different rotational rates, if the rates are reasonably close, this difference is not important to the results. The main effect of the acceleration is within the first couple of minutes, after which both approaches, incorporating the acceleration or having instant rotation, average out about the same value. The difference between the two approaches is shown in Figure 3.5 and 3.6 for the start and end of a run, respectively. The measurements from the two sensors, that will be used for validation, are included to show the improvement at the beginning of a run when including the acceleration time. Looking towards the end, only the phase between the two approaches is slightly different. Hence, averaging the resulting g-level over a short time will lead to the same result for both methods. The sensors and their corresponding results are

discussed later.

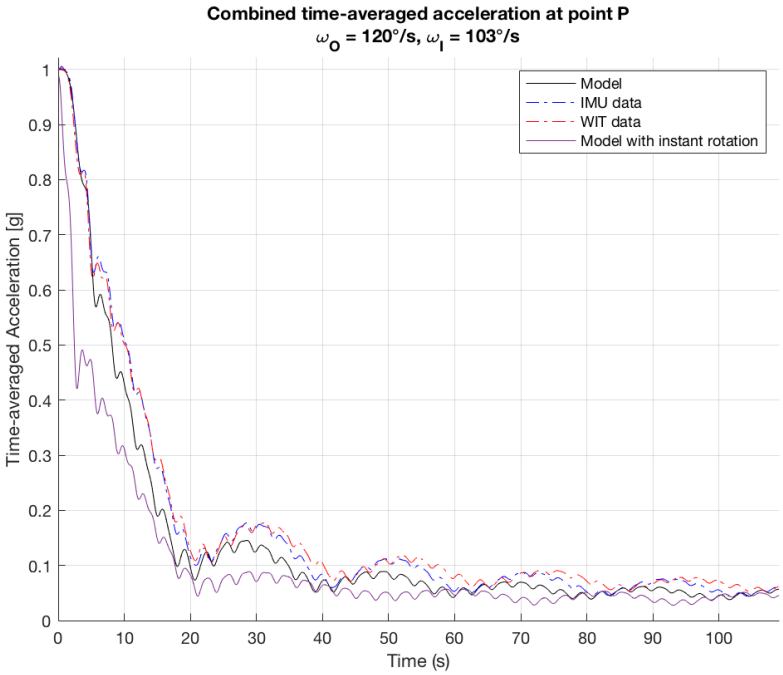

Figure 3.5: Difference between the models and sensors when using instant rotational rate compared to allowing the frames to linearly accelerate to the required rates. The dotted lines are the result of the two different sensors, and the solid lines are the respective approaches. Point P is taken to be in the corner of the experimental platform.

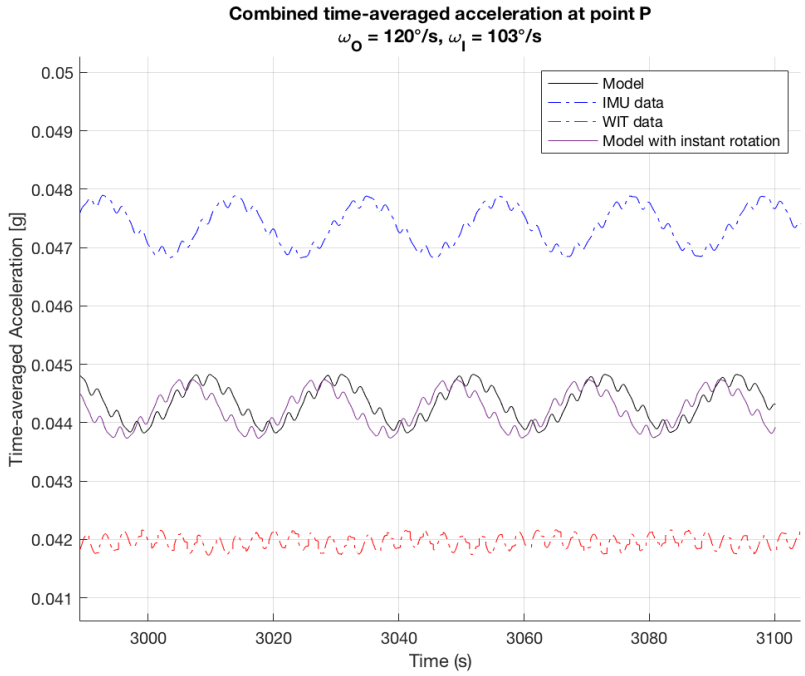

Figure 3.6: Difference between the models and sensors when using instant rotational rate compared to allowing the frames to linearly accelerate to the required rates. The dotted lines are the result of the two different sensors, and the solid lines are the respective approaches. Point P is taken to be in the corner of the experimental platform.

The second consideration regarding the modelling aspects concerns the way the accelerations are

implemented in the model. To gain insight into the RPM, they are calculated at each time step, and the average value of the current and all previous values generates the time-averaged acceleration. This value is used to address the behaviour a sample on the RPM would experience. The acceleration is calculated for each direction individually and combined to a mean acceleration μ_a. Mathematically, this is defined in Equation 3.29 and Equation 3.30 for the N'th time step. To ensure consistency, this method is applicable to all data, both from the model and the experimental data.

$$\boldsymbol{a}_{time\,average}(N) = \begin{bmatrix} a_{x_{time\,average}} \\ a_{y_{time\,average}} \\ a_{z_{time\,average}} \end{bmatrix} = \frac{1}{N}\sum_{i=1}^{N} \boldsymbol{a}_i \tag{3.29}$$

$$\mu_a = \sqrt{a^2_{x_{time\,average}} + a^2_{y_{time\,average}} + a^2_{z_{time\,average}}} \tag{3.30}$$

Finally, it should be mentioned that Matlab is used throughout this thesis to make the model as well as to analyse all the data gathered. The actual rotation of the RPM is in the negative direction for both rotations based on the adopted coordinates system shown in Figure 3.2.

3.2.2. Trajectory of the Gravity Vector Tip

The trajectory of the gravity vector tip can be computed using the rotational matrices from earlier. Gravity is constant, always pointing in the negative z_G-direction of the global reference frame. The angles of the outer and inner frames are therefore crucial when tracking the trajectory, as these are used to move from the global frame to the inner frame. Here, it is possible to draw the orientation of gravity with respect to a sample in the centre of rotation. For visualisation, the unit sphere is used with $1g$ on the axes, which corresponds to the orientation of the gravity vector with respect to the sample.

The angles are needed at every time step and are calculated by taking the angular velocity ω and multiplying it with the time t. However, as introduced above, the velocity is not constant at all times as the RPM needs to accelerate the frames first. To accommodate this in the case of constant rotational rates, the covered angle is calculated at each time step for that particular velocity and added to the previous result. Once the required rotational rates are reached, it becomes trivial to calculate the angle. As the velocity is constant, $\omega\, t$ can simply be added for every future time step, providing continuous knowledge of the angle.

As will be discussed later on, certain control algorithms can have different accelerations and can change the angular acceleration during a run. Hence, in these cases, it is important to implement the angles correspondingly to that algorithm. This will be done by calculating the angle as $\omega\, t$ for each time step and adding it to the previous value. This also ensures that, when the rotation is reversed, the angle is subtracted from the previous value for negative values of ω. This provides a continuous and accurate method for tracking the trajectory of the gravity vector.

Having defined the angles continuously makes it very easy to track the trajectory during a run. Simply applying the rotational matrices to the gravity vector and scaling it into a unit sphere of $1g$ will lead to the correct result. This is shown in Equation 3.31 where l indicates points on the trajectory and a_g is the gravitational acceleration with constant contribution in the global z-axis.

$$l = \boldsymbol{R_y} \cdot \boldsymbol{R_x} \cdot \frac{\boldsymbol{a_g}}{9.81} \tag{3.31}$$

3.3. Changing the Position of the Sample

Moving the sample away from the centre of rotation leads to imperfections in the rotation, as it can no longer be considered as a single point at the centre. This leads to new accelerations and forces acting on the sample. Until now there has been no precise formulation of the gravity level at certain distances away from the centre of rotation. The only indication scientists have is shown in Figure 3.7. This figure gives a simple overview of the resulting g-level and the most commonly used settings in the bottom left, in the grey area. However, the g-level depends on the control algorithm, and the individual angular velocities of the two frames individually, and the correlation is more complex than shown. A simplification like this, which does not contain the more complex aspects of the RPM, can potentially

result in completely different and invalid results in research. It can therefore be interesting to see how a change in the position actually affects the resulting g-level based on an actual control algorithm.

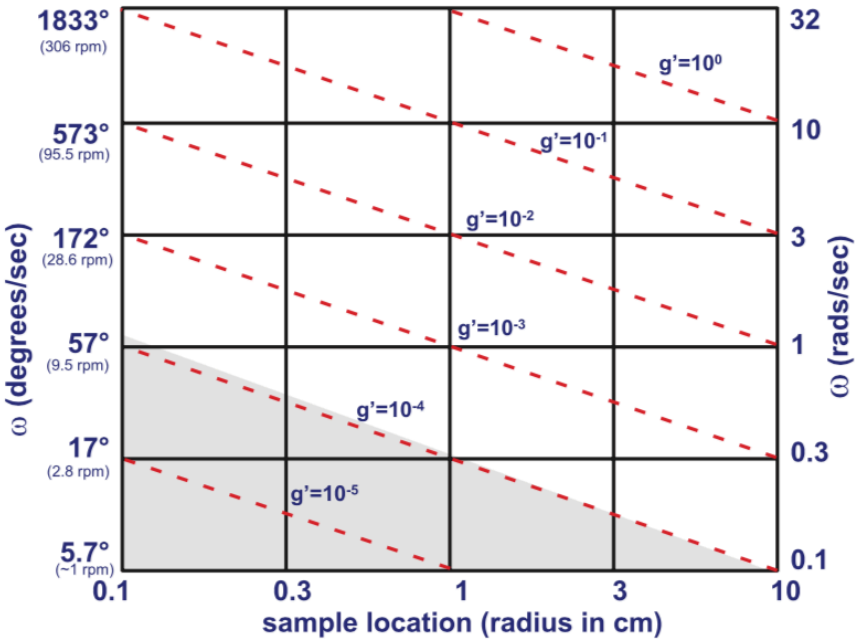

Figure 3.7: Residual g-level based on rotational speed and distance from the centre of rotation in an RPM [105].

However, it is not only just to evaluate how large an experiment or sample can be, it can also show new opportunities or limitations for sizing an RPM. When it comes to gravitational research, especially within biological samples, it is interesting to test the gravity dose response of certain biological materials. That means seeing how this material behaves at various gravitational levels as a step towards better understanding the influence of gravity. As it is possible to scale the RPM and introduce other g-levels away from the centre of rotation, it is interesting to evaluate how big an RPM need to be to simulate multiple g-levels in one run. Moving further and further away from the centre introduces larger accelerations, which at some point will equal the Moon's or Mars's gravity level. Biological materials develop over time, which is one of the reasons the RPM can be used to evaluate the effects of microgravity, as the sample's response to gravity is slower than the rotation. However, it also means that some systems need considerable time on the RPM to study the long-term effects of different g-levels. If it is possible to simulate multiple gravity levels at the same time, the required time it takes to perform the experiments can be reduced and it is possible to use a larger test sample in the results. Some systems need one month or longer on the RPM, hence studies can span for a very long time when investigating several g-levels.

This is the reason why a proper model for the RPM is needed, which takes into consideration the placement of a sample on the RPM itself. In the above kinematics, such a model is achieved and the placement can easily be adjusted to test the g-level at various locations.

3.4. Experimental Setup

Experiments are needed for validating the model of the RPM, these will be described in this section. Two different experimental setups have been used, firstly the use of motion capture to validate the movement of the RPM is discussed in Subsection 3.4.1. The second type of experiment contains IMUs and is explained in Subsection 3.4.2. For both tests, the Yuri RPM is being used at constant rotational rates. The controls of this RPM are pre-programmed, however, it is possible to choose individual constant rotational rates, which is the reason these are used to validate the model. The experiments were performed at various rotational rates to give a complete picture of the behaviour, compared to testing only one set of rotational rates. The RPM itself has the possibility to track the resulting gravity

level using its software, the results from this will be discussed in Subsection 3.4.3. The three ways to collect data require individual approaches for processing. However, they are converted into similar data using the same approach as outlined in Subsection 3.2.1, which will be used in the analysis. This ensures consistency between the data and the ability to compare the data.

3.4.1. Motion Capture

The motion capture system uses an OptiTrack V120 Trio camera, consisting of three cameras placed at different locations on the same line and a built-in license for the Motive software. This software allows tracking of markers on the RPM, which can be used for collecting data to analyse the movement of the RPM. The tests are done with the lights turned off in the room and the shades pulled down, to minimise the unwanted reflections of anything but the markers. The camera works best at a distance of around 60 cm or more from the markers, which means it should not be placed too close to the RPM. To hold the camera steady, a tripod is used as seen in the setup in Figure 3.8. To minimise the angle between the camera and the RPM, they are placed on two different tables with different heights. In case the camera is placed differently, this can be accommodated in the post-processing of the data by rotating the data according to the angles between the RPM and cameras.

Figure 3.8: Experimental setup of the motion capture at the Aerospace Physiology Laboratory.

The markers on the RPM can be labelled in Motive, so they are easy to find in the data afterwards. Since the license of the camera only allows tracking of markers, not objects, and the three individual cameras are on the same line, it is critical how the markers are placed. At first, it can seem smart to place markers on both the top and bottom of the platform on the RPM and based on these markers, track the orientation of the experimental platform. This however, is not a feasible setup as only one side of the platform can be tracked at any instant, and since it is not possible to create an object with the software licence, the top and bottom would be converted into two distinct parts. To overcome this, markers are placed on various locations of the inner frame, such that the cameras can almost continuously track the orientation of the inner frame. Whereas it is not possible to create objects, markers can be combined into forming rigid bodies, with the centre of the body being at the centre of the markers. These rigid bodies can be tracked by the software, which is a way of getting the orientation of the RPM without making an object. The view from the cameras can be seen in Figure 3.9. The top part shows the rigid body of the inner frame in blue together with its orientation. The markers on the RPM can be

seen as dots, with an extra dot in the centre marking the centre of the rigid body, the placement of the cameras is indicated by the orange objects. The three views at the bottom are the views directly from the individual cameras. The markers are here marked by white dots, and the red areas are masking implemented through the Motive software to ignore areas whose reflections are similar to the markers but do not contain any markers. In this case, the middle camera noticed the edge of the table the RPM stood on, whereas the left side camera detected a reflection on the wall. It is very clear that the markers would never be in these areas, making it valid to mask these areas, so the cameras would not detect anything here. The cameras have their individual views with different angles, making one camera catch reflections the others might not catch. However, the markers are easily caught by all three cameras making them more distinct and easier to track compared to random reflections.

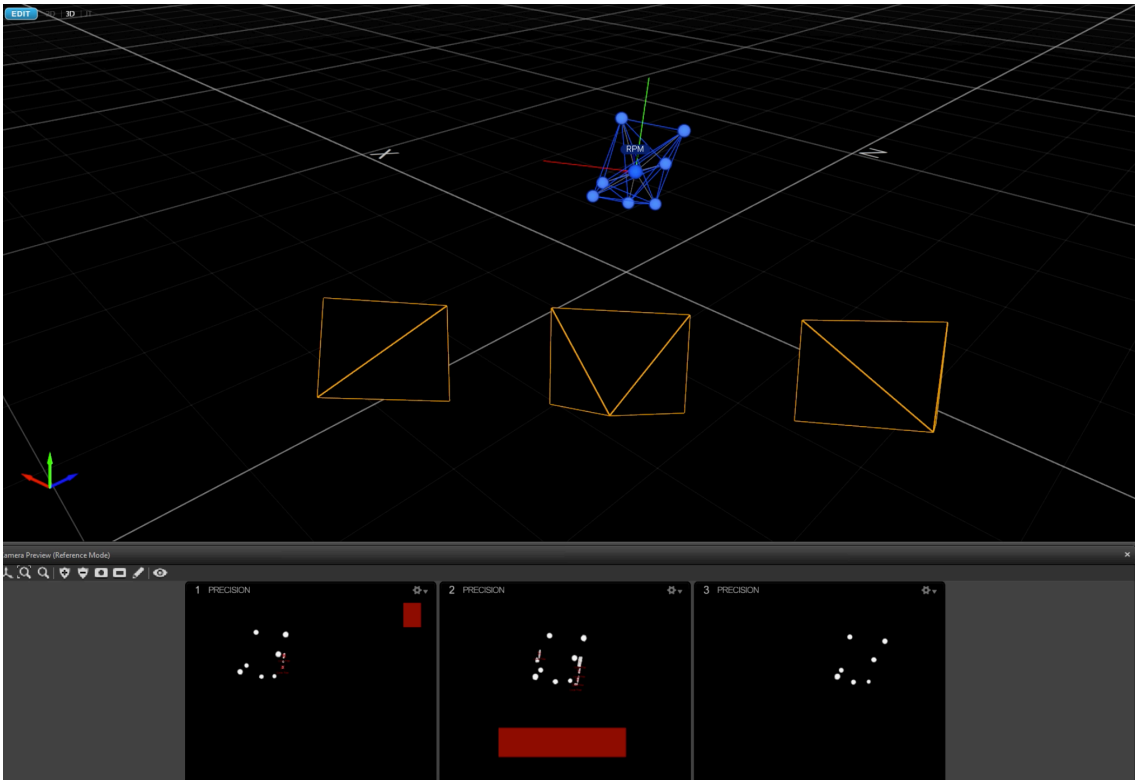

Figure 3.9: View of the Motive software while tracking the RPM.

To work properly, the cameras need at least 3 markers for identifying the rigid body of the RPM. This is not always possible to achieve during a run, as the markers would be hidden behind the bottom part of the frame at certain times during the rotation. Placing the markers strategically will ease the tracking, as any three markers can be used to track the orientation. Having the markers form unsymmetrical and easily separable patterns can improve the tracking when only a few of the markers are visible. The cameras do not realize how the RPM moves, meaning that if the markers are placed symmetrically, the orientation of the RPM could technically be one of multiple options, whereas unsymmetrical placement offers greater precision in recognizing the orientation.

The next step in the process is to realize that the bottom of the inner frame follows a distinct path around the unit sphere exactly opposite, mathematically, to the path of the gravity vector. The RPM furthermore has three holes in the inner frame, making it possible to place a marker exactly at the centre of the bottom of the inner frame. To let this marker be visible almost continuously, the biggest possible marker is set here, such that it extends beyond the upper and lower part of the hole as much as possible. The cameras cannot always track this marker, but as the data will show later, at almost all times will the placement of this marker be known. This is a way to simplify the tracking and easily extract the orientation data at a higher quality, compared to using the orientation generated by the software. As seen in the videos linked in Figure 3.10 and Figure 3.11, jittering occurs occasionally in the orientation, which makes this method for tracking less precise. On the other hand, the one marker at the bottom is

tracked very smoothly at almost all times, which is why this is a good option for tracking the RPM.

The trajectory of the inner frame in the global reference frame, which is tracked by the motion capture system, can be described mathematically by following the point located at -1 on the z-axis of the inner frame. To convert this to the global frame this point needs to be rotated first around the local y-axis, and then the x-axis. This is shown in Equation 3.32 and is opposite to the rotation of the gravity vector tip, which was shown in Equation 3.31 and is listed again below in a slightly different form in Equation 3.33. Here the rotation is taken from a point located at -1 on the z-axis in the global frame. This point was then rotated around the x-axis and then the y-axis to show how the gravity vector would point inside a sample placed on the RPM following the orientation of the inner frame.

$$l_{global\,frame} = \boldsymbol{R_x} \cdot \boldsymbol{R_y} \cdot \begin{bmatrix} 0 \\ 0 \\ -1 \end{bmatrix}_{inner\,frame} \tag{3.32}$$

$$l_{inner\,frame} = \boldsymbol{R_y} \cdot \boldsymbol{R_x} \cdot \begin{bmatrix} 0 \\ 0 \\ -1 \end{bmatrix}_{global\,frame} \tag{3.33}$$

There are therefore two distinct trajectories presented throughout this work. One shows the trajectory of the gravity vector in a sample, and the other shows the trajectory of the inner frame, which is comparable to the motion capture data. It can be noted, that switching the rotational rates of the two frames is equivalent to switching the order of rotation about the x and y-axes. In every applicable figure, it will be indicated if the trajectory is of the inner frame or the gravity vector, which corresponds to either of the above two approaches to visualise the trajectory. The trajectory of the inner frame will only be used in relation to the motion capture results.

Figure 3.10: Motion capture recording of the RPM at ω_I = 18°/s and ω_O = 24°/s. `https://mitprod-my.sharepoint.com/:v:/g/personal/lbruun_mit_edu/ES1KfbyHJc1IkbR4akSuP_IBc1lYtrs7hHJlOnnq1HlERg?e=lp46iL`

Figure 3.11: Motion capture recording of the RPM at ω_I = 18°/s and ω_O = 24°/s. `https://mitprod-my.sharepoint.com/:v:/g/personal/lbruun_mit_edu/EY3OTEcEDjJIlq3rLWqYSQcBfyDQWYonQAFDBTNj-aM_gQ?e=yUiOmm`

One problem, however, is the surfaces of the RPM reflecting light similarly to the markers, especially the grey and silver parts of the RPM, i.e. the structural frame, the screws and the gears. To accommodate for this, black tape is used to cover these surfaces to minimise the number of unidentified markers in the data. It is not possible to eliminate all unidentified markers during a run, as even the black tape would occasionally reflect light in a way the cameras would detect. However, having defined the markers on the RPM as a rigid body makes it very easy to clean up the data of unidentified markers, as they are automatically separated by the software. These markers will generally only be recorded for a couple

of frames, which means they are distinctly different from the labelled markers, which have continuous data at all times they are visible. An example of how these unidentified markers are seen from the cameras is shown in Figure 3.12. Usually, the reflection will be visible at only one camera, however in the figure there is also the example of two cameras spotting the same reflection. When the unidentified markers are small, it can be more difficult to state whether or not they are one of the markers, however, as mentioned, the software automatically categorises the labelled and unlabelled markers making it easy to distinguish between them.

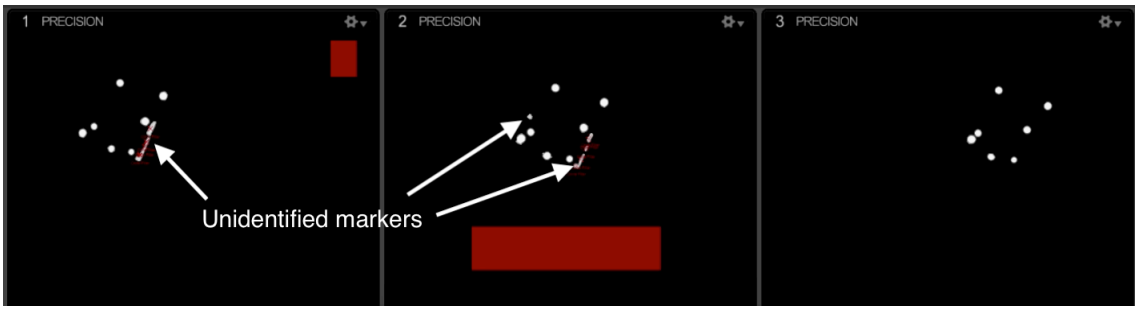

Figure 3.12: Example of unidentified markers seen from the cameras during recording.

The experiments were not all run on the same day, and two slightly different setups for the placement of the markers were used. At first, 10 markers were used on the RPM. These were placed to cover most parts of the inner frame, to ensure that at least three markers would be visible at most times. The markers were indeed visible most times, however, the software had difficulty figuring out exactly which markers were visible at any time. Due to the many markers, the different markers did not make distinct enough patterns for the tracking software, which caused this challenge. During these runs, the orientation had jumps and irregularities when the software thought it was a certain three markers it could see, then it turned out next frame or a few frames later, that it was actually not those three markers. This leads back to the importance of the placement of the markers on the RPM. To minimise the irregularities, the markers were replaced and reduced in number, so only 7 markers were used. They were also placed at various locations to make distinct patterns, so the software more easily could track the orientation. This setup is shown in Figure 3.13, where 6 of the 7 markers are visible. While they needed to be placed to improve the tracking ability, they also needed to be placed such that the centre of the rigid body they form in the software, would be very close to the centre of rotation. This ensures that the orientation is tracked correctly. Despite the two different approaches, the best tracking data was gathered from only one marker, which was placed at the same place during all runs, therefore having two different approaches will not affect the final result. This specific marker can also be seen in the centre hole of the inner frame in Figure 3.13. The recordings capture 120 fps which is enough to study the movement of the RPM.

Postprocessing of the Motion Capture Recordings

Now the experiment has been described, the focus will be on the post-processing of the data. This is an equally important aspect required for validation. The first step in the Motive software is to remove all the unidentified markers from the data. Once this is done, it is possible to export the data containing only information on the markers and the rigid body formed by the markers. Each marker is labelled together with its values in x, y and z-coordinates and the values are given at each frame for all markers. When a marker is not visible to the cameras, it can be that the values for that marker are left blank for the specific frames. The marker placement inside the exported document is not the same throughout the runs, not even runs taken sequentially. Therefore, the specific marker number used to generate the tracking data is noted down for each run. When extracting the data into Matlab, each marker's specific placement should be entered manually.

With the correct marker and its corresponding data imported, data is aligned to match the coordinate system of the model: this was shown earlier in Figure 3.2, and it requires the x, y and z-direction of the motion capture system to actually be changed, such that the new x-values are the negative z-values of the motion capture system, then the new y-values becomes the old x-values and the new z-values will

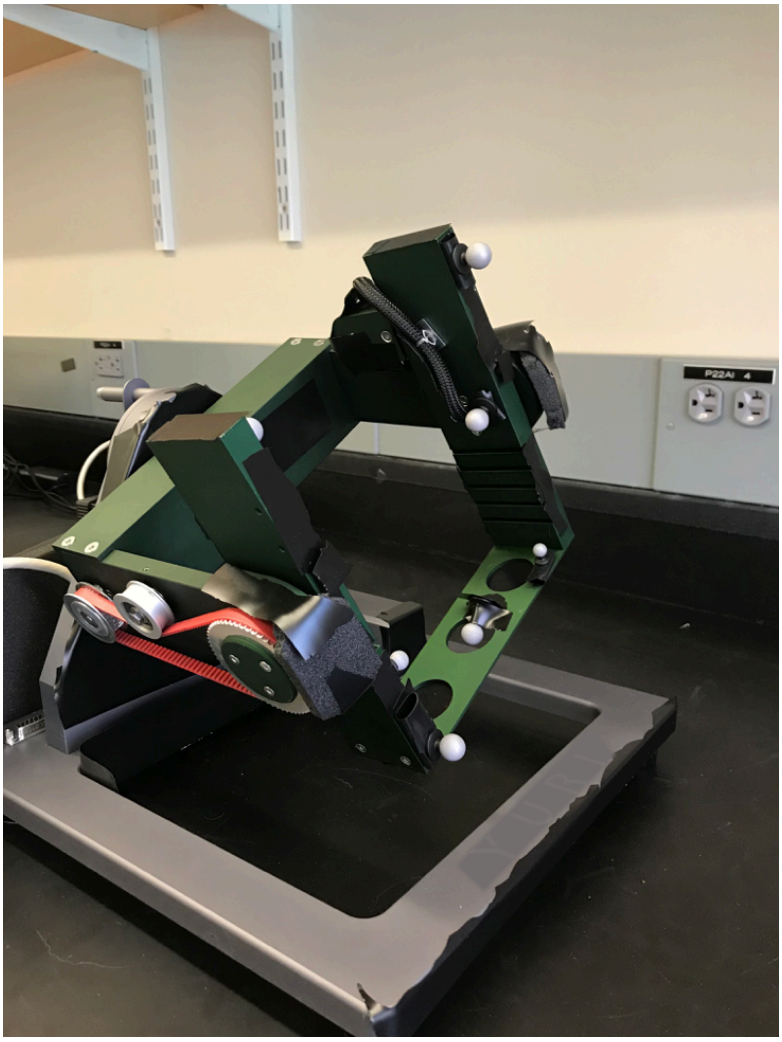

Figure 3.13: Experimental setup at the Aerospace Physiology Laboratory.

be the old negative y-values. This is shown in Equation 3.34 for clarity. However, the axes do not yet correspond correctly, as the motion capture cameras have a certain angle with respect to the RPM and its coordinate system. The next step is therefore to rotate the coordinates accordingly. This is simply done using rotational matrices. The last step is to rescale the data from the motion capture system to that of the RPM. The data points in the motion capture system do not automatically fit the sphere of movement generated by the model as the data points are taken at a different scale.

$$\begin{bmatrix} x \\ y \\ z \end{bmatrix}_{inner\,frame} = \begin{bmatrix} -z \\ x \\ -y \end{bmatrix}_{Motion\,Capture} \tag{3.34}$$

With these small steps and correct scaling, it is possible to plot the trajectory of the RPM, both the theoretical one and the recorded trajectory from the motion capture system. The results from this will be discussed later in Section 4.2.

3.4.2. Inertial Measurement Units

There are two different parameters to be changed throughout the experiments with the IMUs, that is the individual rotational rates of the frames and the distance from the centre of rotation to the sensors. The rotational rates are chosen in a wide range so they cover various ratios of the inner and outer frame rates while also allowing a variety in rotational rates to uncover details related to the increase or decrease in rotational rate. Covering various ratios between the inner and outer frame rates allows

uncovering how the trajectory changes and which effects this has on the resulting g-level.

To gather the data, two IMUs are used. The first one is the BWT61CL accelerometer from WitMotion, and the second one is the Delsys Electromyography (EMG) sensor. However, it is clear that for this purpose not all the capabilities of the EMG is used, instead it is used solely as an IMU to measure accelerations. Having two distinct sensors can help to evaluate their performance while also allowing more data to be gathered in less time. When running the RPM, it takes at least 30 min until the resulting gravity level stabilises. All of the performed runs were longer than 30 min and generally a run would be recorded for around 45 min to ensure the resulting gravity level had stabilised. Some of the runs are longer, however. Overall, it means that using an extra sensor significantly reduces the time used for performing experiments while also providing a way to directly evaluate the sensor quality by comparing data from the two sensors.

The IMUs are placed such that their coordinate system is aligned with that of the model and the RPM. Generally, the accelerometer sensor is significantly smaller than the casing of the IMUs. For the Delsys sensor, it is assumed that the accelerometer is in the centre of the casing. For the WIT sensor, this is not the case. Pictures provided by the company show that it is slightly off-centre towards one side, however, the exact distance could not be provided. It is estimated that this off-centre distance was around 10 mm, which seems reasonable based on the picture. The dimensions of the Delsys casing were 24x36x13 mm in width, length and height respectively. For the WIT sensor casing, these values were 36x46x15 mm. When run simultaneously, the two sensors are placed diagonally from each other, at the same distances from the corner. Both dimensions of 36 mm align with each other, and since the sensor was off-centre towards the edge of the RPM, it is very easy to place them as they are then placed exactly the same distance from the corner. The accelerometer component of the WIT sensor might be a couple of mm from the actual modelled spot, however, as the results will show, one or two mm are not significant. At the very edge, moving the sensor 1 mm further away from the centre will theoretically affect the results by $4 \cdot 10^{-4} g$ at the highest operational speeds of ω_O = $120°\text{s}^{-1}$ and ω_I = $103°\text{s}^{-1}$. This is less than 0.9% of the resulting gravity level at this location. For this purpose, it is therefore a reasonable assumption.

A limitation of this method is that the actual sensor placement can vary. Multiple runs are made with the sensor at the same location but on different days, such that the placement of the sensor may have several actual locations, that vary a little bit. This is done to see the influence of placing the sensor, while it also gives more data points to be analysed. This can help understand the impact of placing the sensors this way.

The WIT sensor is calibrated before each run, this includes calibration of its acceleration measurements and aligning its reference frame with the starting position of the RPM. The Delsys sensor cannot be calibrated manually and will need some time from the measurement starts until it reaches a stable measurement. This is in the order of 15 s. Each of the two sensors is discussed individually in the subsections below. Details on post-processing and data handling for each of the two sensors are also included. As the output data is collected in different formats, two different methods are adopted to convert the data to be able to analyse it. In the text and corresponding data files, IMU refers to the Delsys sensor, whereas WIT refers to the WitMotion sensor. This is the notation adopted throughout this thesis.

IMU Sensor

Due to the IMU from Delsys needing at least 15 s to 20 s before reaching a steady state, as well as its need for correction of bias, the data will need postprocessing before it can be analysed. Data is exported through Delsys software to a .csv file, that contains all the measurements of all the parameters. Since the IMU collects a vast amount of data and significantly more than what is required, some of the data is removed. To be specific, the IMU collects data at approximately 1111 Hz, whereas around 10 Hz would be sufficient to generate a continuous function of the gravity level similar to the model. To have a smooth function from the IMU measurements, every 20th line in the data set is rewritten into a .txt file, that can be used for the analysis. This gives around 8-10 data points every second, meaning the sensor does not collect at 1111 Hz as stated by the settings but slightly lower. However, it leads to a continuous function similar to the model of around 10 Hz. As the IMU is an EMG, it measures additional variables and not just the acceleration. In the .txt file, only the relevant variables are included. Taking

these two steps allows the processing time to be minimised, as the file has significantly fewer data points.

The start time of each run is noted, making it possible to remove data points of the IMU before the starting point. Not all the data points will be removed, however. As there is bias in the measurements, the measured values of around a second before the start will be used to correct this bias. At this point, the IMU has reached a steady state in its measurements and the bias can be taken from the data just before the start. The data points before the start are averaged out, and subtracted for the relevant direction. When this has been done, the time-averaged acceleration is computed and plotted, such that the result can be compared with the model.

WIT sensor
When used for the same runs, the WIT sensor is placed diagonally opposite of the IMU sensor. The only difference here is that the point P, where the sensor is, now has a different x and y-coordinate. Instead of being negative, they are now positive but have the same value. Unlike the IMU, the WIT sensor uses all data points and with the calibration before each run, it is only rarely needed to correct for bias. The data is measured in $\mathrm{m\,s^{-2}}$ with gravity defined as $10\,\mathrm{m\,s^{-2}}$, which means that this data is divided by 10 to get values in g for this specific sensor. It is very easy to decide when the run starts for this data, the sensor is started after the IMU and it has a very clear jump from zero to new values at the beginning of a run. With this clear jump, the data before the start can be removed.

The results are computed and plotted in Matlab similarly to the IMU sensor and can be compared to the model. The accuracy of the sensor is $0.01g$ and a stability of $0.005g$.

It is important that the data files only consist of data points from the beginning, as the time-averaged acceleration is calculated. If all the data before the start are kept in the files, these will be included in the calculations, making the time-averaged acceleration less sensitive to the actual changes in gravity during a run.

The measurements of the sensor do not show any bias prior to testing, however, the results do contain some bias and small drifting which is revealed when plotting the data. To evaluate these discrepancies, runs were made where the sensor after a run was brought back to the initial starting position to quantify the changes in acceleration measurements compared to the start. Applying this did not result in any conclusive outcome, as the differences after a run were small and in the order of $0.008g$ in only the y-direction, which had no significant effect on the overall result when accounted for. This was the case both when it was modelled as a drift occurring over the duration of the run and when it was modelled as bias. It is expected there will be some inaccuracy in the WIT sensor's measurements but by making multiple runs at the same settings it will be possible to evaluate the range of its measurements. This is done in the following chapter when presenting the validation of the model.

3.4.3. Recorded Gravity Level from the RPM

The last and most important component of the experiments is the RPM. The only commercial available RPM is from Yuri and is being used for the experiments. This RPM was developed in 2000 to fit inside a standard-sized incubator. The platform, which can support experiments, is 15.9 x 14.6 cm. This platform is very limited when trying to validate the accelerations when moving away from the centre of rotation, which means that higher rotational rates are required to make the accelerations substantial. The RPM is straightforward to use, however, there are several options for controlling it. The first option is to generate a completely random movement. This movement can be changed from run to run and will not necessarily cover the same path. It is possible to choose the maximum and minimum rotational rate for the two frames individually and then start the run. The change in rotational rate occurs at random times as well. The next option is to use one of the pre-programmed g-levels. They range from $0g$ to $0.9g$ in increments of $0.1g$, as well as specific options for Moon and Mars g-levels. Using these pre-defined paths means, that it is possible to run that specific path again. The paths are defined for 24 hrs, after which they start over, running the same path again for the next 24 hrs. The third option is to run the RPM at constant rotational rates between 0 and $120°\mathrm{s^{-1}}$. The rates can be chosen individually for both frames. This also yields the possibility to use the RPM as a clinostat, simply by keeping one frame from moving. The starting positions of the frames will determine how the clinostat rotates and whether it simulates microgravity horizontally or vertically. Finally, it is possible to turn the frames at a

specific angle, after which they stop. The RPM can in the other three modes be stopped at any time, and if no input is given, it will continue to rotate.

As mentioned earlier, the experiments will use constant rotational rates, as these can be controlled by the user to specific values. The other options will not allow comparison to the model as the algorithms are proprietary. It is also not possible to write custom algorithms and export those to the RPM, which limits the algorithms discussed later in Chapter 5 to be tested on the model only. The slowest set of rotational rates for the frames is ω_I = $12°s^{-1}$ and ω_O = $24°s^{-1}$ and the fastest is ω_I = $103°s^{-1}$ and ω_O = $120°s^{-1}$. Various sets resulting in different ratios between the rates of the inner and outer frame will be used to validate the model.

Before an experiment is started, it is important to align the *home* position of the RPM such that gravity points vertically down on the platform. This will give the correct results, as the RPM is designed such that the required g-level is only valid from this starting position. It is an easy process to define the home position by simply releasing the frames, placing them correctly and defining that as the home position in the software. Using a wrong home position will lead to wrong results: this is especially critical for partial-g modes. It should be clear that the resulting g-level should not be at an angle compared to the sample.

During a run on the RPM, it is possible to track the resulting g-level based on a model included in the software. It should be said that the movement of the RPM is defined by lines of text in the path files, which define the sequence of positions of the frames. These lines define waypoints of the RPM, which is used to model and track the resulting g-level. The average g-level is calculated by the software as shown in Equation 3.35, where x, y and z indicate the acceleration level in the corresponding direction. This average value only applies at the centre of rotation and cannot be translated to different places on the RPM. Since its development more than 20 years ago, the RPM has been validated including its output of the gravity level. This was done when Airbus still had the rights to the RPM using sensors but currently, no sensors are included on the RPM.

$$g_{av} = \sqrt{x_{av}^2 + y_{av}^2 + z_{av}^2} \tag{3.35}$$

Certain jumps can be seen in the resulting g-level using the software. This is shown in Figure 3.14, where there is a clear and sudden jump in the average acceleration in the y-direction. Due to these jumps, there will be expected to be some deviations between the model and the RPM data, especially on runs less than one hour long, where these jumps affect the overall g-level. This is easily seen in Figure 3.15. Over very long durations, it is assumed these jumps will average out, as they also occur in the opposite direction. They will therefore be less and less noticeable as it takes an increasing amount of data to affect the average g-level due to the increasing amount of data collected as time progresses.

There are five slots on the RPM in which the platform that holds the experiments can fit. These range at 23 mm when it is closest to the rotation axis to 75 mm when it is placed furthest away from the rotational axis. The intermediate steps are placed at the same distance between each other of 13 mm. This means, that the sensors are not placed directly at the axis of rotation, as they are less than 23 mm tall. In reality, the sensors are placed 16.5 mm from the rotational axis in the z-direction, assuming the sensors are located in the middle of the cases. At slow rotations, this small discrepancy does not affect the results making it possible to compare measurements from the sensors to the model and the average g-level modelled by the RPM. However, at faster rotations, this small distance affects the results and the RPM's predictions should not be included in the analysis and validation.

It should also be noted that the rotational rates implemented do not exactly match the chosen rate but can vary slightly. This is the case in certain experiments and can be seen as a shift in the phase of the model compared to both the RPM and the sensor data. Modelling at a rotation that is $0.1°$ lower can visibly improve the results, leading to the model and the data having the same phase. The amplitude of the resulting g-level is unaffected by this and will stay between the same maximum and minimum values. This can explain why the model has a slightly faster frequency in each direction during an experiment.

The RPM also has counterweights installed but these are not changed or actively used during exper-

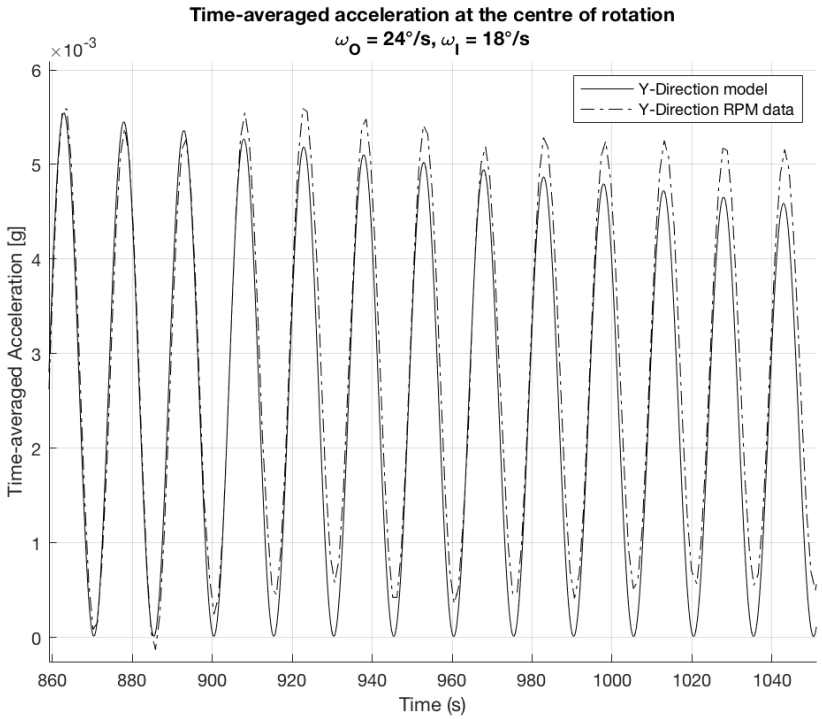

Figure 3.14: Jump in the y-direction in the modelling of the resulting g-level by the RPM software. This jump is not seen in the model.

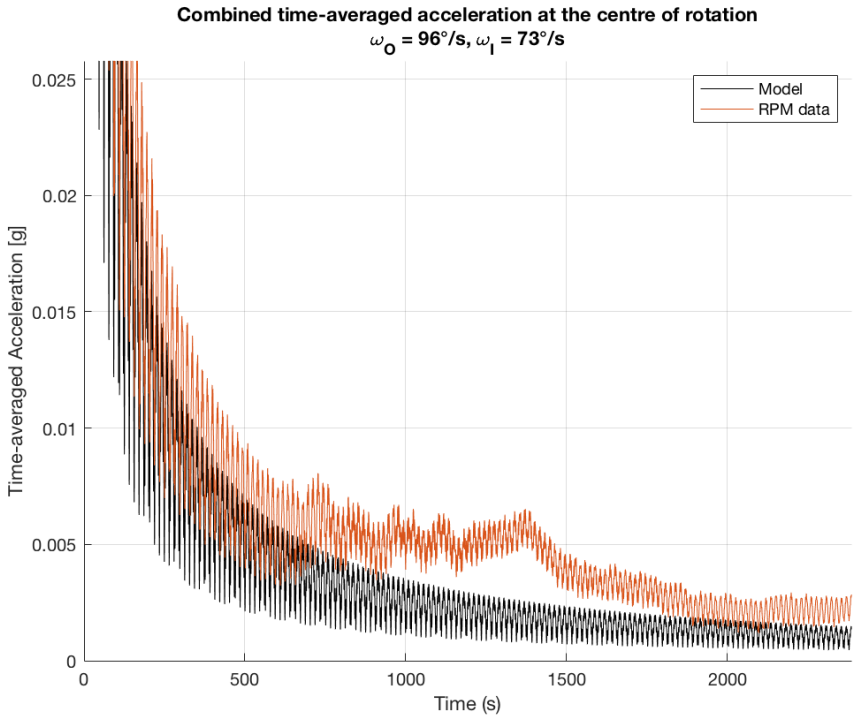

Figure 3.15: Jumps in the RPM data affect the overall time-averaged g-level noticeably.

iments. When using the counterweights, it is important to tighten them, so they do not slide around when the RPM is rotating. This can introduce vibrations and shocks in the experiment.

4

Validation

It is crucial to validate the model and ensure that it shows the correct accelerations before it can be used for anything else. Therefore, this chapter will look at the data from the experiments and compare it to the model predictions. The first step is to compare the accelerations experienced during a run in Section 4.1. This includes evaluating the accelerations at different rotational rates and various distances from the centre of rotation. This is followed in Section 4.2 by an assessment of the trajectory of the RPM and the motion capture system recordings. It will then be shown that the RPM is actually drifting at certain rotational rates in Section 4.3 as the frames do not reach the precise rotational rates. The velocities of the measurements and model are shown in Section 4.4. This is followed by an evaluation of existing alternative models in literature in Section 4.5. To end this chapter, a few conclusive notes on the validation are presented in Section 4.6.

4.1. Comparison of Accelerations

There are two variables in the experiments, the rotational rates of the frames of the RPM and the distance from the centre of rotation to the sensors. At the centre, no other acceleration than gravity will affect the samples, which makes this a trivial case to solve. This can be done using the rotational matrices and Earth's gravity. Interesting aspects appear when one tries to move away from the centre of rotation, where multiple sources of acceleration are present and can become dominant. The results from varying locations on the RPM are discussed in Subsection 4.1.2. Here, both the case when measuring the acceleration at the centre of rotation, at an intermediate distance from the centre, and at the corner of the platform are shown. Since the RPM has a rather small platform, the rotational rates need to increase in order to measure significantly different acceleration levels between the centre and the corner location. This leads to the next important element that affects the resulting accelerations, namely the rotational rates of the two frames. By changing the rates individually, it is possible to achieve different acceleration levels and different trajectories of the gravity vector tip. This is outlined in Subsection 4.1.3. First, the sensitivity of the sensor measurements will be discussed in Subsection 4.1.1. This is done to see how the sensors behave using the same settings during different runs.

4.1.1. Sensitivity of the Measurements

The measurements of the sensors can differ both due to slight variations in the locations they are placed as well as due to bias or drift in their measurements. For the IMU sensor, this bias is automatically found by averaging the measurements one second before the RPM starts rotating. The bias cannot be determined this way for the WIT sensor, hence the measurements by the WIT sensor generally include potential bias. To understand how sensitive the measurements are, several runs are performed with the same settings to display potential errors.

The measurements of the WIT sensor are generally not spread as much as the IMU data. There is more noise in the IMU data whereas it also contains extreme outliers occasionally. The measurements vary between 0.85 to $1.15g$ with the outliers lying at $0.04g$. The WIT sensor varies in measurements

between 0.9 to $1.1g$ and very clearly has a similar periodic shape to the model, this shape is far less distinct for the IMU sensor. This can be seen in Figure 4.1.

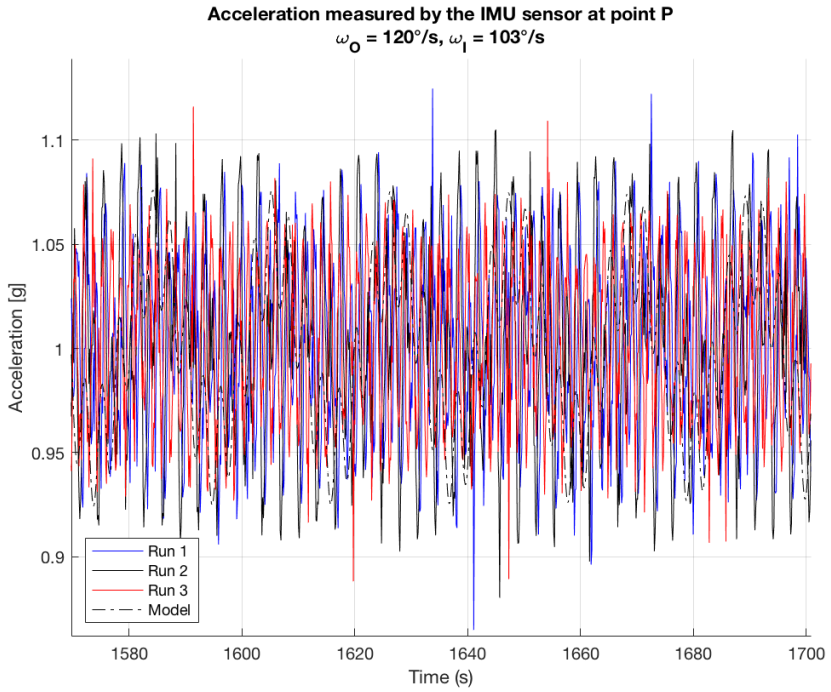

(a) IMU sensor

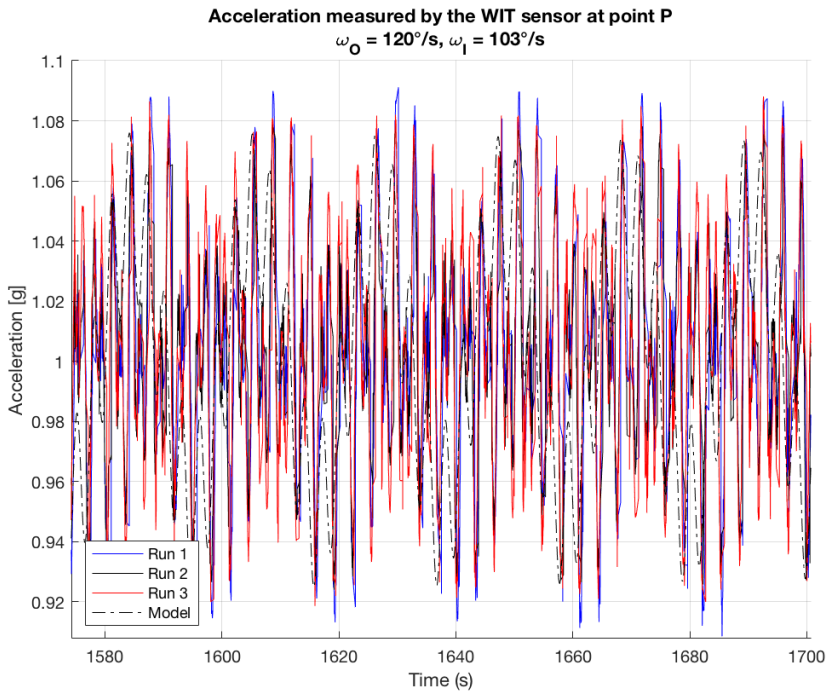

(b) WIT sensor

Figure 4.1: Data from three runs at $\omega_I = 103°\text{s}^{-1}$ and $\omega_O = 120°\text{s}^{-1}$. Figure a shows the IMU sensor and figure b shows the WIT sensor

Whereas the WIT sensor has less noisy data, its bias changes during each run, resulting in some more different overall results each time. Unless considering the model or the IMU data to be true, there is no way of determining this bias correctly as it does not show up when the sensor is static. Throughout

the runs, it consistently underestimates the acceleration in the x-direction while overestimating the acceleration in the y-direction compared to the IMU sensor. When looking at the IMU sensor, the results are very similar across the three different runs and only vary by $0.002g$, this is so low that the result is not shown here. For the WIT sensor, the variation is $0.015g$ but the shape also differs as shown in Figure 4.2. This different shape is caused by an overestimation of the acceleration in the y-direction, which has a higher frequency compared to the other directions. When this becomes more dominant it affects the shape of the time-averaged acceleration. The difference between the tests can be a result of a difference in the bias of the respective runs and exceeds the accuracy of the sensor of $0.01g$, that was claimed by the producer.

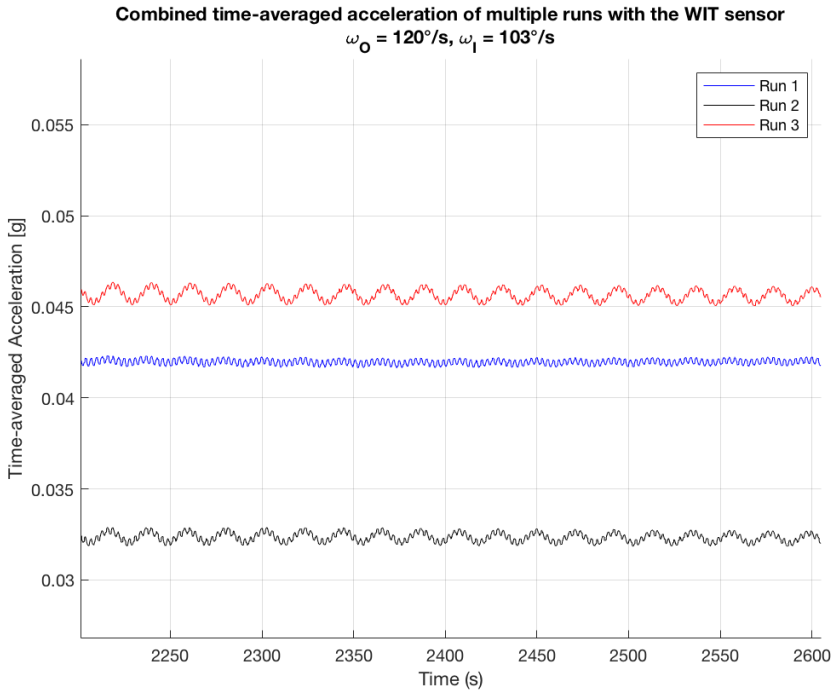

Figure 4.2: Time-averaged acceleration measure by the WIT sensor after 40 min at ω_I = $103°s^{-1}$ and ω_O = $120°s^{-1}$.

The IMU sensor shows very consistent results, whereas the WIT sensor shows less noise in the data. However, for this purpose, small errors and differences in the measurements become very obvious as the resulting g-level tends to be very small and approach $0g$ as the RPM comes close to simulating microgravity. To get rid of this uncertainty, one would need a very accurate accelerometer that can be spun around connected to the RPM. This is outside the scope of this thesis and the results from the two sensors will be used to evaluate the model validity.

4.1.2. Varying Distances from the Centre of Rotation

At the very centre of rotation, the only data collected is from the RPM itself. As the highest slot for the platform is placed 23 mm below the axis of rotation of the inner frame, it is not possible to place the sensors accurately at the centre of rotation without additional hardware. At very low rotational rates, the additional accelerations are very small and not the main source of the error between the model and the data. In Figure 4.3 and Figure 4.4 the beginning and end of a run at ω_I = $18°s^{-1}$ and ω_O = $24°s^{-1}$ is shown, respectively. The sensors were placed at the corner, whereas the RPM data is modelled at the centre of rotation. In all plots, the acceleration is on the vertical axis and time is on the horizontal axis. In these figures, the modelling has been done at the corner of the platform and thereby at the sensor location. Overall, there is a very good coherence between the model and the sensor data. Towards the end, some small discrepancies between the model and the other data can be seen, which is interesting to look closer at even though the resulting g-level is similar.

In this specific example, the bias from the WIT sensor is removed by using a theoretical value, as it is

supposed to be close to zero. The RPM data has been validated throughout the years by Airbus and used to have a sensor on to measure the acceleration level. This means that at low rotational rates where the main contribution is from Earth's gravity, it is possible to find the theoretical bias. It is not possible to do this when the RPM rotates faster and for these results the bias is not accounted for. The WIT data can be seen in Figure A.1. The WIT data has a time-averaged acceleration of $0.028g$, an order of magnitude above the rest of the data induced by the bias.

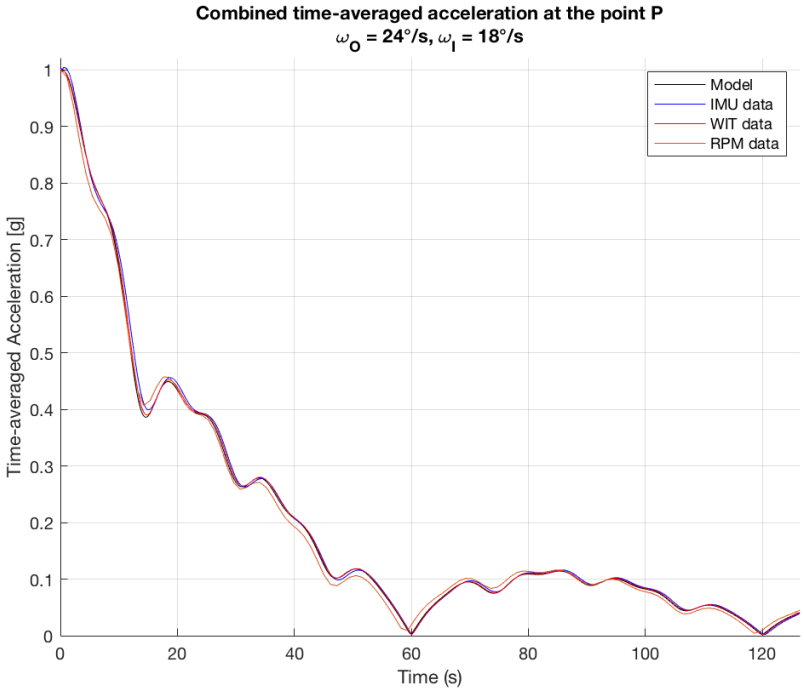

Figure 4.3: First 120 s of a run with the time-averaged acceleration on the vertical axis and time on the horizontal axis. The model and the two sensor data are taken at the corner of the platform, whereas the RPM data is taken from the centre of rotation.

As mentioned earlier, the additional accelerations are not yet significant for this case of low rotational rates, however, there are still some very interesting points to make based on the discrepancies. For the first point, it is interesting to look at the measured g-level in each individual direction. In Figure 4.5 it is clear that very small deviations to the actual rotational rate result in different measurements. The resulting g-level will reach the same level, however, the phase of the measurement is very different. The model is ideal and will always be based on the exact rotational rates, the sensors will, however, not be measuring at the ideal rotational rates, as the RPM is just not accurate enough. Again, this only causes phase shifts and does not significantly affect the overall resulting g-level, the effect is in the order of $10^{-4}g$. The phase shift is only shown in the x-direction but it is also valid in both y and z-direction. As it is very difficult and time-consuming to find the exact rotational rates of the RPM, it will not be done at other rotational rates. This can explain potential phase shifts in future graphs. This is mentioned where it is relevant. Both Figure 4.5 and Figure 4.6 show how the modelled and measured acceleration for the individual directions match each other. The results are similar in the z-direction, indicating that the model is very good at predicting the acceleration levels in each direction. The differences in the time-averaged acceleration appear due to the very small differences which are in the order of $10^{-3}g$.

When adjusting the model to be at the centre of rotation, it fits the pattern better with the other data. In Figure 4.7 the result is shown with only the RPM and the model. This improved correlation makes sense as the additional accelerations do not come into play now and generate the more trivial case where only the gravitational acceleration should be considered. Based on this, it would be expected that the sensors show a better correlation to the model when measuring from the corner of the platform, rather than the RPM data that is taken from the centre of rotation. This is not the case, however. The sensors seem to be closer to the RPM data compared to the model, however, at these slow rates the

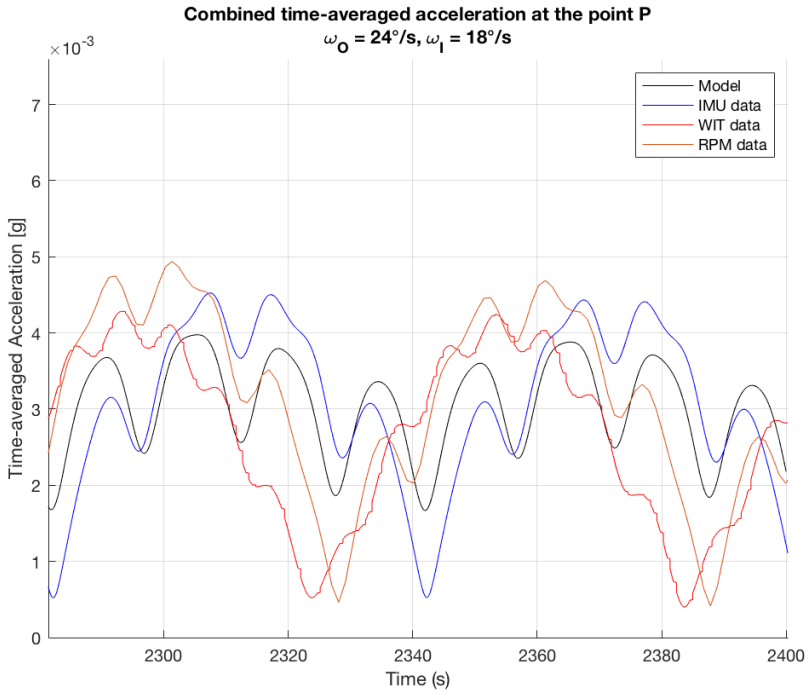

Figure 4.4: The time-averaged acceleration after 38 min of a run in the RPM. The model and the two sensor data are taken at the corner of the platform, whereas the RPM data is taken from the centre of rotation.

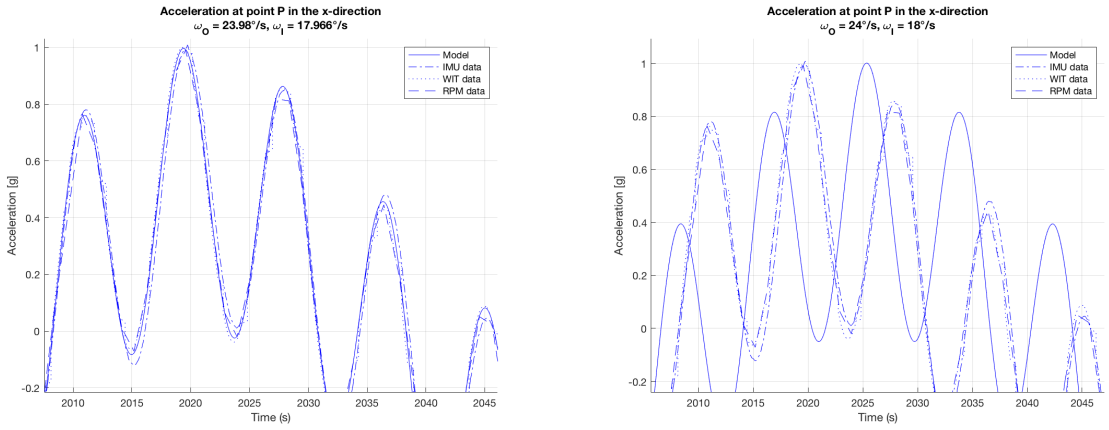

(a) ω_I = $17.966°s^{-1}$ and ω_O = $23.98°s^{-1}$

(b) ω_I = $18.0°s^{-1}$ and ω_O = $24.0°s^{-1}$

Figure 4.5: Phase shift in the x-direction due to very small inaccuracies in the actual rotational rates of the frames. Figure a shows the actual rotational rates of the RPM, whereas figure b shows the ideal rotational rates.

additional accelerations are not very dominant and looking closer into the values of these can reveal some of the underlying reasons for the slightly different sensor data. It can be seen in Figure 4.4, that the difference is in the order of $10^{-3}g$, which is very small. Looking at the Euler acceleration, it can be concluded that this does not affect the results at so slow rotational rates with minimal changes in angular velocity during the start, however, when looking at the relative acceleration, the centrifugal acceleration and the Coriolis acceleration the story is different. The last two are periodic and reach values up to $1.6 \cdot 10^{-3}g$, whereas the relative acceleration reaches $0.6 \cdot 10^{-3}g$. These small values exceed the accuracy of the sensors, the WIT sensor has an accuracy of $0.01g$. This can explain why there is a difference between the model and the sensor data, as the accelerations are too small for the sensors to detect. This causes to some extent the slightly different patterns in Figure 4.4, and the variations are in the order of $10^{-3}g$ over time, which is the same order of magnitude as the additional

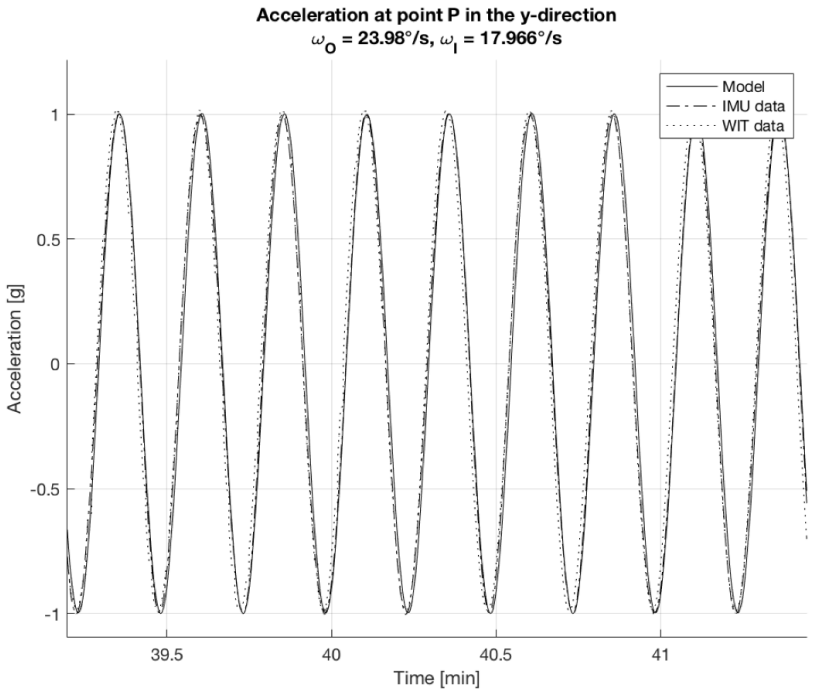

Figure 4.6: The measured and modelled acceleration in the y-direction after 40 min run on the RPM.

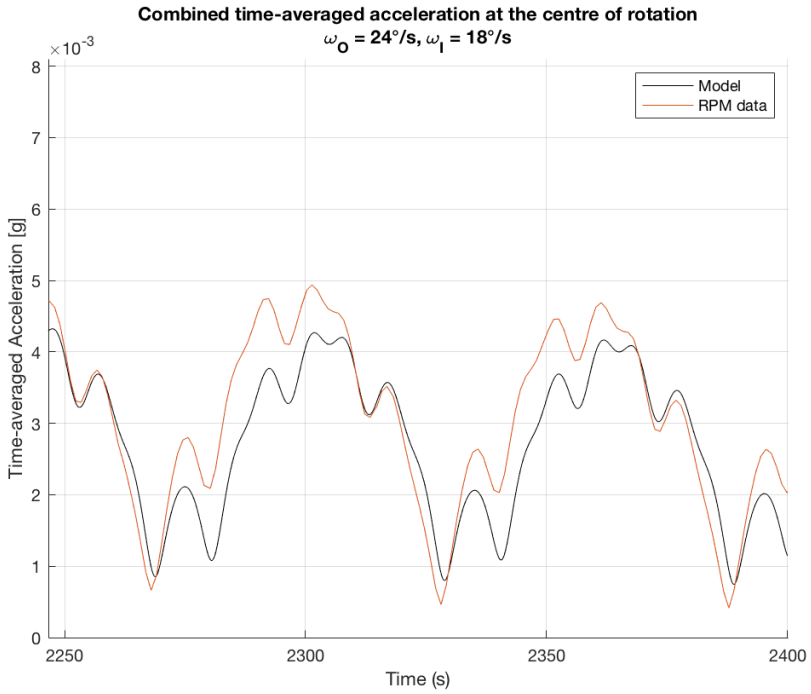

Figure 4.7: The time-averaged acceleration after 38 min of a run in the RPM. The model and the RPM data are taken from the centre of rotation.

accelerations at these rotational rates.

The last thing to consider before continuing is the overall measured acceleration in Figure 4.8. The RPM data is as expected constantly $1g$ as it is in the centre of rotation. The model is shown for the corner where there are some effects of the additional sources of acceleration. The two sensors vary

more in their measurements but stay close around $1g$ and are taken at the corner just like the model. Only a small part of the run is shown to give an indication of the data.

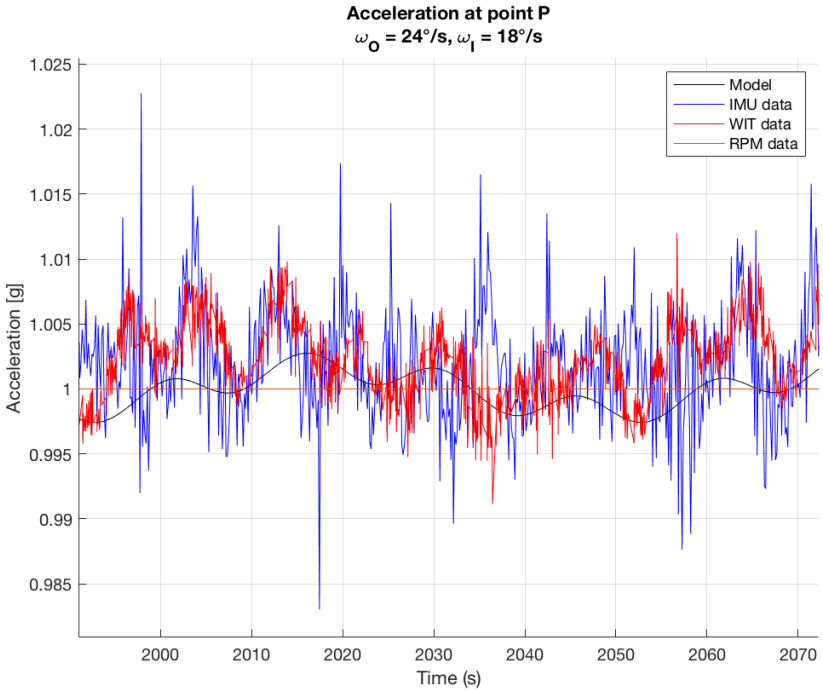

Figure 4.8: The measured acceleration 34 min into a run on the RPM. The model and the IMU and WIT sensors are measured at the corner of the platform. The RPM data is measured at the centre of rotation.

In order to evaluate the model correctly, other locations of the sensors should also be included. For this, it can be beneficial to increase the rotational rates, such that the accelerations become detectable when moving away from the centre of rotation. It is very hard to determine the exact bias of the measurements, which can have an impact on the results. This is especially true when looking at the time-averaged acceleration, where a small bias in any direction can make a noticeable difference. To show the different measurements of varying the location, rotational rates of ω_I = $73°\text{s}^{-1}$ and ω_O = $96°\text{s}^{-1}$ are used. Three distinct locations are measured, namely at the centre of rotation, where the RPM data is expected to be the most accurate, at a middle distance between the centre and the corner, and lastly at the corner of the platform. Instead of trying to precisely place a sensor at the axis of rotation, it is placed in the centre of the platform and below the axis of rotation. This will yield a theoretical error of $3.5 \cdot 10^{-3} g$ based on the results from the model. The data from the RPM should be sufficient to compare the model at the centre of rotation. It has a long history of use and has previously been validated and thoroughly tested, which is why it can be used to validate this model. The two sensors are inaccurate partly due to them being placed below the axis of rotation but also due to their bias and the uncertainty in placing the sensors. At the very centre, there should be no additional accelerations to Earth's gravity, which means that a bias has a large effect on the overall result but a small misalignment can also alter the results to a certain degree. These are the reasons, why the RPM data is considered to be the most accurate at the centre of rotation. The results from the centre are shown in Figure 4.9, where the model is included in both the centre of rotation and the sensor location. Neither of the two sensors comes really close to the expected g-level, but the WIT sensor measurements are significantly off compared to the others. Applying a constant bias in the individual directions is able to account for this difference. A bias of $0.0295g$ in the x-direction, $0.015g$ in the y-direction and $0.013g$ in the z-direction is enough to align the WIT data with the model. This cannot be explained solely by the accuracy of the sensor that is $0.01g$, there will have to be other aspects at play. However, it is not possible to extract this bias from the measurements, which is why it is not included for validation purposes. Looking at the medium distance from the centre, the measured g-level actually decreases, which is the opposite of what would be expected. This shows that there definitely is some uncertainty in the measurements that affects the

results.

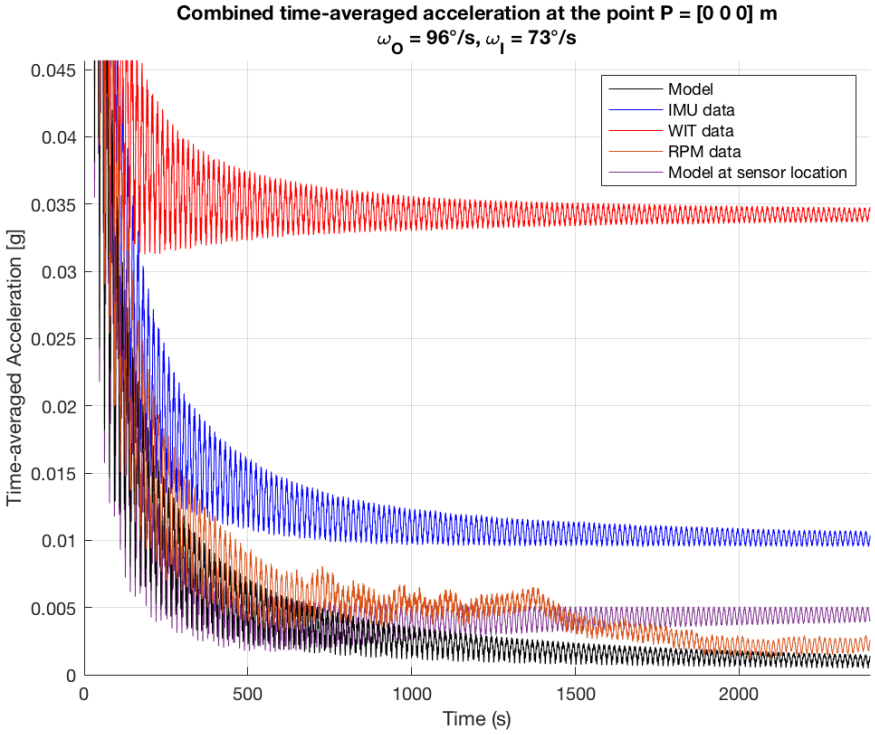

Figure 4.9: Time-averaged acceleration close to the centre of rotation. The WIT and IMU sensors have been placed 1.6 cm below the centre of rotation.

Moving away from the centre of rotation invalidates the results of the RPM and provides a more suitable case for the sensors, which are used to evaluate the results of the model. The intermediate distance of the sensors is taken 3.3 cm from the centre in the x-direction, 3.8 cm in the y-direction and 1.65 cm below the centre of rotation due to the vertical distance to the first slot for the platform. Generally, the results improve as the sensors now show more accordance with the model. Three different sets of rotational rates have been tested and analysed at this intermediate distance and two distinct runs have been made to test the reliability of placing the sensors at this distance. The two runs show no difference between each other, meaning the placement of the sensors is performed accurately. The three sets of rotational rates are ω_I = $73°s^{-1}$ and ω_O = $96°s^{-1}$, ω_I = $120°s^{-1}$ and ω_O = $103°s^{-1}$, and ω_I = $100°s^{-1}$ and ω_O = $50°s^{-1}$. For the third set, the IMU sensor and model coincide at the exact same level, whereas the WIT sensor is still overestimating the g-level compared to the model. The results from ω_I = $73°s^{-1}$ and ω_O = $96°s^{-1}$ can be seen in Figure 4.10. This result is similar to the final set of rotational rates at the medium distance. All three examples show that the WIT sensor overestimates the g-level, whereas the IMU sensor is reasonably close to the model but slightly underestimates the g-level. None of the differences seen between the model and the measurements can be claimed to be significant and beyond the uncertainty. Placed in between the two sensors, the model still makes a very probable solution for determining the accelerations present during a run as well as the resulting g-level at a point located arbitrarily outside the centre of rotation.

The final location is at the corner of the platform, placed 6.1 cm from the centre in the x-direction, 6.15 cm in the y-direction and still 1.65 cm below the centre of rotation. Here, the measurements show good accordance with the model as seen in Figure 4.11. The previously mentioned drifting of the WIT sensor becomes very evident in this run and shows that the measurements are not perfect. The drifting occurs naturally in the sensor and there is no way to change it prior to the runs, one could try to adjust the results afterwards by correcting the data for the drift. However, this showed no improvement overall and it should be accepted that there occasionally is drifting in the sensors as long as it is known that this is a possibility. During a 40min run, this drifting of the sensor is not substantial and will not lead

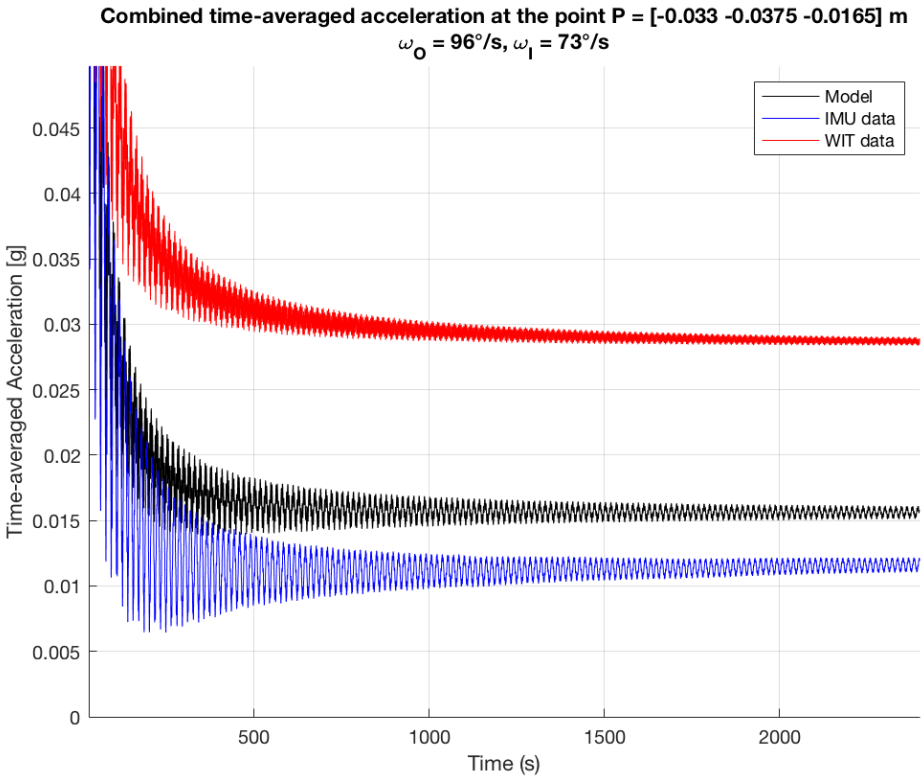

Figure 4.10: Time-averaged acceleration at an intermediate distance from the centre of rotation.

to a poor conclusion as other factors have larger impacts on the measurements. The results display a certain affirmation of the model at the corner of the platform. The inaccuracies of the sensors cannot be completely removed, however, when looking at a different set of rotational rates the story is the same. At the corner location, several rotational rates have been used, which are shown in the following section below. This is done to evaluate the model in more detail across several sets of rotational rates. Overall, the model is within the uncertainty of the measurements, which indicates the model's validity at different distances. It is not possible to increase the distance further on the available RPM, which sets the limit in this case but at the available distances, the model shows reasonable agreement with the sensors. For this run, the time-averaged contribution of the individual directions can be seen in Figure A.2 to Figure A.4 and the acceleration measured in each direction can be seen in Figure A.5 to Figure A.7. There is a small shift in phase in the measured accelerations compared to the model, which can be explained by the motors not necessarily reaching the correct rotational rates as previously shown, it can also be that the modelled time to reach the steady rotational rates is not accurate. Overall, the acceleration of the individual directions is as expected by the model. The time-averaged accelerations vary a little more, and one sensor underestimates the averaged acceleration in the x-direction, whereas the other sensor does it for the y-direction. The drifting of the WIT sensor is not immediately clear when looking at the directions individually, which indicates it might be an overall drift of the sensor not applicable to just one direction.

4.1.3. Varying Rotational Rates

The results for this section are very similar to the previously shown results, therefore a table summarises the main results in Table 4.1. All the measurements included here are taken at the corner of the platform to maximise the additional accelerations. Furthermore, the final 300 data points for each run have been averaged to give the results as the RPM movement and measurements have a periodic nature. The runs are of at least 40min but some of them are longer. The main consideration is to use various ratios of rotational rates, as these determine the pattern taken by the gravity vector. However, it is also interesting to evaluate similar ratios but at faster and slower rotational rates to more clearly see the

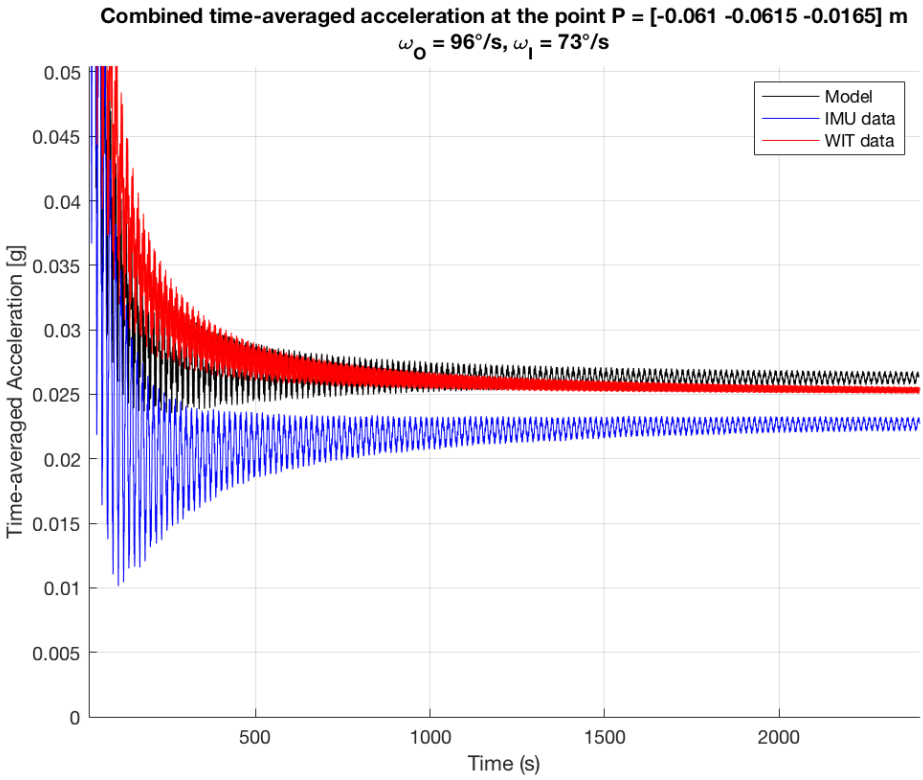

Figure 4.11: Time-averaged acceleration at the corner of the platform on the RPM.

impact on the resulting accelerations when changing the rotational rates. Clearly, the WIT sensor is not very accurate at low rotational rates where the resulting g-level is below the accuracy of this sensor. At faster rotational rates its measurements are closer to the IMU sensor and seem more realistic. Overall, the model follows the sensor measurements well and at higher rates, the resulting g-level increases as expected.

When looking at the numbers, it may seem that there is a large deviation in the results, however, at such small g-levels, even small discrepancies can lead to a large percentage error. Looking at the results of the measurements in each direction shown previously in Figure 4.5, the measurements actually coincide very well with the model and here it is the small errors in the order of $10^{-3}g$ that can explain some of the discrepancies. These can come from the placement of the sensors, the actual location of the sensors inside the casing, bias, drifting, the accuracy of the sensors or inaccurate rotational rates.

The inaccurate rotational rates can be detrimental to the results at specific ratios. In this case, it is when the two frames have the same rotational rates. This setting is not suitable for the RPM as one cannot be sure it actually reaches the exact same rotational rate for each frame. Slight inaccuracies in the motor speeds result in a continuous drift that grows bigger over time. This will be explained in detail in Section 4.3 when considering the drifting of the RPM itself, which is caused by inaccurate rotational rates. Hence, this ratio is not included in the table below.

Table 4.1: Summary of the time-averaged g-level for the measurements and the model at varying rotational rates and ratios. The time of the runs is at least 40 minutes but can be longer. The g-level displayed is an average of the final 300 data points to account for its periodic nature.

Inner frame [$^\circ s^{-1}$]	**Outer frame** [$^\circ s^{-1}$]	**Ratio** [-]	**Model** [g]	**WIT sensor** [g]	**IMU sensor** [g]
12	24	0.5	0.0023	0.0272	0.0028
18	24	0.75	0.0031	0.0273	0.0027
30	40	0.75	0.0045	0.0155	0.0019
40	30	1.33	0.0059	0.0294	0.0053
50	75	0.67	0.0150	0.0101	0.0107
50	100	0.5	0.0243	0.0178	0.0186
73	96	0.76	0.0263	0.0252	0.0227
75	50	1.5	0.0150	0.0092	0.0123
100	50	2.0	0.0230	0.0176	0.0215
100	75	1.33	0.0281	0.0118	0.0250
103	120	0.86	0.0443	0.0455	0.0411

4.2. Trajectory

Different ratios of rotational rates of the frames yield distinct patterns in the trajectory of the gravity vector or, equivalently, the inner frame. These patterns will be the same whether fast or slow rotation is used. Looking at the trajectories, it quickly becomes evident that some ratios cover more of the unit sphere than others. Depending on the system of interest, one might prefer a more evenly distributed trajectory or maybe the trajectory is not of importance. Whether it is one or the other, it is interesting to look at how the gravity vector is dispersed throughout a run. To do this, runs were recorded using a motion capture system to track the trajectory of the inner frame. This is compared to the theoretical trajectory, which can be modelled using the rotational matrices. The motion capture recordings can be used to validate this approach and determine the orientation of the RPM. A result from this can be seen in Figure 4.12. The model and the recorded motion correspond very well and it can be seen that the trajectory forms a very distinct pattern that is repeated throughout the run. This specific run lasted close to 10min but the trajectory repeats the same pattern due to the constant rotational rates of both frames. On the sides of the plot, the pattern of the model is projected in 2D to give a better feeling of the results.

The pattern of the trajectory can be simpler at certain ratios, which makes it easier to compare the model with the recordings. In this section both the ratio of 0.5 and 0.75 are being used as they clearly show two distinct patterns but still allow easy exploration of any differences between the recordings and the model. In Figure 4.13 it becomes very clear that there is a discrepancy between the model and the recordings. Theoretically, the trajectory should follow the same pattern during a run, however, the RPM seems to be drifting, resulting in a pattern that deviates from the theoretical result.

The rotational rates of ω_I = $24^\circ s^{-1}$ and ω_O = $18^\circ s^{-1}$ were also considered earlier. Here it was shown that the motors do not fully reach the correct rotational rates resulting in a shift of the phase of the measurements. This shift is correlated to the drifting of the RPM. Applying the rotational rates used earlier explains the drifting in the pattern. The interesting aspect is that this drifting only occurs at certain rotational rates and not all. The pattern is repeated as expected in Figure 4.12 but increasing the rate of the inner frame to $18^\circ s^{-1}$ leads to small inaccuracies. Rotating the frames at ω_I = $24^\circ s^{-1}$ and ω_O = $12^\circ s^{-1}$ was the only case that did not show any drifting but a repeat of the pattern as expected. When the ratios were chosen to cover more of the unit sphere with a more complex pattern, it was not possible to distinguish the data sufficiently to determine whether there was any drifting or not.

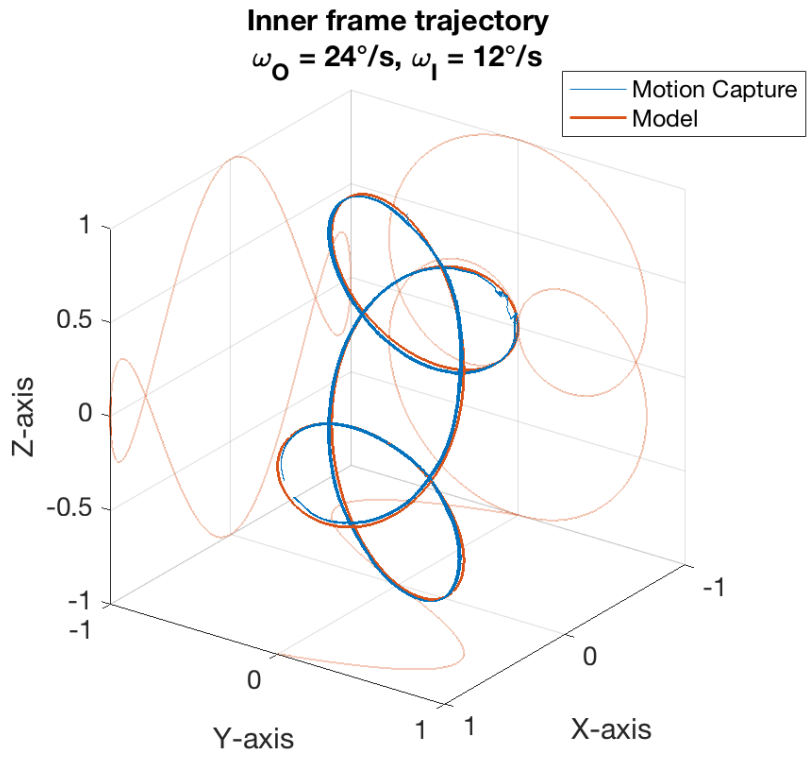

Figure 4.12: Trajectory of the inner frame at ω_I = $24°s^{-1}$ and ω_O = $12°s^{-1}$. The 2D shapes of the model are shown as shadows on the sides.

It should be noted that the drifting is seen when using the RPM at constant rotational rates. Using one of the predetermined trajectories is not expected to result in drifting, as the movement is determined by reading specific lines of the code, that is used to determine the orientation of the RPM. These should be correctly implemented and follow the correct path, which also changes in direction and rotational rates, which makes it impossible to determine any drifting without knowing the exact movement determined by the code.

As mentioned, the motors are not truly accurate, which will result in a drift that is clearly visible in the trajectory. Earlier, the example of rotational rates at ω_I = $23.98°s^{-1}$ and ω_O = $17.966°s^{-1}$ were used, and these will be used again here, to show the drifting that will occur in the model as a result of small inaccuracies. In Figure 4.14 these rotational rates have been adopted and it clearly follows the recorded trajectory very well. It is not given that these rotational rates are the exact rates that the RPM uses but it can be concluded that they are a potential match and that the RPM at least do not necessarily follow the theoretical trajectory for a given set of rotational rates. In most cases, this drifting behaviour was not spotted in the data as it equals out in all directions when covering more of the unit sphere. However, at a specific ratio, this drifting was also visible in the data, which will be explained in Section 4.3 below.

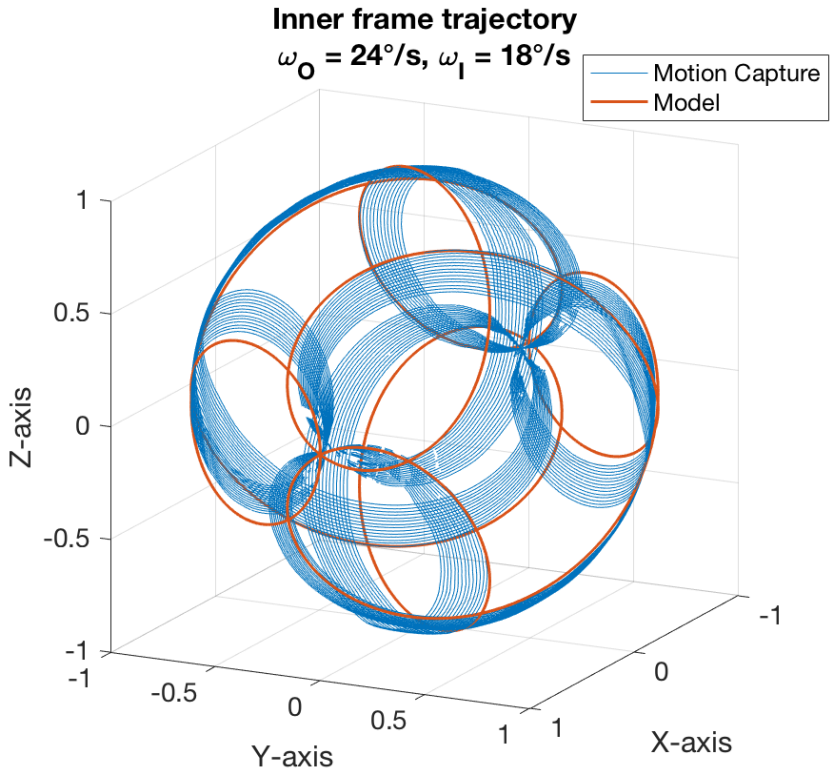

Figure 4.13: Trajectory of the inner frame after 14 min of a run with the model showing the theoretically correct path.

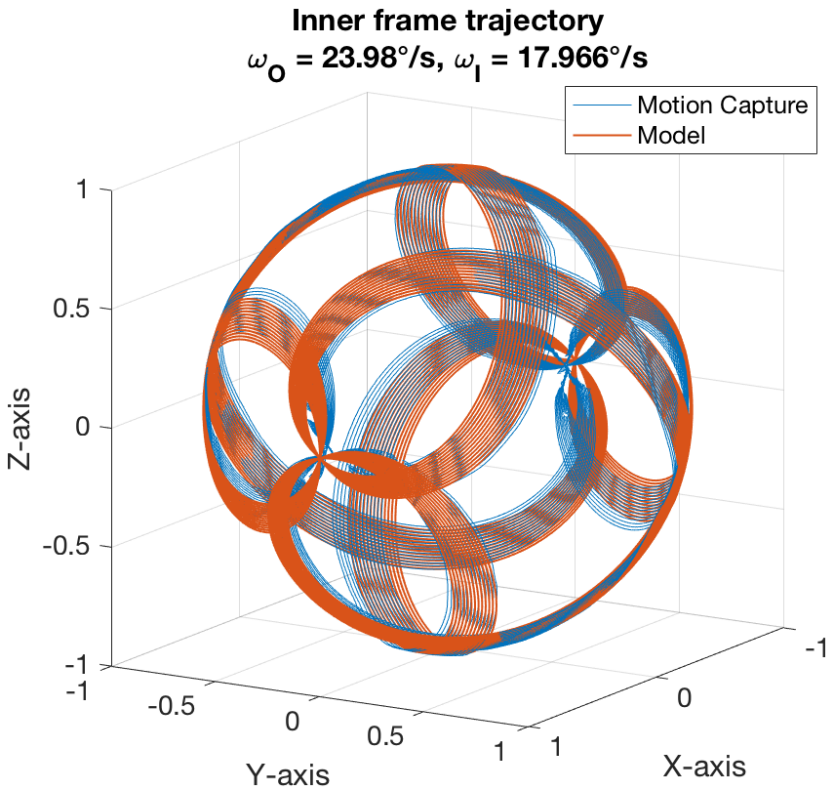

Figure 4.14: Trajectory of the inner frame after 14 min of a run using imprecise rates.

Considering the orientation of the RPM can be important for certain experiments and generally it is

preferred to have the gravity vector spread out in more directions to improve the quality of the simulated microgravity on a sample. The trajectories can balance out each outer in the model, providing a low microgravity level by taking a simple pattern. This is not ideal as gravity should point equally in all directions while also providing low g-levels. One thing that is evident when plotting the trajectories for different rotational rates, is that this trajectory contains pole bias. No matter which rate is chosen, the constant rotational rates will always result in pole bias due to the nature of the movement. When the outer frame is aligned vertically, which happens twice during each rotation, the gravity vector is bound to point in the same direction on a sample, resulting in two poles being generated. To avoid this, one would need more complex controls that avoid the outer frame moving through the vertical position. Examining the trajectory while also looking at the resulting g-level can be used to gain insights when determining the rotational rates of the RPM for experiments. When developing new control algorithms, this model can also be used to evaluate these control algorithms before they are implemented into the hardware. Different control algorithms will be explained further in Chapter 5.

It can be noted that the scaling of the motion capture data differs slightly from reaching the perfect unit sphere. In Figure 4.14, the scaling in the x-direction does not generally go to -1 or 1. This is likely due to one data point during the movement being recorded to be slightly further, as well as one slightly closer, to the camera than the general data points. This causes a slight offset in the recording compared to the model, which can be seen if looking closely around the two poles. This offset is further highlighted on the far side by the perspective of the plot. The offset is not very significant and the pattern is clearly still very close to the expected pattern indicated by the model, which adds to accepting the model to describe the RPM.

4.3. Drifting of the RPM

It does not matter significantly that the RPM motors do not accurately reach the correct rotational rates for most results. However, there are occasions where it is absolutely critical to the results and yields some results that are completely wrong to the intention. The drifting was noticed easily when looking at the trajectory, however, with the data not showing this drift, it will cancel out over time as the drifting occurs equally in all directions. Rotating the frames at the same rate should yield a result where the time-averaged acceleration reaches a constant level similar to the other rotational rates. In the measurements, it is seen that the is a drift of the acceleration. Interestingly, the RPM data also show this drift indicating that their model is using the actual orientation and rotational rates of the RPM and not the desired ones. This is the case for all the three sets of same rotational rates at ω_O = ω_I for $40°\text{s}^{-1}$, $60°\text{s}^{-1}$ and $100°\text{s}^{-1}$, which were tested on the RPM. In Figure 4.15 one of these runs is shown, where it is clear to see the drifting of the sensors and the RPM data. The IMU sensor does not follow the expected shape, as it should be similar to the WIT sensor and the RPM data in its shape. In the measurements, it is the x-direction and z-direction where the drift occurs. This drifting has tried to be modelled into the model by adjusting the rotational rate of one of the frames to be $0.01°\text{s}^{-1}$, which can be seen in Figure 4.16. This figure also shows the result from rotating the frames at $60°\text{s}^{-1}$, where both sensors show the same drifting, which is expected when the motors do not operate at the exact same rates.

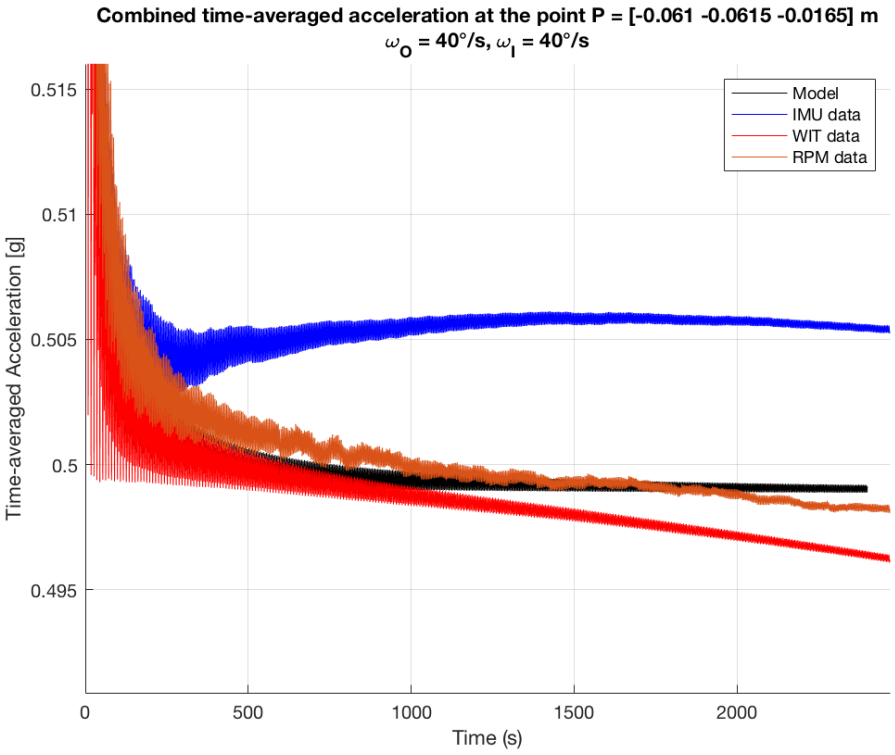

Figure 4.15: Time-averaged acceleration when the frames are supposed to run at the same rotational rates. The IMU sensor is inaccurate compared to the other data sets. The drift of the sensors is clearly visible and is caused by deviations in the motor speeds.

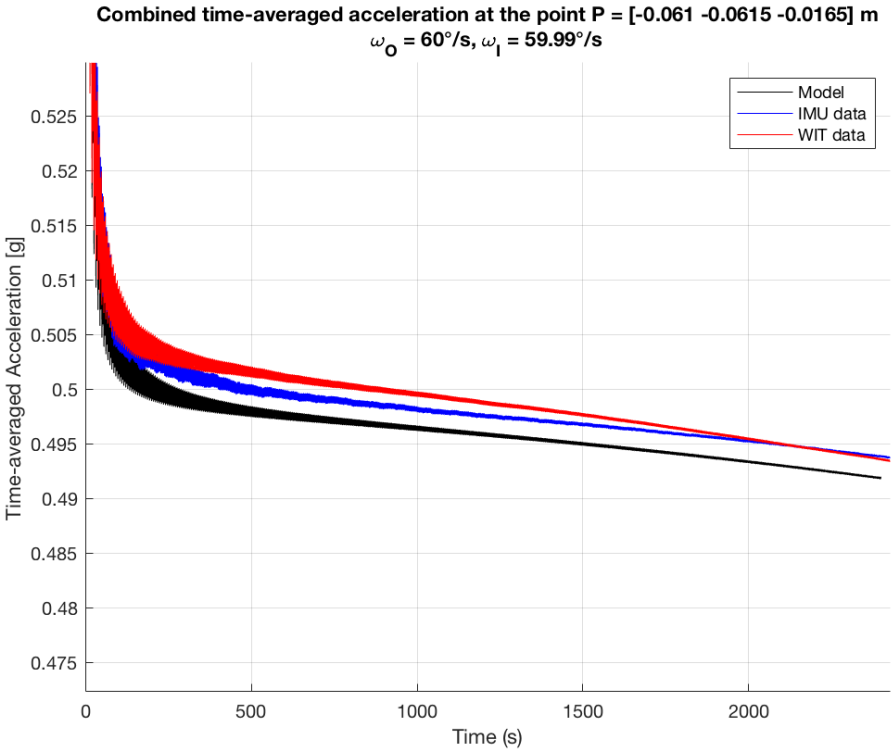

Figure 4.16: Time-averaged acceleration when the rates are deviating by $0.01°s^{-1}$. This can explain the drifting seen in the measurements.

The reason for the drifting to show in the measurements when the two frames rotate at the same rate but not in any of the other ratios tested, can be explained by looking at the trajectory of the gravity vector for this case. The trajectory will not cover the entire unit sphere and therefore, it will not cancel out but rather result in the drifting observed. In Figure 4.17 the theoretically correct trajectory is shown alongside the trajectory for drifting. It is clear that only a very small part of the unit sphere is covered, and only on the bottom side of the unit sphere. Hence, when drifting, the trajectory moves towards completely new angles closer to the x = -1 axis in a clockwise rotation about the y-axis for x = 0 and z = 0. This can explain the drifting in the measurements and show why this RPM should not be used at the same constant rotational rates for the two frames. It will simply lead to a wrong result compared to the intention. This is the only ratio of rotational rates where the drifting has a significant impact and the only ratio that the RPM should never be used at. At the other ratios, the drifting will be spread out towards all directions and thereby cancel out. If expecting a certain trajectory and g-level, the drifting can be unacceptable, however, in most use cases of the RPM this drifting does not play an important role. The resulting g-level will be the same and the trajectory will cover more of the unit sphere. There also exist different ways of controlling the RPM and not just using constant rotational rates. This was only done here as the RPM did not support the implementation of other more complex control algorithms.

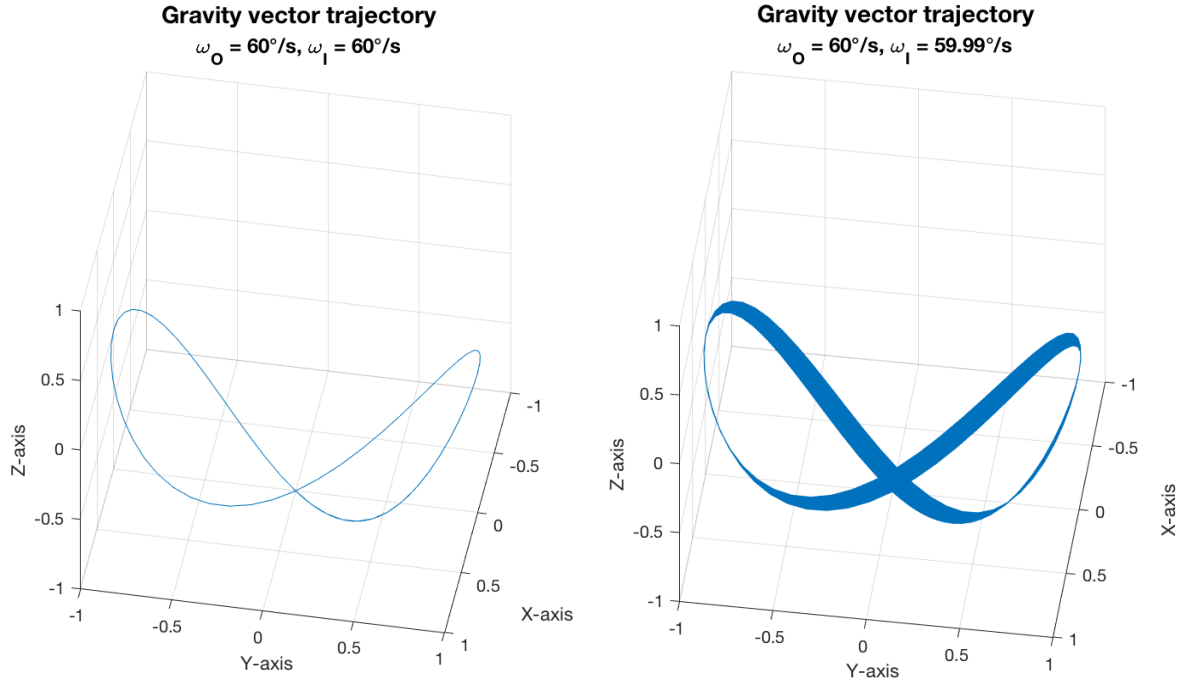

(a) Modelled trajectory at ω_I = $60.0°\text{s}^{-1}$ and ω_O = $60.0°\text{s}^{-1}$

(b) Modelled trajectory at ω_I = $59.99°\text{s}^{-1}$ and ω_O = $60.0°\text{s}^{-1}$

Figure 4.17: Trajectory of the gravity vector is drifting when one motor is off by $0.01°\text{s}^{-1}$. The drifting results in moving the trajectory towards the x = -1 axis.

4.4. Velocities

One last thing to look at in this chapter is the velocity of the sensors. Both sensors also measure the angular velocity of the RPM during a run, which can be compared to the angular velocity generated by the model. This is an extra step to evaluate the model beyond just the accelerations and trajectories, although these are the interesting aspects. The velocity is measured in the x, y and z-direction of each sensor, and the data is combined by taking the square root of the summation of each direction squared as seen in Equation 4.1, similarly to the approach for the acceleration.

$$\omega_{tot} = \sqrt{\omega_x^2 + \omega_y^2 + \omega_z^2} \tag{4.1}$$

One thing to note is that the WIT sensor measures at an angle 10 times larger than expected. The angular velocity of the frames, depending on the chosen rate, is around 100^circs^{-1} for each frame. In

the case of ω_I = $103°s^{-1}$ and ω_O = $120°s^{-1}$, the sensor measures velocities in the order of $1200°s^{-1}$ in the individual directions, a factor 10 higher than expected. Accounting for a factor of 10 in the data yields the result shown in Figure 4.18. Both the model and the sensors agree on the angular velocity, and it can be seen that the IMU sensor is periodically moving around the same value as the WIT sensor and the model. As the angular velocity stays constant throughout the run, only the first $30\,s$ is shown. The rate of change at the beginning of the run matches the acceleration time of $5\,s$ before the correct rotational rates are reached, as used earlier. Similar results were found for the other sets of rotational rates indicating that, although a little simple to model, the angular velocity of the model is in accordance with the measured value. This angular velocity is only based on the rotational rate of the two frames and therefore it is not the most complex part to model.

The small deviations from the correct rotational rates discussed earlier are so small, that they are not visible when looking at the angular velocity. When the overall angular velocity is around $160°s^{-1}$, small deviations in the order of $0.1°s^{-1}$ and less, are not visible. The average velocity for the constant phase is modelled to be $158.14°s^{-1}$, whereas the WIT sensor measures $158.03°s^{-1}$ and the IMU sensor measures $158.64°s^{-1}$.

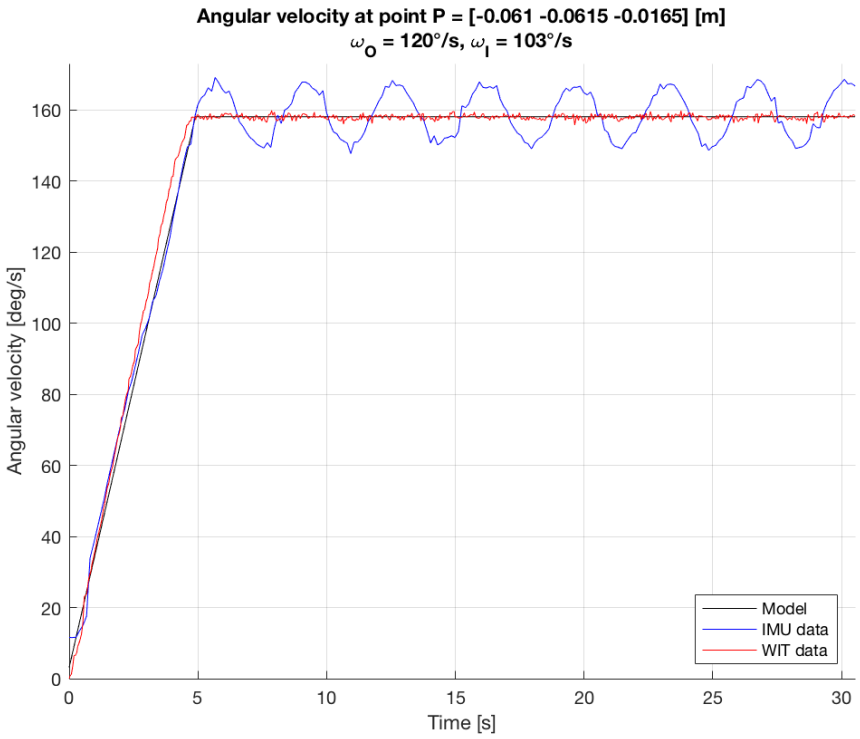

Figure 4.18: Overall angular velocity at the corner location during a run on the RPM.

4.5. Evaluation of Alternative Models in Literature

Comparing the model developed in this thesis to what has already been done in the literature will help evaluate the approach. The most recent model presented in literature [106] is supposed to predict the accelerations of a point P in the RPM. The following three equations shown in Equation 4.2 to 4.4 are given to model the acceleration at the point P in the x, y and z-direction respectively. R in these equations is the distance from the origin to point P, t is the time and ω_I and ω_O are the angular velocities of the inner and outer frame, respectively.

$$a_x = -R\left[\left(\omega_I^2 + \omega_O^2\right)\ sin\omega_O t\, cos\omega_I t\ +\ 2\omega_I\omega_O\, cos\omega_O t\, sin\omega_I t\right] \tag{4.2}$$

$$a_y = -R\omega_I^2\, sin\omega_I t \tag{4.3}$$

$$a_z = R\left[-\left(\omega_I^2 + \omega_O^2\right)\ cos\omega_O t\, cos\omega_I t\ +\ 2\omega_I\omega_O\, sin\omega_O t\, cos\omega_I t\right] \tag{4.4}$$

There are several things wrong in this paper, especially the use of the wrong terms. However, scientifically the most important aspect is the model, which is completely wrong. This is not the approach to take when trying to model the movement of the RPM. The first thing to note is that the contribution of Earth's gravity is missing. This is an important part of the overall acceleration. Without this contribution, the model presented will not start at $1g$ but at $0g$. This is one very apparent mistake. The next thing to note is that it is limited to only constant rotational rates. Using the angular velocity multiplied by the time is only valid to find the angle when the frames are moving at constant rates. If the frames change their rates, a sudden jump will be experienced in the values of the cosine and sine terms, which can significantly affect the acceleration level. In reality, these abrupt changes in values will not occur, instead, the angle will gradually change from the previous position to the new one following the new rotational rate.

After adding the contribution of Earth's gravity to the model, it is run for two locations to show the difference. The locations are chosen to be at the centre of rotation, and at the corner location of the existing RPM, which the previously presented measurements were based on. This is done to easily evaluate this alternative model with the data. As shown in Figure 4.19 there is no deviation when it comes to the resulting g-level when using these equations at different locations. The g-level should increase significantly as seen earlier, however, the acceleration level only changes shape to a very limited degree. Another aspect can be seen in Figure A.8 where the overall modelled acceleration does not match Earth's gravity of $1g$. At the corner location, it should be oscillating about $1g$, however, in the alternative model, the shape is different and closer to $1.4g$ than $1g$, further indicating that this model is wrong: the movement of the RPM cannot be simply modelled by differentiating a position twice, it is the wrong approach for this problem.

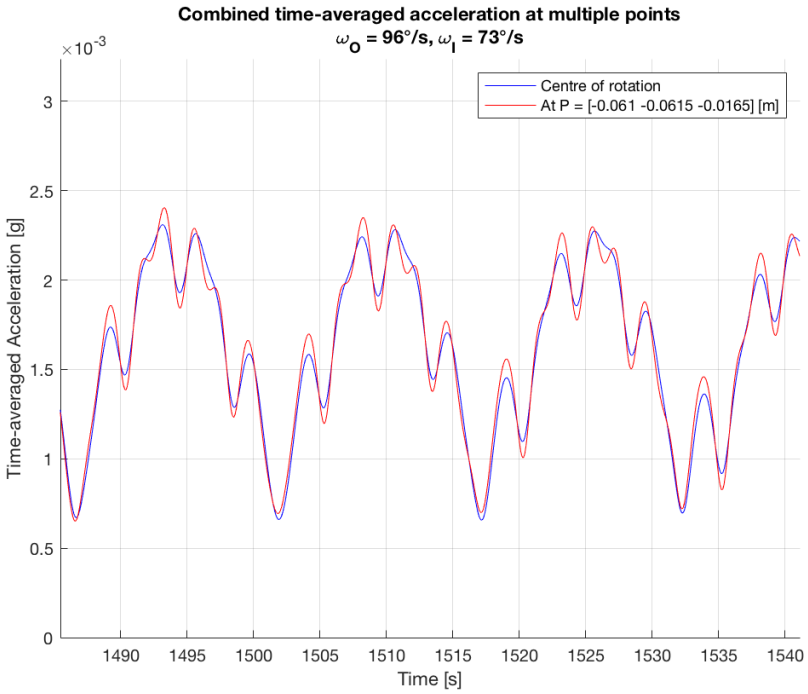

Figure 4.19: Resulting g-level of the alternative model presented in [106]. A small portion of the plot is shown to make the difference visible between the two points. Comparing it to previous results shown from the sensors, the result at the corner should be around $0.026g$.

An approximation of the acceleration based on the position has previously been presented as shown in Equation 4.5 [100]. In the equation, r indicates the position to the point P. The first thing to note about this approximation is that they in one step assume the two frames to rotate at the same rate. This is a special case where the resulting g-level is high and the trajectory covered does not cover the unit sphere. Once again, the contribution from Earth's gravity needs to be added. However, this model shows improvement compared to the previous one by actually oscillating about a level of $1g$. Using

this approximation for an arbitrary set of rotational rates and changing the location has no effect but using this approximation when the two frames have the same rotational rates lead to different results for different locations. Despite showing different results for different locations, this approximation is very limited and does not work for a broad set of rotational rates. Hence, there is still a need for a complete expression to describe the dynamical system, that the RPM is, which the model presented in this thesis does.

$$a_{mean} = \omega^2 \sqrt{2.25r_x^2 + r_y^2 + 2.25r_z^2} \tag{4.5}$$

When it comes to the trajectory of the gravity vector, one paper has used a sensor to track the orientation of the RPM [107]. In their simulations, they have switched the orientation 90° compared to the sensor data, however, the same patterns recorded by the motion capture system can be seen in their sensor data for certain ratios of rotation. Their results show no signs of drifting at any ratio. The main difference is that some of their data seem to be rotated a little bit. This is easily seen when the ratio of the two frames is 0.5. Here their results are very similar but rotated slightly compared to the results presented in this paper from the motion capture recording. Apart from this difference of having some of the sensor data rotated and the simulation being rotated 90°, the results show very similar patterns. The rotation of their simulations can very well be caused by a small inconsistency in the use of their coordinate system. This can easily occur if not careful when writing out the rotational matrices according to the rotation of the RPM. A different coordinate system is used for their simulations, than what is used in this model based on their results for the angular velocity. Their coordinate system is not shown, making it difficult to evaluate whether this actually is the cause for the rotation of the trajectory.

4.6. Conclusive Notes

This chapter has focused on different aspects to validate the model presented. Two different sensors have been used together with a motion capture system for recording the movement of the RPM. In this section, a small recap of the most important validation aspects will be outlined before moving on to using this model to explore the use of the RPM in gravity-related research on Earth from an engineering viewpoint.

The results show some discrepancies between the model and the data, which can be explained by several factors. Firstly, the accuracy of the sensors is not perfect and is in the order of $0.01g$. Looking at data that should have a very small g-level below $0.01g$, the sensor accuracy can impose a deviation in the measurements leading to a wrong result. In addition to this is the drift of the sensors, which can occur during the measurements. The drift during the 40min runs investigated here does not affect the sensors significantly but they are still present and do affect the final result.

One of the largest unknowns is the bias of the WIT sensor and the bias, in general, in accelerometers. This is a systematic error that, even though it is very small, can hugely impact the results as some g-levels were in the order of $10^{-3}g$. This means a systematic error will seriously impact the results as seen in some of the examples shown earlier. The bias cannot be determined completely accurately and varies from run to run. To evaluate the difference between runs, the same settings were used on different days. This led to measurements that varied $0.015g$ and the results were not consistent in showing the correct dominant axis for the acceleration, which is expressed through the different shapes in Figure 4.2.

It was furthermore shown that the RPM experiences drift as the rotational rates are not 100% accurate, leading to a phase shift in the rotation at most ratios of rotational rates but completely unexpected results when the two frames rotate at the same rate. Finally, it can also be said that the sensors are not located at the exact position every time. There might be a small angle or a small distance from the actual sensor to the modelled location. These were shown to not greatly impact the results. Performing different runs on the IMU leads to differences of only $0.002g$ across three different runs at the same settings, which is accurate within a couple of millimetres accuracy as it was shown that 1 mm difference would result in a change in g-level of $4 \cdot 10^{-4}\ g$. The exact location of the sensor inside the casing could also vary a little from the modelled location, which also leads to small differences. Finally, it can be mentioned that the trajectory was basically spot-on between the recordings and the model.

Combining all this information, the modelled results are concluded to be within the uncertainties of the measurements. The model is able to predict the trajectory of the RPM and the resulting g-level at arbitrary locations and for all rotational rates of the inner and outer frame. As expected, moving away from the centre of rotation leads to larger accelerations due to additional accelerations affecting the results and not only Earth's gravity. Therefore, it follows the simple logic that would be expected and is deemed a valid model for the RPM. Looking at the individual directions, the sensors and the model indicate the same level and phase of acceleration indicating that the differences originate from very small errors in the sensors data, which explains a limitation of this thesis being the quality of the sensors. Overall, this should be a theoretically valid model for predicting the movement and the resulting g-level of a run on the RPM. This model is therefore used in the following chapters to investigate and show different aspects of operating the RPM for gravity-related research.

5

Control Algorithms

Using constant rotational rates is not the only way to control the RPM. In fact, only the imagination sets the limit on how to control the two frames. In this chapter, different approaches are investigated to evaluate which controls might improve the resulting g-level or the trajectory of the gravity vector. The model introduced previously serves as a great tool to test any controls that might perform well and saves time and cost compared to building and programming a new RPM to test ideas. It can be very difficult to predict how well the control algorithm is performing and how to improve it without the model. Several different approaches are presented in the literature, which will shortly be discussed here, together with some control algorithms specifically developed to test a broader variety of controls and show how different control algorithms affect the performance, and thereby the use, of the RPM.

The known algorithms used in RPMs will be shortly shown and discussed in Section 5.1 and can be seen as an addition to Chapter 2.4. After this, various aspects of making a control algorithm will be explored with the corresponding explanation in Section 5.2. Then follows some information on pole bias and potential ways to overcome this problem in Section 5.3 before a partial gravity algorithm is introduced in Section 5.4.

5.1. Previously Used Algorithms

The randomness aspect was introduced as an improvement to the use of a 3-D clinostat rotating at constant rates around two axes. This new algorithm randomly changed the rotation rate in the range from 2 to -2 (opposite direction) rev/min. The two frames changed rotation speed every $30\,$s to $60\,$s [74]. This has certain advantages compared to constant rotational rates, namely that the sample does not become used to the movement of the frames and will not react to always moving a certain path as it constantly changes. The path also covers places that would not otherwise be covered when using only one set of rotational rates. However, there are not many more benefits to having completely randomised controls. Each change of rotational rates will lead to a period where the trajectory is not evenly distributed which affects the overall g-level. Adding to this that some sets of rotational rates perform better than others also means that in some settings the RPM is bound to deviate further from the optimal conditions. This combined means that an optimum g-level will not be achieved. The results of a $3\,$hr simulation using this algorithm are shown in Figure 5.1 and Figure 5.2, where the trajectory and the resulting g-level are shown, respectively. The trajectory can be compared to the one initially presented in the original paper and shown in Figure 2.11. There are two poles at either end, which will be further discussed in Section 5.3 but otherwise most of the sphere is covered. The g-level is compared to a simulation with constant rotational rates of ω_I = $12°$s^{-1} and ω_O = $18°$s^{-1}. There is a clear improvement in the g-level when using constant rotational rates. This supports the claim, that fully randomized controls are not the best way of controlling the RPM. Increasing the simulation time to$15\,$hrs does not change the achieved g-level.

The algorithm used in the simulation generates random values in the range -12 to $12°$s^{-1} with the

exception of zero, which is excluded. The rates change randomly every $30\,\mathrm{s}$ to $60\,\mathrm{s}$ and allow two seconds for the frames to reach the new speeds, irrespective of the difference between the two subsequent rates.

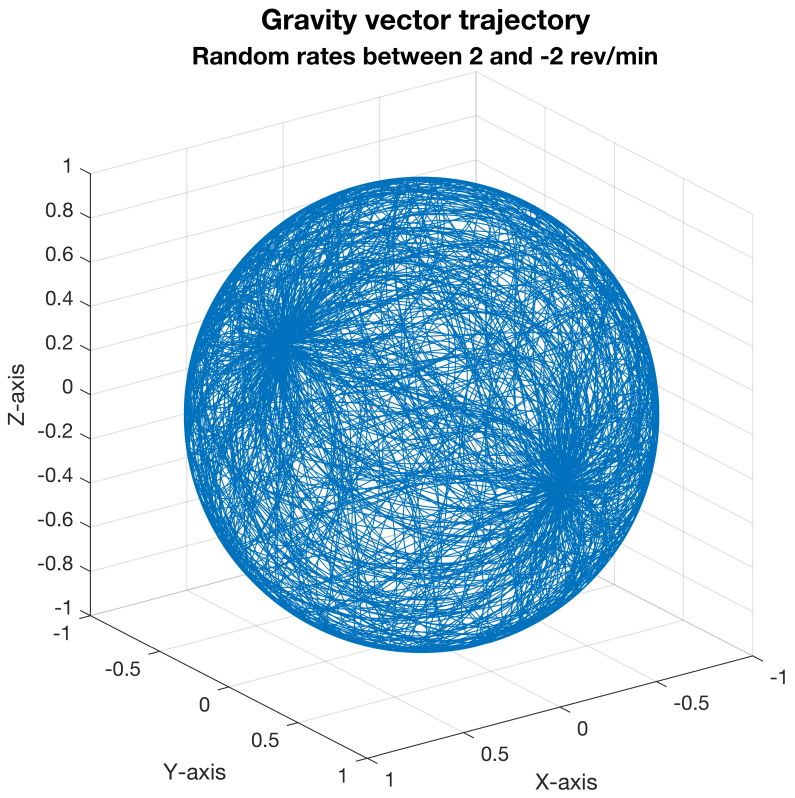

Figure 5.1: Trajectory of the gravity vector after $3\,\mathrm{hr}$ simulation of the algorithm randomly changing between 2 and -2 (opposite direction) rev/min every 30-60 s, and allowing $2\,\mathrm{s}$ to reach the new rotational rates.

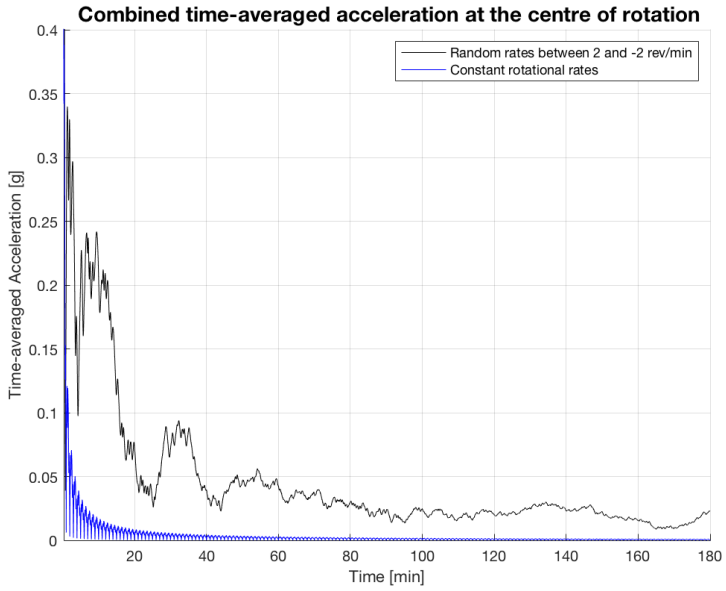

Figure 5.2: Time-averaged g-level after $3\,\mathrm{hr}$ simulation of the algorithm randomly changing between 2 and -2 (opposite direction) rev/min every 30-60 s, and allowing $2\,\mathrm{s}$ to reach the new rotational rates compared to constant rotational rates of ω_I = $12°\mathrm{s}^{-1}$ and ω_O = $18°\mathrm{s}^{-1}$.

Shortly after the randomness idea was presented in Japan, a different randomised aspect was introduced at Fokker Space in the Netherlands, where an RPM using completely randomized settings was built. This is very close to the above algorithm and will not be further discussed as the results show the same pattern, with a more randomized trajectory but a poorer simulation of microgravity. The only difference is that the rates of the frames can exceed $12°s^{-1}$ now, making it possible to cover more area by moving around faster. This real random mode was used with an average angular velocity of $60°s^{-1}$ to grow chondrocytes [10] or to grow bone tissue with random rotation between $60°s^{-1}$ and $75°s^{-1}$ [11], however, based on the analysis in this thesis it might actually yield improved results to use a different control algorithm to avoid pole bias when growing spheroids and 3-D cell cultures. This is something that should be considered in all future studies using the RPM.

Since then, there have been a couple more suggestions on how to control the RPM. The first of these uses a random walk algorithm with the two frames rotating at a constant velocity but the direction of rotation is inverted at random timesteps [100]. The transition in direction is done at constant rotational acceleration. With this approach, the two poles quickly became dominant but it was argued that the two poles cancelled out each other and resulted in similar effects between the original RPM and this new one. The validation results showed the same outcome compared to real microgravity for T-lymphocytes, which show a very distinct behaviour when exposed to microgravity compared to $1g$ environment. One thing to add is that using constant rotational rates must be done with caution. Certain sets of rotational rates are better than others to simulate microgravity and result in different trajectories of the gravity vector as already shown. A more comprehensive guide on using constant rotational rates is presented in Chapter 6. The resulting g-level showed values below $0.03g$, which is worse than the randomised controls discussed above. When trying to achieve microgravity, this value is very high and there is significant room for improvement. The results of an algorithm inverting constant rotational rates randomly are shown in Subsection 5.2.1 and also show a g-level around $0.03g$.

The next one is based on a surjective map comprised of the two angles that describe the orientation of the gravity vector based on the rotating frames [102]. The orientation of the gravity vector will cover a sphere, and in order to have a uniformly distributed orientation of the gravity vector a reference trajectory of all points in the sphere will be used. Each point has an equal likelihood of being visited and random points are chosen and projected onto the surface of a unit sphere. Here, neighbouring points are being merged to form a trajectory. The geodesic curvature and distance between points on this trajectory determine the angular velocity and acceleration that the RPM is following. To limit the angular acceleration only points close to the current point of the trajectory are included as possibilities for the next point.

A final idea for a control algorithm suggests moving faster through the poles and slower during the middle part of the unit sphere to overcome the problem of pole bias [108]. Moving faster through the poles does not remove pole bias, however. The time spent at the poles will be less dominant but the poles will still be present. It is stated that ideally, the frames should move infinitely fast through the poles [109], however, this is the wrong way to think. Moving infinitely fast through the poles generates infinitely large accelerations, that will completely destroy any attempt at simulating microgravity outside a point in the centre of rotation. Such an approach could therefore be detrimental when trying to minimise the resulting g-level although it does minimise the time at the poles. Even smaller accelerations will be able to affect the overall resulting g-level, and the faster the frames rotate, the larger this effect will be.

These suggestions show very different approaches and creative variety to control the RPM, which shows that there is no one way to definitely control the RPM but rather there exists a large design space of options. Evaluating these options and finding the best requires some understanding of the RPM and the modelled dynamics can provide a basis to understand these controls in a new and significantly more detailed way. The problem of pole bias occurs naturally when the outer frame is in the vertical position. This will be discussed in more detail in Section section 5.3, as it is a problem that most control algorithms encounter and there can be benefits to avoiding pole bias and not having two directions become dominant during an experiment. It is not straightforward to avoid pole bias while also minimising the resulting g-level but more on this will follow. After looking at what control algorithms already exist, it is time to test some control algorithms developed specifically for the purpose of gaining a better understanding of the movement of the RPM and how different controls affect the performance.

5.2. Varying the Control Algorithm

The main takeaway from the previous section is that randomised controls are not the best option to control the RPM. This is very important as it can be misleading as the name of the machine states *random*. With this set, this section shows the results of various specifically developed algorithms to show how alternative controls behave. A variety of control algorithms are presented below.

5.2.1. Inverting Constant Rotational Rates

One way to control the RPM is to invert the rotation direction of the frames using constant rates. This is to some extent similar to one of the previously presented methods, where the frame's rotational rates were inverted at random time steps. The rotational rates of the two frames are chosen before the simulation and will be inverted at random time steps between 30 s to 60 s, to allow for comparison with the results in Figure 5.1 and Figure 5.2. Comparing those two results will show the difference between randomly choosing the rotational rates and using constant rotation. The simulation allows the frames to reach the new speeds in 2 s under constant angular acceleration.

What really affects the results for this algorithm, is the chosen rotational rates and the time it takes to invert the rotation. The trajectories for the simulation with an inversion lasting 2 s compared to using half the time to invert the rates are shown in Figure 5.3. Just by changing the inversion time, it is possible to cover more of the unit sphere, while the resulting g-level stays close to the same value. Compared to the fully randomised rotation, significantly fewer points are covered with this approach. Based on the trajectory here and earlier it is very clear that the trajectory is improved using randomly chosen rotational rates compared to constant rotation. The time-averaged acceleration is shown in Figure 5.4 and the result is comparable to the one shown for random rotation rates in Figure 5.2 but is slightly worse. The g-level matches the previous results of $0.03g$ [100], which this algorithm is based on.

Although the g-level is comparable, the trajectory is significantly worsened, as one ideally wants to cover the entire unit sphere, leading to an inferior control algorithm. Changing the constant rotational rates also strongly affects the results and can impact both the trajectory and g-level. This leads to the next potential control algorithm investigated in this thesis.

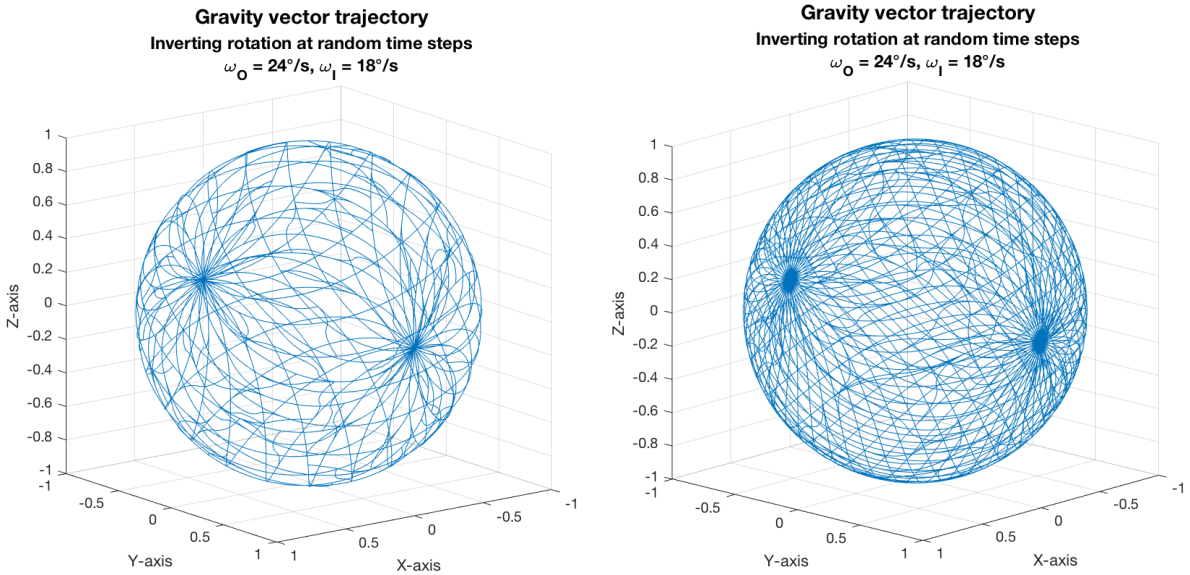

(a) Resulting trajectory allowing 1 s to invert the rotation of the frames. **(b)** Resulting trajectory allowing 2 s to invert the rotation of the frames.

Figure 5.3: Trajectory of the gravity vector after 50 min simulation of randomly inverting the rotational rates every 30 s to 60 s with varying timeframe to reach the new rotational rates.

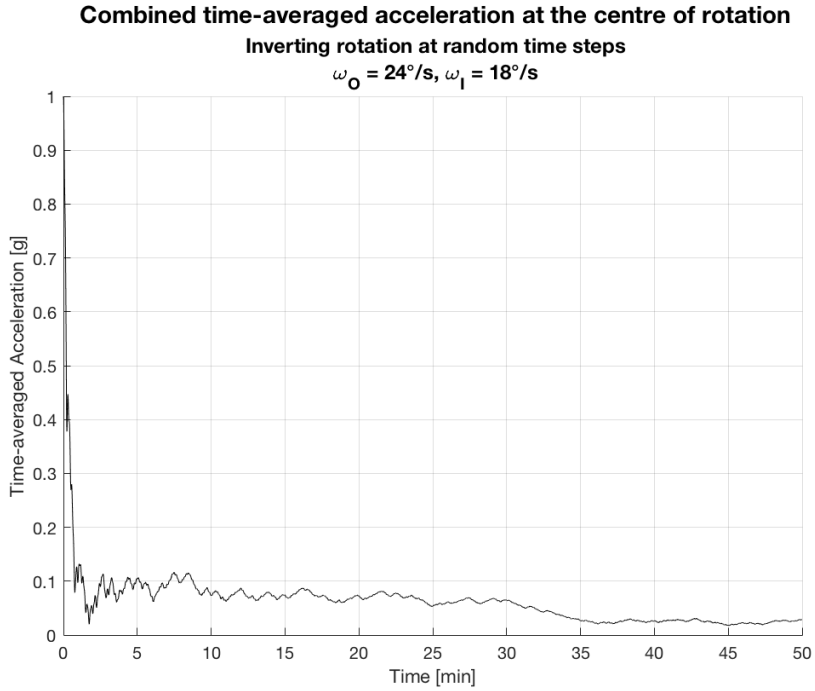

Figure 5.4: Time-averaged g-level after 50 min simulation of randomly inverting the rotational rates every 30 s to 60 s and allowing 1 s to invert the rotation.

5.2.2. Randomly Choose Between a Selection of Rates

This control algorithm is specifically developed to investigate the result of combining the best of the random algorithms and using constant rotational rates. While the benefits of the random algorithms are the more diverse coverage of the unit sphere and the non-constant rotational pattern, the low g-levels of the constant rotational rates are more attractive when trying to simulate microgravity. This algorithm therefore combines the rotational rates that result in the lowest g-levels and randomly chooses between these. The rotational rates are found by mapping a large variety of rates and their resulting g-levels, which is covered in Chapter 6.

24 combinations of rotational rates for the inner and outer frame showed g-levels below $0.0014g$ after 25 min operation. These sets were very similar in their rotational rates, and instead of using only these, some of them were combined with other rotational sets of rates, that also showed low g-levels. These were in the order of $0.0025g$ or less, so only slightly higher than the lowest possible. Five distinctively different sets of rates were chosen, such that more variety is included. These were added to a pool of sets of rates, that the algorithm can randomly pick from. All combinations of rotational direction using the five sets are included in the pool. This means that both frames can rotate in the positive direction, only one of the frames will rotate in the positive direction, or lastly, both frames will rotate in the negative direction. This yields a total of 20 available sets of rates to randomly switch between. To be consistent with the previous algorithms, the rates change every 30 s to 60 s and allow 1 s to decelerate and 1 s to accelerate to the new rates. Applying sets that are noticeably different allows more variation in the trajectory and therefore a better coverage of the unit sphere. Furthermore, using the sets already shown to lead to small g-levels can potentially improve the microgravity simulation.

The list of rotational rates in deg/s is shown in Equation 5.1 with the rate of the outer frame first followed by the inner frame. The trajectory after 50 min is shown in Figure 5.5 and it is clear that more of the unit sphere is covered comparing it to the random rotation. Almost the entire unit sphere is covered and provides an improved trajectory while also providing low g-levels as shown in Figure 5.6. This is an improved way of controlling the RPM, which overcomes some of the problems of constant rotation without compromising the g-level significantly. Whereas the g-levels for constant rates can get as low as $0.001g$ or even a little lower after 50 min. Choosing between these selected sets of rates results in a value of $0.005g$, which is an order of magnitude better than the results of the random algorithms that

provided a resulting acceleration close to $0.03g$. With this small tweak of the algorithm, a remarkable improvement is achieved. One thing that still jumps to the eyes is the creation of the poles, which is significant in this algorithm, where the outer frame more frequently passes by the vertical position resulting in these poles.

$$(\omega_O \ \omega_I) = (\pm 50 \ \pm 14; \ \pm 48 \ \pm 5; \ \pm 44 \ \pm 16; \ \pm 33 \ \pm 13; \ \pm 20 \ \pm 47) \tag{5.1}$$

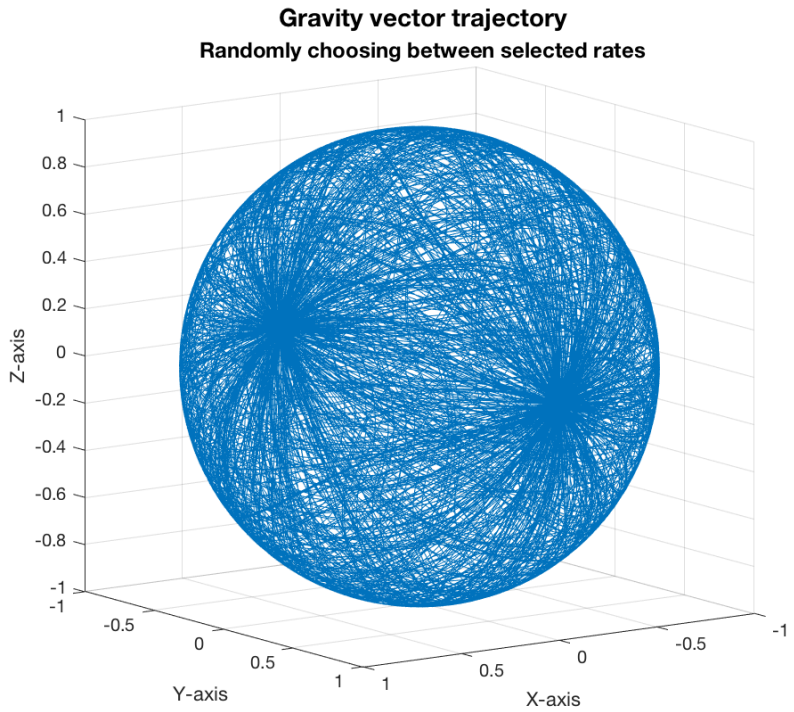

Figure 5.5: Trajectory of the gravity vector after 50 min of randomly switching between carefully selected rotational rates every 30-60 s, and allowing 2 s to reach the new rotational rates.

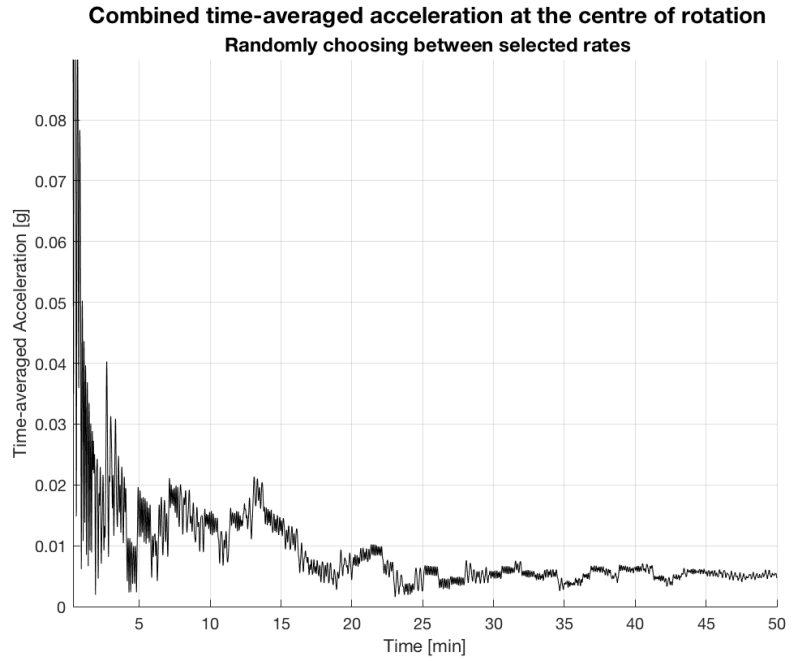

Figure 5.6: Time-averaged acceleration after 50 min of randomly switching between carefully selected rotational rates every 30-60 s, and allowing 2 s to reach the new rotational rates.

5.2.3. Sinusoidal Controls

Another possibility is to have the frames follow a sinusoidal function. This generates a variety of angular velocities that continuously change throughout the rotation. This is an alternative to the constant rotation that has been in focus until now. The benefit of the sinusoidal function is its constantly changing rotation, which provides a natural change of stimulation in the samples. This is due to the constantly changing acceleration levels of the function, which can be modified in many different ways and generate possibilities that are not achievable with constant rotation. For example, it is possible to adjust the sinusoidal function such that the trajectory of the gravity vector only covers part of the unit sphere. This is visualised in Figure 5.7, where the far end of the unit sphere is not covered at all by the gravity vector. This is done by limiting the rotation of the outer frame, such that it does not rotate a full revolution. Generally, the gravity vector should point in all directions equally when trying to generate a state of simulated gravity. It should be clear, that for a good microgravity simulation, the gravity vector should be uniformly distributed around the entire unit sphere, such that the effects of gravity act in all directions on the sample. When in true microgravity, the lack of gravity affects all directions equally, which is what the RPM should replicate in its simulation. However, there can be certain cases where the experimental set-up may not allow for a full rotation of the frames, in which case the sinusoidal function can generate such a trajectory. There are also other ways to achieve this but the sinusoidal function is a simple mathematical expression and does not require extensive programming.

A different use case for the sinusoidal function is to allow the inner frame to not rotate a full rotation but oscillate between certain angles. This can be useful when trying to put tubes on an RPM that should not get tangled up due to the rotation. One such example could be if transportation of liquids is required from the inner frame to a place outside the RPM. To still be able to subtract the liquid, these tubes cannot be allowed to rotate around the outer frame, which limits the rotation of the inner frame to one full revolution. Rotating around the outer frame will get the tubes to get tangled up and if multiple rotations are done it makes it impossible to keep control of the tubes. Allowing the outer frame to rotate freely, it is still possible to point the gravity vector in many directions, and actually, all directions if the inner frame oscillates exactly one full revolution.

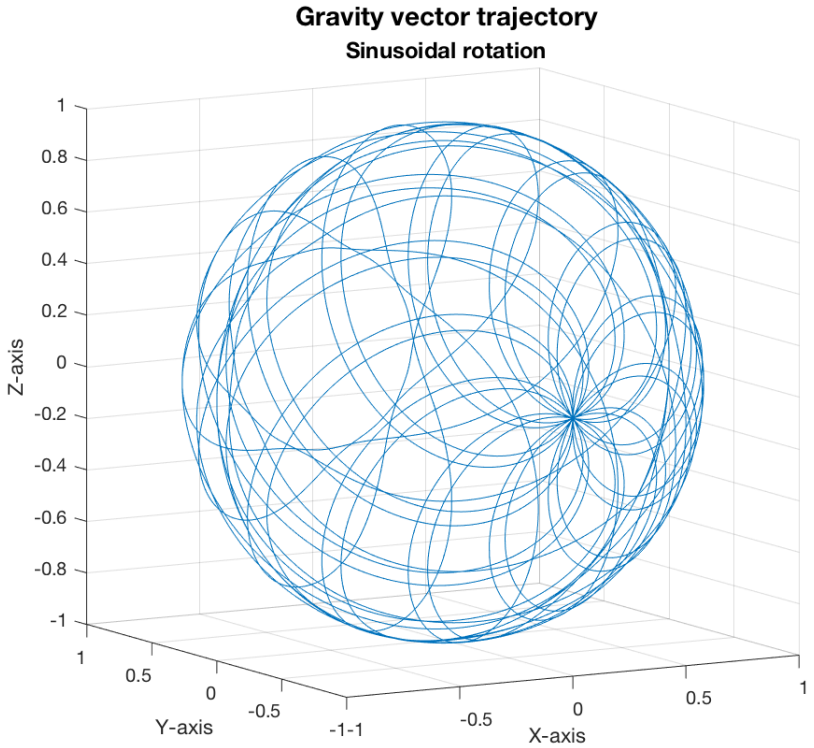

Figure 5.7: Trajectory of the gravity vector after 1 hr of a sinusoidal function that does not allow a full rotation of the outer frame.

5.2.4. Outlook

These are only a few examples of how the RPM can be controlled. Only the imagination sets a boundary for various control algorithms and mixing between these algorithms to reach an improved simulation of microgravity. One thing that most algorithms will have is pole bias, which is caused by the movement of the outer frame. Therefore, the outer frame should minimise its movement through the two generated poles, while the inner frame can be controlled in a different manner. The best option for controlling the two frames might therefore differ from each other. Achieving a low simulated gravity level is much more complicated when trying to avoid pole bias, hence some of the previously presented algorithms might be suitable for simple use cases or in cases where the RPM has already been built. Some cases that might be able to adopt these algorithms are 2D cell cultures or in similar cells as those originally tested on the RPM.

All control algorithms lead to specific g-levels and distinct trajectories of the gravity vector. In the future, more effort can be put into optimising the movement of the RPM, such that the gravity vector is uniformly distributed and the lowest resulting g-level is achieved. This is exactly what the dynamical model of the RPM can provide a platform to experiment with, such that the future use of the RPM is improved.

5.3. Pole Bias

The most important consideration for the quality of the simulation of microgravity in an RPM besides the resulting acceleration is the consideration of pole bias. Most of the discussed algorithms have all shown signs of pole bias, where a certain direction has become dominant over time due to the nature of the RPM. Even though these poles cancel out each other concerning the acceleration, it becomes an interesting topic when considering other qualitative aspects of this way of simulating microgravity. In space, we do not feel the effects of gravity and everything is floating around in true microgravity around $10^{-6}g$. This level of microgravity is present uniformly in all directions at all times, hence when we simulate microgravity using an RPM that contains pole bias, we claim that the two poles cancel out and therefore this method will still be valid. However, on Earth, gravity is constantly present affecting everything. This is also true when we use the RPM. This means that when two directions become dominant, our simulation quality of true microgravity decreases as gravity is no longer acting uniformly in all directions but in distinct directions. Especially in consideration of 3-D cell cultures rather than 2D cell cultures, this becomes an important consideration. A cell will experience gravity more dominantly in two directions as shown in the 2D sketch in Figure 5.8, which can affect the development of the cell differently than what is expected in true microgravity. Ideally, the gravity vector would be spread out uniformly as depicted on the right and not have the resulting gravity be more prominent at the poles, compressing material more significantly at these locations.

Pole bias will affect cells differently than when uniformly distributed, hence it is beneficial to look at solutions to solve the problem to allow for a wider range of use of the RPM. If not dealt with, cells will be affected more around the poles than around their equator in the case of spherical cells. This has a direct influence on the development of the cell and therefore the quality of the simulated microgravity. Mathematically, this effect cancels out but physically it can lead to a wrong simulation and faulty conclusions.

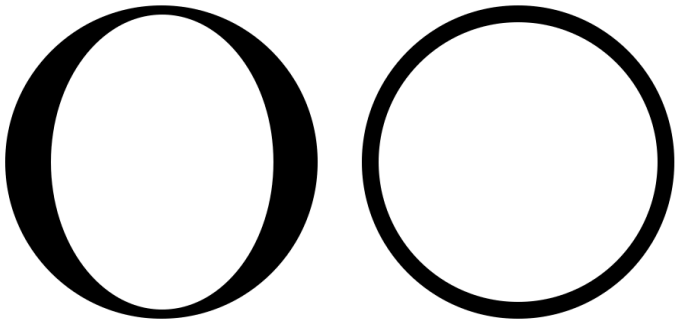

Figure 5.8: 2D sketch of the gravity dispersion in a sphere. To the left, pole bias dominates the sphere whereas gravity is uniformly distributed to the right.

Superposition of Sinusoidal Waves

The first approach investigated is to use a superposition of sinusoidal functions in order to constantly change the orientation of the outer frame while still being able to let it be in the vertical position very rarely. The idea is that only when all the sinusoidal waves are in phase, will the outer frame exactly reach a vertical position, while the rest of the time it will oscillate in between the vertical positions and thereby not generate any poles.

The concept is simple enough to explain, however, it is more difficult to convert it to practice while also generating a low resulting g-level. There are many parameters to control, which can change the outcome significantly with even small adjustments. This has made it very difficult to achieve a trajectory which only exactly reaches the vertical position. Following the efforts of trying to reach only the vertical position very rarely, it should also be noted that the trajectory follows a relatively simple pattern and does not cover the full unit sphere. The example of a sinusoidal control of the outer frame and constant rotation of the inner frame is shown in Figure 5.9. This is the example of the outer frame that only about exactly reaches the vertical position, removing the pole bias. It is also possible to change the parameters, such that only a very narrow part of the unit sphere is covered. When trying to achieve a state of simulated microgravity, this will, however, not be the best option as other options distribute the gravity vector more uniformly.

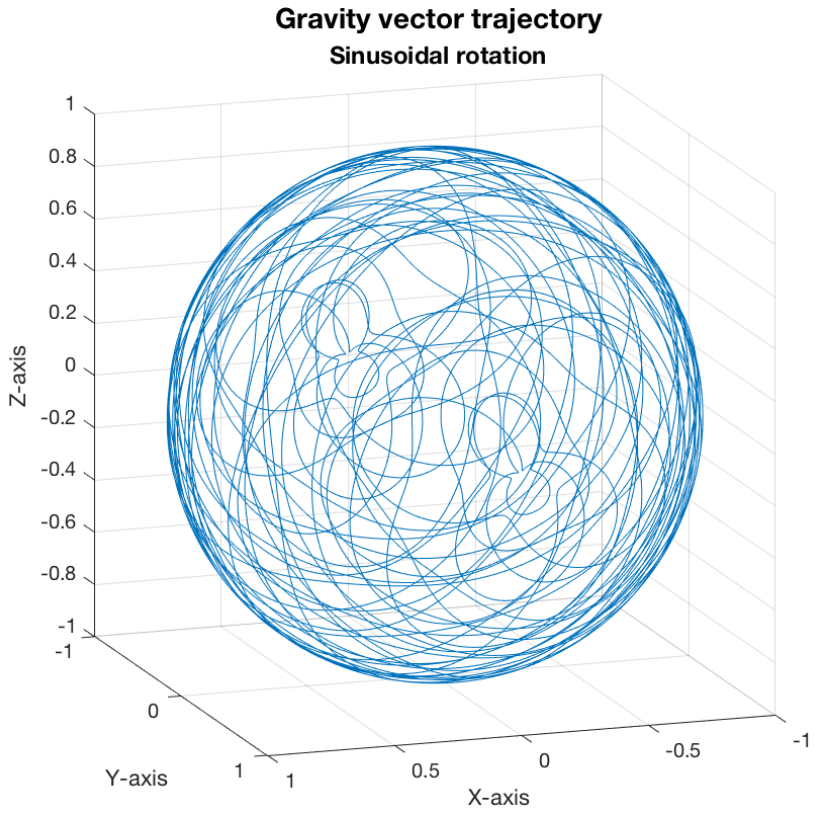

Figure 5.9: Trajectory of the gravity vector after 3 hrs of sinusoidal rotation of the outer frame and constant rotation of the inner frame.

Based on the trajectories of this approach, it can be concluded that it is not an optimal approach for controlling the RPM. The poles might be less significant but the trajectories will never cover the entire sphere and will repeat the same pattern. In the run where the outer frame only just reaches about the vertical position, the resulting g-level becomes $0.02g$ after two hours as shown in Figure A.9. The fluctuation of the resulting g-level is significant but over very long times it will approach low values more consistently.

Instead of rotating the inner frame at a constant rate, it can be interesting to see if more of the unit sphere

can be covered when changing the rate of the inner frame. To test this, the approach of changing the rate in the range from 2 to -2 rev/min is adopted. Simulating a run of 3 hrs shows that more of the unit sphere is covered, however, not all of the unit sphere will be covered. If looking from the side, it is also clear that certain areas are visited more by the gravity vector compared to others. These look like stripes of darker blue where the gravity vector visits more. It is a significant improvement from having the inner frame rotate at a constant rate but it is not the optimal option for controlling the RPM.

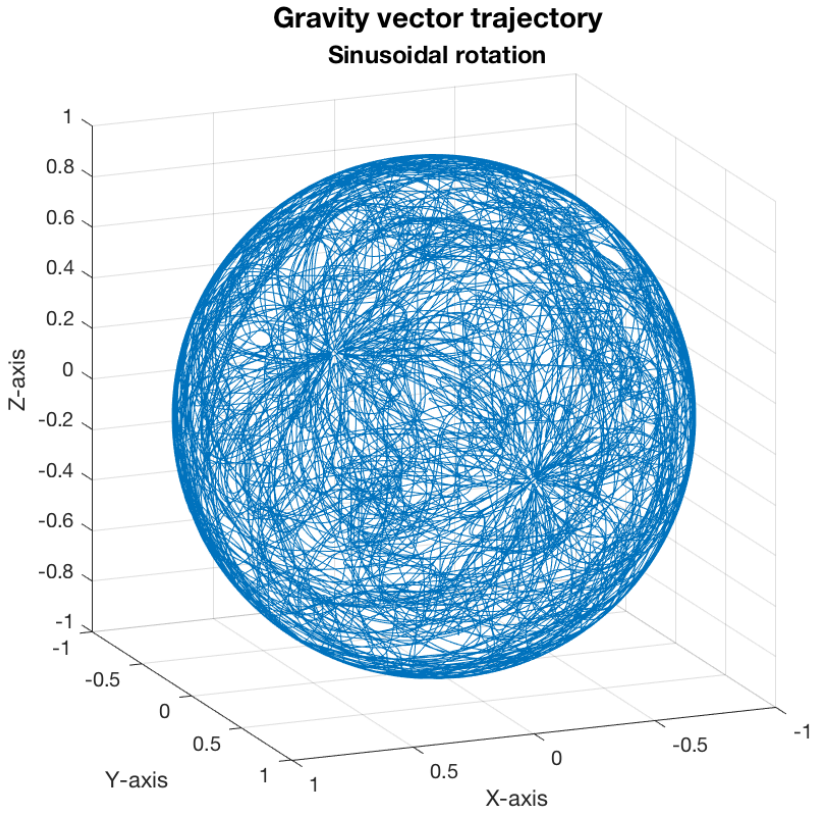

Figure 5.10: Trajectory of the gravity vector after 3 hrs of sinusoidal rotation of the outer frame and randomly changing the rotation of the inner frame in the range from 2 to -2 rev/min.

Design with Three Frames

Another possibility to improve the RPM is to consider the mechanical design instead of only the control software. Following the derivation of the model for two frames, three frames can be modelled similarly by just adding another frame and adding the respective equations. In Figure 5.11 the coordinate system for the three framed RPM is shown, with subscript I and O still indicating the inner and outer frame, respectively, whereas M indicates the middle frame. Adding a third frame allows for avoiding pole bias at each full rotation of the outer frame.

Building on from Chapter 3 the equations related to this new design are shown below. This time τ indicates the angle between the outer frame and the global frame, whereas σ becomes the angle between the middle frame and the outer frame, and finally, θ becomes the angle between the inner frame and the middle frame. For the added frame, the rotational matrix about the x-axis is valid for any rotation τ, like the rotation θ is valid for the inner frame. These matrices can be seen in Equation 3.1 and 3.2.

The angular velocity is shown in Equation 5.2, with the change in angular velocity being defined the same way as earlier by the difference between the current and previous angular velocity divided by the corresponding time step.

$$\boldsymbol{\omega}_G = \boldsymbol{\omega}_O +_G \boldsymbol{R}_O \cdot \boldsymbol{\omega}_M +_G \boldsymbol{R}_O \, {}_O\boldsymbol{R}_M \cdot \boldsymbol{\omega}_I \tag{5.2}$$

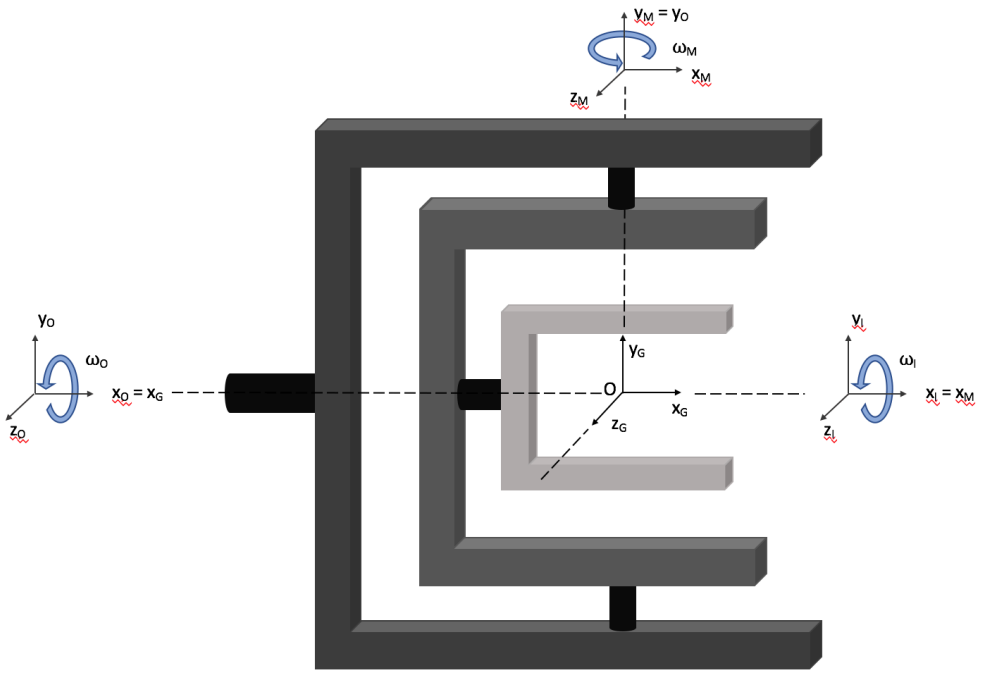

Figure 5.11: Coordinate system of an RPM with three frames.

The angular acceleration is first defined for the individual frames in Equation 5.3 to Equation 5.5 and then combined into one expression in Equation 5.6.

$$(\dot{\boldsymbol{\omega}}_O)_{x_G,y_G,z_G} = (\dot{\boldsymbol{\omega}}_O)_{x_O,y_O,z_O} + \boldsymbol{\omega}_O \times \boldsymbol{\omega}_O = (\dot{\boldsymbol{\omega}}_O)_{x_O,y_O,z_O} \tag{5.3}$$

$$(\dot{\boldsymbol{\omega}}_M)_{x_G,y_G,z_G} = {}_G\boldsymbol{R}_O \cdot (\dot{\boldsymbol{\omega}}_M)_{x_O,y_O,z_O} + \boldsymbol{\omega}_O \times ({}_G\boldsymbol{R}_O \cdot \boldsymbol{\omega}_M) \tag{5.4}$$

$$(\dot{\boldsymbol{\omega}}_I)_{x_G,y_G,z_G} = {}_G\boldsymbol{R}_M \cdot (\dot{\boldsymbol{\omega}}_I)_{x_O,y_O,z_O} + (\boldsymbol{\omega}_O \times ({}_G\boldsymbol{R}_O \cdot \boldsymbol{\omega}_M)) \times ({}_G\boldsymbol{R}_M \cdot \boldsymbol{\omega}_I) \tag{5.5}$$

$$\boldsymbol{\alpha}_G = \dot{\boldsymbol{\omega}}_G = (\dot{\boldsymbol{\omega}}_O)_{x_G,y_G,z_G} + (\dot{\boldsymbol{\omega}}_M)_{x_G,y_G,z_G} + (\dot{\boldsymbol{\omega}}_I)_{x_G,y_G,z_G} \tag{5.6}$$

With the angular accelerations set, it is time to look at the velocity. Adding an extra rotating frame to the system gives another set of equations, that can be found using the same approach as in section 3.1. This leads to the expressions for the velocities shown in Equation 5.11 to 5.13, where both the total velocity as well as the velocities of the moving frames, which is used to find the Coriolis acceleration, are shown. The general system of three rotating frames and its corresponding equations are shown in Figure 5.12 and Equation 5.7 to Equation 5.10, respectively to clarify the origin of the expressions.

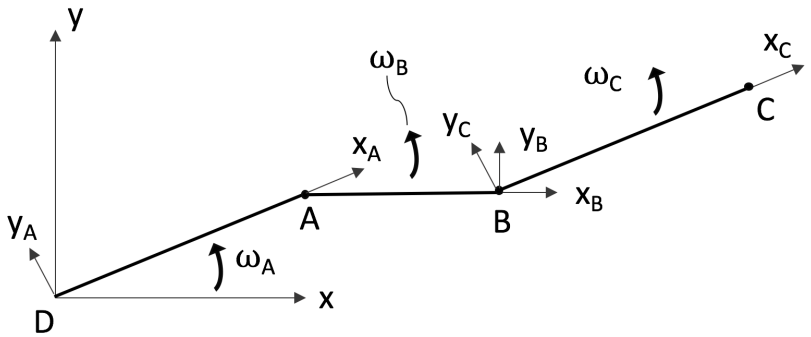

Figure 5.12: Sketch of a general system with three rotating frames.

$$ {}_D\boldsymbol{V}_C = {}_D\boldsymbol{V}_B + \cancelto{0}{{}_B\boldsymbol{V}_C|_{\omega_C=0}} + {}_D\boldsymbol{\omega}_C \times_B \boldsymbol{P}_C \tag{5.7} $$

$$ {}_D\boldsymbol{V}_B = {}_D\boldsymbol{V}_A + \cancelto{0}{{}_A\boldsymbol{V}_B|_{\omega_B=0}} + {}_D\boldsymbol{\omega}_B \times_A \boldsymbol{P}_B \tag{5.8} $$

$$ {}_D\boldsymbol{V}_A = \cancelto{0}{{}_D\boldsymbol{V}_d} + \cancelto{0}{{}_d\boldsymbol{V}_A|_{\omega_A=0}} + {}_D\boldsymbol{\omega}_A \times_d \boldsymbol{P}_A \tag{5.9} $$

$$ {}_D\boldsymbol{V}_C = {}_D\boldsymbol{\omega}_C \times_B \boldsymbol{P}_C + {}_D\boldsymbol{\omega}_B \times_A \boldsymbol{P}_B + {}_D\boldsymbol{\omega}_A \times_d \boldsymbol{P}_A \tag{5.10} $$

In the following equations, ${}_O\boldsymbol{\omega}_P = {}_O\boldsymbol{\omega}_M + {}_O(M\boldsymbol{\omega}_I)$ and similarly for ${}_G\boldsymbol{\omega}_P = {}_G\boldsymbol{\omega}_O + {}_G({}_O\boldsymbol{\omega}_M) + {}_G({}_M\boldsymbol{\omega}_I)$. Equation 5.12 is used as the moving frame velocity for the outer frame to find the Coriolis acceleration contribution and Equation 5.13 is used for the middle frame.

$$ {}_G\boldsymbol{V}_P = {}_M\boldsymbol{\omega}_P \times_M \boldsymbol{P}_P + {}_O\boldsymbol{\omega}_P \times_O \boldsymbol{P}_P + {}_G\boldsymbol{\omega}_P \times_G \boldsymbol{P}_P \tag{5.11} $$

$$ {}_O\boldsymbol{V}_P = {}_M\boldsymbol{\omega}_P \times_M \boldsymbol{P}_P + {}_O\boldsymbol{\omega}_P \times_O \boldsymbol{P}_P \tag{5.12} $$

$$ {}_M\boldsymbol{V}_P = {}_M\boldsymbol{\omega}_P \times_M \boldsymbol{P}_P \tag{5.13} $$

With the velocity set, it is now time to complete the model and set up equations for the acceleration. The model can be extended from two frames to three, simply by applying the same acceleration equation for the new frame and correcting the contributions of each part. These equations are shown in Equation 5.14 to Equation 5.16.

$$ {}_G\boldsymbol{a}_P = \boldsymbol{a}_G + {}_O\boldsymbol{a}_P + ({}_G\boldsymbol{a}_P)_{centripetal} + ({}_G\boldsymbol{a}_P)_{Coriolis} + ({}_G\boldsymbol{a}_P)_{Euler} \tag{5.14} $$

$$ {}_O\boldsymbol{a}_P = \cancelto{0}{\boldsymbol{a}_M} + {}_M\boldsymbol{a}_P + ({}_O\boldsymbol{a}_P)_{centripetal} + ({}_O\boldsymbol{a}_P)_{Coriolis} + ({}_O\boldsymbol{a}_P)_{Euler} \tag{5.15} $$

$$ {}_M\boldsymbol{a}_P = \cancelto{0}{\boldsymbol{a}_I} + \cancelto{0}{{}_I\boldsymbol{a}_P} + ({}_M\boldsymbol{a}_P)_{centripetal} + ({}_M\boldsymbol{a}_P)_{Coriolis} + ({}_M\boldsymbol{a}_P)_{Euler} \tag{5.16} $$

This leads to the following final expressions for the acceleration. This includes all acceleration imposed by adding a third frame to the RPM and is dependent on the rotational rates of the frames and the location of the point P. The terms are all being converted to the G-frame where applicable, such that the final expression is given fully in terms of the static global frame. This is done using the rotational matrices and converting from the M or O-frame to the G-frame. This is noted by the square brackets and subscripts, such that e.g. ${}_G[{}_M\dot{\boldsymbol{\omega}}_I \times_M \boldsymbol{P}_I]_M$ is calculated in the M-frame but then converted to the G-frame using rotational matrices.

$$ {}_G\boldsymbol{a}_P = \begin{bmatrix} 0 \\ 0 \\ -g \end{bmatrix} + [{}_O\boldsymbol{a}_P]_G + {}_G\boldsymbol{\omega}_O \times ({}_G\boldsymbol{\omega}_O \times_G \boldsymbol{P}_I) + 2\,{}_G\boldsymbol{\omega}_O \times_O \boldsymbol{V}_P + {}_G\dot{\boldsymbol{\omega}}_O \times_G \boldsymbol{P}_I \tag{5.17} $$

$$ [{}_O\boldsymbol{a}_P]_G = [{}_M\boldsymbol{a}_P]_G + {}_G[{}_O\boldsymbol{\omega}_M \times ({}_O\boldsymbol{\omega}_M \times_O \boldsymbol{P}_I)]_O + {}_G[2\,{}_O\boldsymbol{\omega}_M \times_M \boldsymbol{V}_P]_O + {}_G[{}_O\dot{\boldsymbol{\omega}}_M \times_O \boldsymbol{P}_I]_O \tag{5.18} $$

$$ [{}_M\boldsymbol{a}_P]_G = {}_G[{}_M\boldsymbol{\omega}_I \times ({}_M\boldsymbol{\omega}_I \times_M \boldsymbol{P}_I)]_M + {}_G[{}_M\dot{\boldsymbol{\omega}}_I \times_M \boldsymbol{P}_I]_M \tag{5.19} $$

These equations are valid for an RPM with three frames instead of two and can be used to evaluate the resulting g-level of a run, whereas the rotational matrices and the three angles τ, σ and θ can be used to determine whether or not three frames can be used to overcome the problem of pole bias.

Building on the previous work on control algorithms, it is possible to combine the control algorithms that are expected to yield good results for a three-framed RPM. Having the inner and middle frame rotate using the selected rates that yielded low g-levels while letting the outer frame rotate at a constant rate shows good results both with respect to the trajectory of the gravity vector and the resulting g-level, which can be seen in Figure 5.13 and 5.14, respectively. In the latter, the g-level of a completely random mode is also plotted as a reference. They perform relatively similarly with three frames being a little better but more importantly, avoiding pole bias. This could therefore serve as a great improvement to using randomised controls on a two-framed RPM.

The g-level is below $0.01g$ and there is no pole bias in the trajectory, which clearly covers all of the unit sphere. However, looking closely at the trajectory, it is possible to see that the gravity vector visits the

equator of the sphere at the x = 0 axis slightly more than the rest. This is still a significant improvement compared to the trajectories shown for the two-framed RPM across all the control algorithms covered here but is something to be aware of. The gravity vector is much more uniformly distributed and follows a random pattern that changes as the rotational rates of the frames change. Adding an extra frame to the RPM can therefore serve as a simple way to overcome pole bias. It is much easier to mechanically add an extra frame rather than writing a complex algorithm.

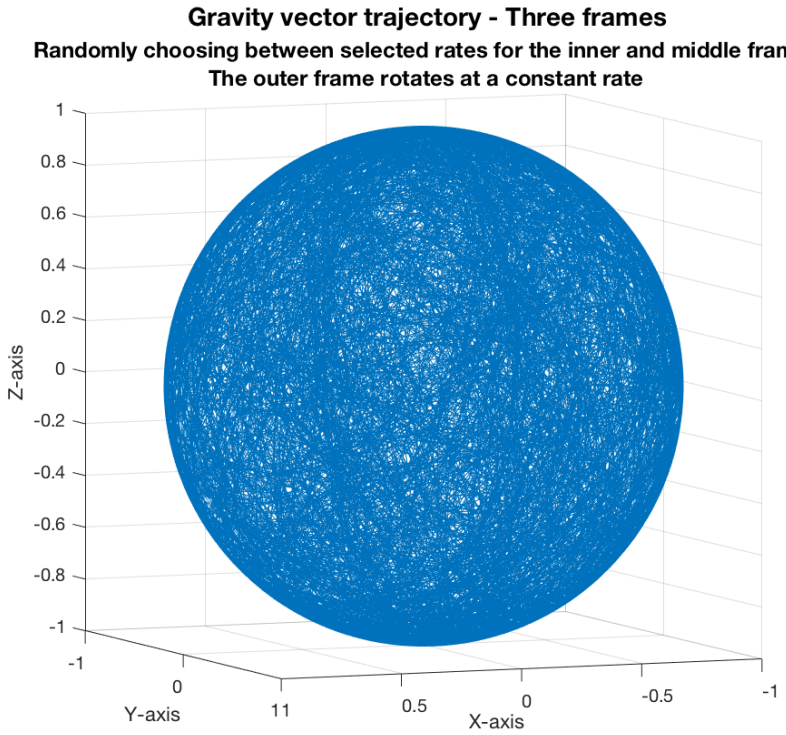

Figure 5.13: Trajectory of the gravity vector after 83 min of a constant rotation of the outer frame at ω_O = $27°\text{s}^{-1}$ while the inner and middle frame rotate by randomly choosing one of the selected sets of rotation shown earlier.

This is, however, not the only combination to control the three frames. Whether it is the outer, middle or inner frame that is set to rotate at a constant rate while the others change shows no difference in the results. The trajectory will still be the same, just as the resulting g-level will also be about the same value. Changing the outer frame's rotation to a value that changes simultaneously with the other's did not show any improvement to the trajectory but looked similar to Figure 5.13.

Using the sinusoidal function to control the outer frame, while leaving the two other frames to rotate randomly at the set rates, will lead to the generation of the poles again. These poles will be less dominant than for two frames and depend on the nature of the sinusoidal function. The trajectory is shown in Figure 5.15 with the two poles marked by the arrows. The poles are much more difficult to visualise for three frames because they are less dominant but they still show up when using the sinusoidal control algorithm.

Using constant rotational rates for all three frames will, similarly to the two-framed RPM, result in distinct patterns, which are just more complicated. The trajectories generated will not contain any poles but they still do not cover the entire unit sphere, which is why changing rates is still the best option. In Figure 5.16, the trajectory is shown when the three frames rotate ω_O = $23°\text{s}^{-1}$, ω_M = $17°\text{s}^{-1}$ and ω_O = $13°\text{s}^{-1}$. This is just one example of a trajectory, and it should be clear that this trajectory changes if any of the rates are changed.

Of all the possible designs presented, a three-framed RPM with one frame rotating at a constant rate and the two others randomly rotating based on a selection of carefully selected rotational sets still serves as the best option in combining a low g-level with a uniformly distributed gravity vector trajectory. This method is significantly better at distributing the gravity vector evenly while it also has very low resulting

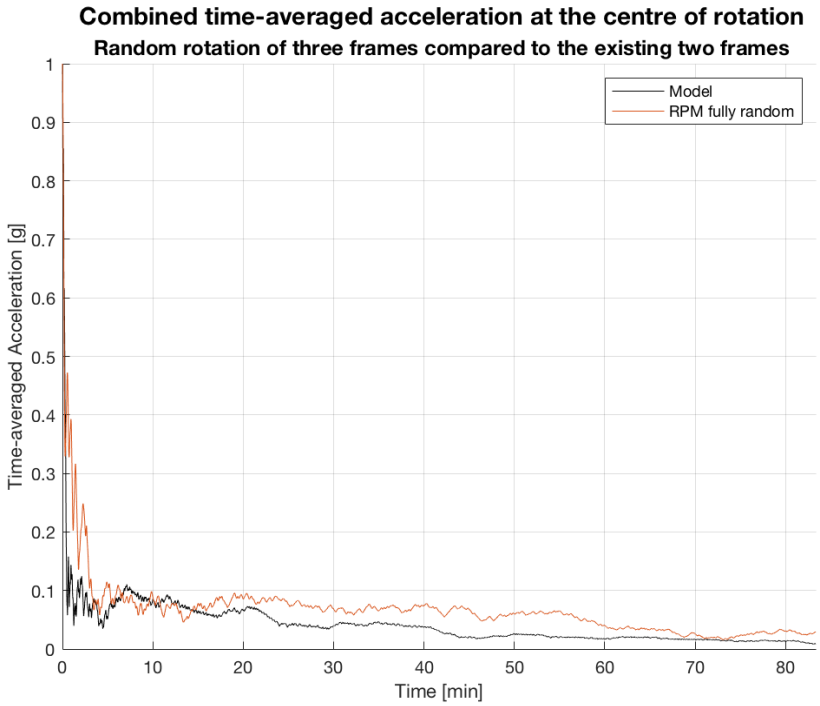

Figure 5.14: Resulting g-level after 83 min of a constant rotation of the outer frame at $\omega_O = 27°\text{s}^{-1}$ while the inner and middle frame rotate by randomly choosing one of the selected sets of rotation shown earlier. The orange line shows the result of a two-frame RPM at completely random rotation for reference.

g-levels. When choosing the rates, it is important that the frames do not have the same rotational rates, as that will result in inferior results. This is the same case for the two-framed RPM, as presented in Chapter 6.

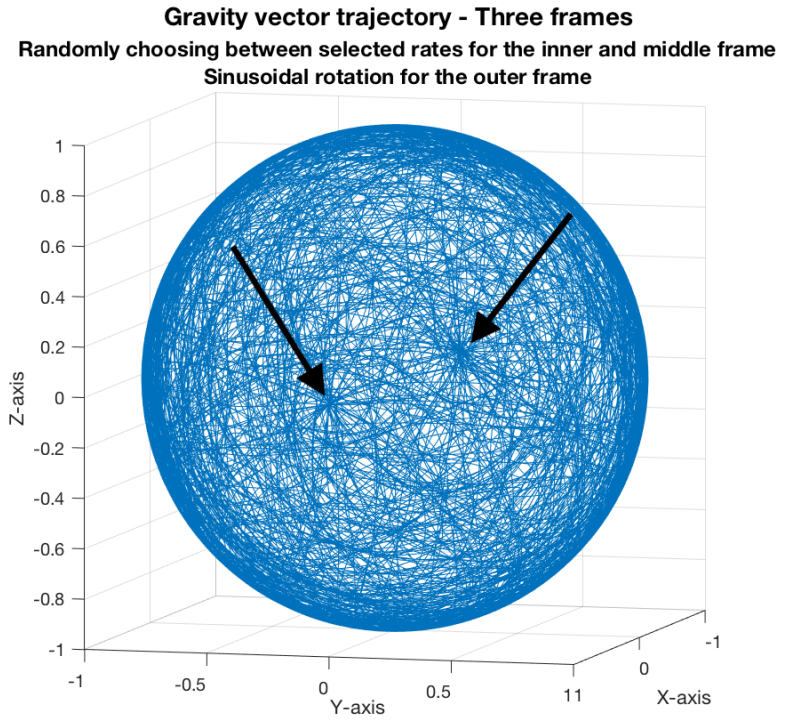

Figure 5.15: Trajectory of the gravity vector after 46 min of a sinusoidal rotation of the outer frame while the inner and middle frame rotate by randomly choosing one of the selected sets of rotation shown earlier.

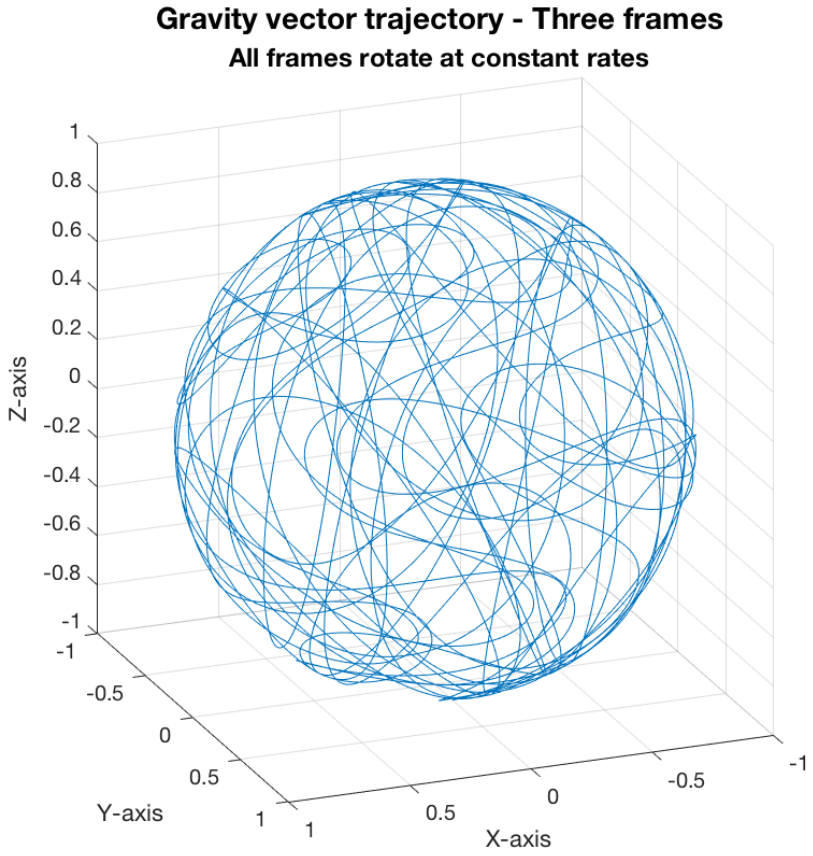

Figure 5.16: Trajectory of the gravity vector after 81 min of constant rotation for all frames. ω_O = $23°\text{s}^{-1}$, ω_M = $17°\text{s}^{-1}$ and ω_O = $13°\text{s}^{-1}$.

5.4. Partial Gravity Control

One of the benefits of using an RPM is the possibility to manipulate the gravity vector, so the resulting g-level reaches hypogravity levels. This can be used to study the gravity dose response in cells and organoids and serve as an important platform in preparation for future missions to the Moon and Mars, and to understand the effects of gravity for Earth-based applications. As of now, we are not able to reach these g-levels easily on the Moon or Mars, making the RPM a unique tool in our understanding of these gravity levels on human physiology. Reaching these hypogravity levels in the RPM is covered here.

There are two approaches to take in order to reach hypogravity levels. The first one is to use the RPM in combination with a centrifuge. Applying the RPM for microgravity, and adding the element of the centrifuge to generate hypogravity levels will result in a simulation of the desired gravity level depending on the rotation of the centrifuge. The other approach is to control the software of the RPM such that the resulting g-level is at the required hypogravity level. Both these approaches have been compared and they show similar results in cell growth and proliferation [110]. Here, the interest is solely on the RPM and including a centrifuge for physically larger RPMs might become a problem, hence only the software solution is explored.

There are two hypogravity levels of particular interest in gravity-related research, that is the Moon and Mars gravity levels. The benefit of these is that they are very distinct, and can provide answers related to future space missions. They also provide different doses of gravity, making it possible to show the gravity dose response for various systems. This can help us understand gravity better and its effect on life. This is a very important aspect of using the RPM in human physiology studies, as the various hypogravity levels can tell us something about the dose-response of certain physiological aspects. Manipulating the gravity vector to spend more time acting from the top of the sample towards

its bottom, allows the achievement of partial g-levels. Depending on how much more time the gravity vector spends in this direction one can achieve both Moon and Mars or even higher g-levels.

The simplest way to manipulate the resulting gravity is to alter the rotational rate of the outer frame, such that the gravity vector points in one direction for longer than the other direction. This can be done very simply by weighing the rotation of the outer frame. It should be said, that the inner frame also can be used to generate partial gravity levels, however, with the rotation of the outer frame always letting the gravity vector point in the lateral direction twice each rotation, it is easier to control the partial gravity using the outer frame.

Using a factor η, the angular velocity of the outer frame can be weighted by the initial rotational rate ω_{init} as seen in Equation 5.20. The angle is calculated at each time step *k* as shown in Equation 5.21, with the initial angle being zero. The term dt indicates the time between each timestep.

$$\omega = \omega_{init} + \eta\,\omega_{init}\,sin\left(\omega_{init} \cdot t\right) \tag{5.20}$$

$$\sigma\left(k+1\right) = \sigma\left(k\right) + \omega\left(k\right) \cdot dt \tag{5.21}$$

These expressions will allow the gravity vector to point more towards one direction, leading to a higher resulting g-level. Changing the value of η will make it possible to alter and achieve the required simulated g-level. It is the simplest possible expression for manipulating the gravity vector and the partial g will be in the y-direction, as the outer frame will point more downwards than upwards. Using this approach therefore also requires proper sample alignment. It does not help to look at the effects of gravity in the wrong direction, then the simulated g-level will be wrong as the direction of gravity is wrong. The time-averaged acceleration in each direction can be seen in Figure 5.17, where it is clear that the y-direction is the direction of the partial g.

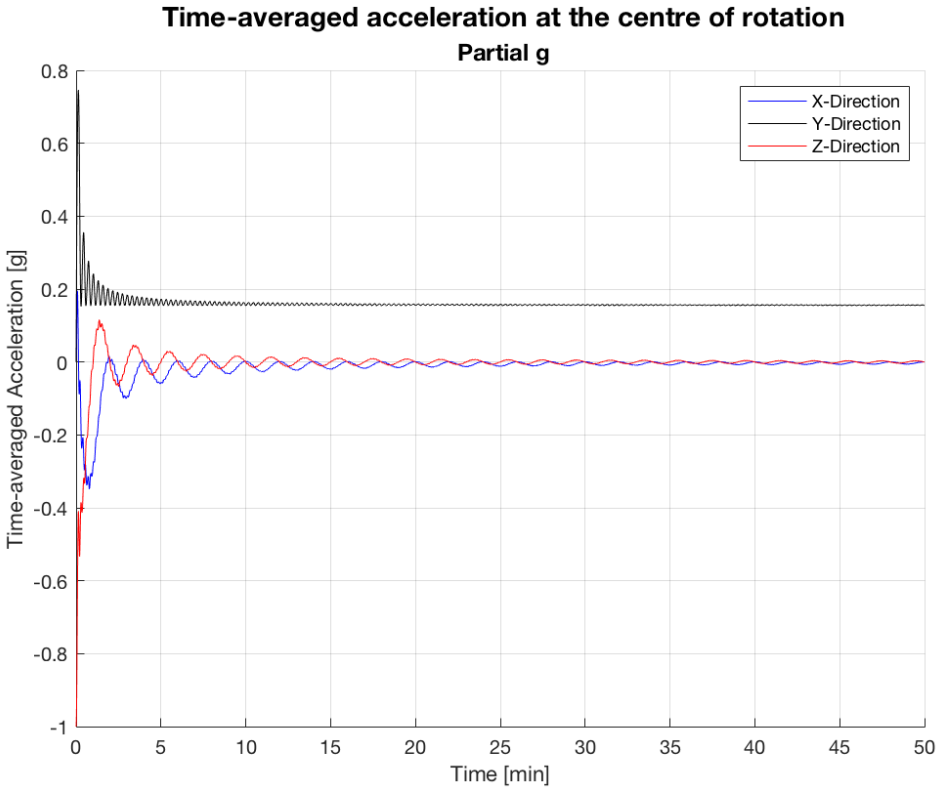

Figure 5.17: The time-averaged acceleration in the three directions during a partial g run.

Like for the other control algorithms, this is just one possible way of achieving partial g-levels. There are many more ways to program the rotation, such that the effective gravity approaches a steady level in

the hypogravity regime, such as the Moon and Mars gravity levels. They all build on the same principle, however, that the gravity vector points more in certain directions.

Alternatively, it is also possible to achieve partial gravity by moving further away from the centre of rotation, thereby letting the residual accelerations become dominant. As shown in the equations in Section 3.1, there are terms of the acceleration which depend on the placement of the sample and the angular velocity. This implies that rotating faster and moving further away from the centre of rotation leads to increased acceleration terms. The centripetal acceleration can be increased by both increasing the angular velocity and by moving the sample further away from the centre of rotation. The Coriolis acceleration term can be increased by increasing the angular velocity and finally, the Euler term can increase with an increasing distance between the centre of rotation and the sample. With these tools, it is possible to adapt the resulting gravity level for simulating partial g. Rotating the RPM too fast can lead to undesired effects in the samples but there is also a limit to which g-levels that are achievable depending on the size of the RPM. This will follow in Section 6.3, where running the RPM with multiple g-levels at different locations are discussed. However, this solution requires a very large RPM to achieve Mars's gravity level or values closer to Earth's gravity. Therefore, it might not be the most efficient way to achieve partial g, especially if values close to Earth's gravity level are required. This is an option, however, to have experiments run simultaneously across the gravity spectrum, given that the RPM is big enough and rotates fast enough.

Finally, a third option would be to generate a partial gravity environment by placing the RPM on a centrifuge and letting the centrifuge generate the required g-level. That way microgravity is still simulated on the sample in the RPM, while the centrifuge provides good controls to achieve these partial gravity levels. This requires significant additional equipment and will be more difficult to come by but it is not impossible to generate partial gravity this way.

6

Results

This chapter focuses on the results of the model during constant rotational rates. Using it to investigate the sizing of experiments, which rotational rates are good, and if it is possible to use the RPM for studies across the entire gravity spectrum will be discussed in the subsequent sections. The combination of rotational rates of the two frames has a significant impact on the performance of the RPM. To maximise its use, a large variety of rotational rates are covered and plotted in Section 6.1 to show the resulting g-levels and allow future studies to benefit from the results. In addition to this, it can be difficult to evaluate how large experiments can be while still being considered to experience microgravity. This is true for all scientists using an RPM across all disciplines. With the established model, it becomes possible to answer these questions for any case. The g-level is dependent on the angular velocities of the two frames and the position of the sample, which means that there are many possibilities for scaling experiments based on the operational conditions. The model can be changed to predict the performance for specific cases, but only some coarse guidelines will be given in Section 6.2 as they will differ from experiment to experiment. A final interesting idea is to have an RPM that can be used across the entire gravity spectrum. As previously discussed, additional accelerations will occur when moving away from the centre of rotation. If moving far enough way, these accelerations will become dominant and the RPM will be able to function similarly to a centrifuge and cover the entire gravity spectrum given a large enough platform. The sizing of such a platform is discussed in Section 6.3.

6.1. Lowest Resulting g-Level

Throughout the presented results, it has been clear that the resulting g-level and trajectory of the gravity vector heavily depend on the chosen rotational rates of the two frames. In this section, the focus is to map a large variety of rotational rates to show which rotational rates provide the lowest g-levels and which to avoid. When using constant rates, the time-averaged acceleration drops quickly and keeps dropping at a slower pace throughout a run. As the focus is on the number of mapped rates, only the first 25 min of a run is considered. This allows for a significant decrease in simulation time as 2500 options are being mapped. The rates of both frames vary from $1°s^{-1}$ to $50°s^{-1}$, and every possible option in this range is considered. The values are taken as an average of the 300 last values to minimise the effects of the periodic nature of the time-averaged acceleration. The average of the 300 last datapoints provides the average g-level of the last 30 s of a run.

Mapping the resulting g-level of the various rates clearly shows that it is undesirable to let the two frames rotate close to the same rates. This can be seen in the diagonal in Figure 6.1, which shows significantly higher g-levels than the rest of the map. When the frames are rotating at the same rate, the g-level is around $0.5g$ and it will never be lower as the gravity vector stays in the lower part of the unit sphere, as presented earlier in Figure 4.17. There is a large difference between the highest and lowest g-levels, indicating, as expected, that it is beneficial to avoid rotating the two frames at the same rate. It is possible to achieve a much better simulation of microgravity simply by letting the frames rotate at different rates. Therefore, never use the RPM to rotate the frames at the same rate.

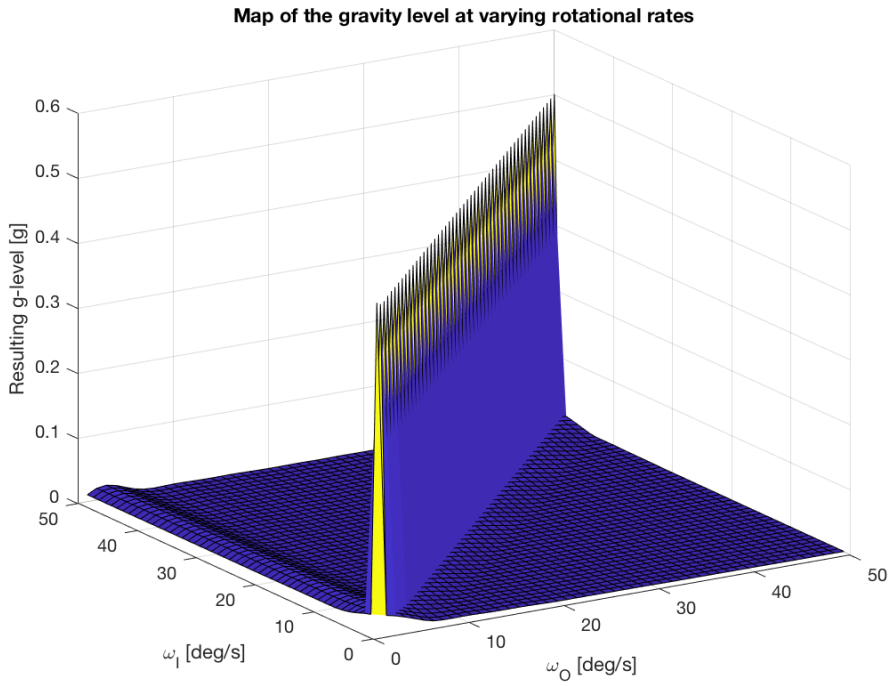

Figure 6.1: Map of the corresponding g-level after 25 min with varying the rotation rate of the frames between $1°s^{-1}$ and $50°s^{-1}$.

To showcase a more detailed view of the better-performing rotational rates, the diagonal values have been left out in Figure 6.2. Now the g-levels are closer to each other and it becomes evident that there are still certain rotation rates to stay clear of. However, the exact rotational rates can still be difficult to find in this figure. It is possible to say that having the outer frame rotate at low rates is clearly not advantageous. Up until $\omega_O = 5°s^{-1}$, one will experience significantly higher g-levels compared to the rest of the rotational rates. The next evident aspect is that having the two frames rotate within a few degrees of the same angular velocity also yields higher acceleration levels. Despite the diagonal values being left out, the values near the diagonal still show higher g-levels, hence these should also be avoided.

An aspect that cannot be included in this graph is the trajectory of the gravity vector, which ideally would cover a significant part of the unit sphere to improve the quality of the simulated microgravity. Before running an experiment, the trajectory can be checked, or similarly, if two sets of rates are almost identical in performance, it is possible to choose the one that spreads out the gravity vector more to improve the simulation. This can easily be done by comparing the trajectories of the two sets of rates in consideration. Comparing the vast amount of trajectories is not feasible but can easily be done at a small scale if considering only a few options. As seen in both Figure 6.2 and Figure 6.3, the higher rotational rates of the outer frame yield lower g-levels but will also cause other problems. Rotating the outer frame faster will force the gravity vector to move through the poles more frequently as the outer frame is in the vertical position more often. This can potentially affect the simulation of microgravity as discussed earlier and remains one of the cases where using three frames on the RPM is particularly useful.

However, if the sample is larger than just a point at the centre, it might be useful to consider how the resulting g-level will be at the furthest parts of the sample. The higher rates, which at the centre of rotation might result in small g-levels, can at further distances from the centre prove to exceed those of the lower rates, thereby changing the optimum rotational rates. The larger the RPM and sample become, the more important this aspect will be. A couple of cm will not make a huge difference but going beyond that can definitely affect the simulated microgravity environment. As the auxiliary accelerations increase at increased rotational speeds, it also means that these high rotation rates are more susceptible to change significantly if experiments are done with large samples.

The use of the RPM remains very specific depending on the sample, which makes it difficult to tell which rates are the optimal ones. With different experiments come different needs, and some relatively fast processes might force speeding up the RPM, while for other processes with large samples, it might be beneficial to slow the frames down to avoid introducing additional accelerations.

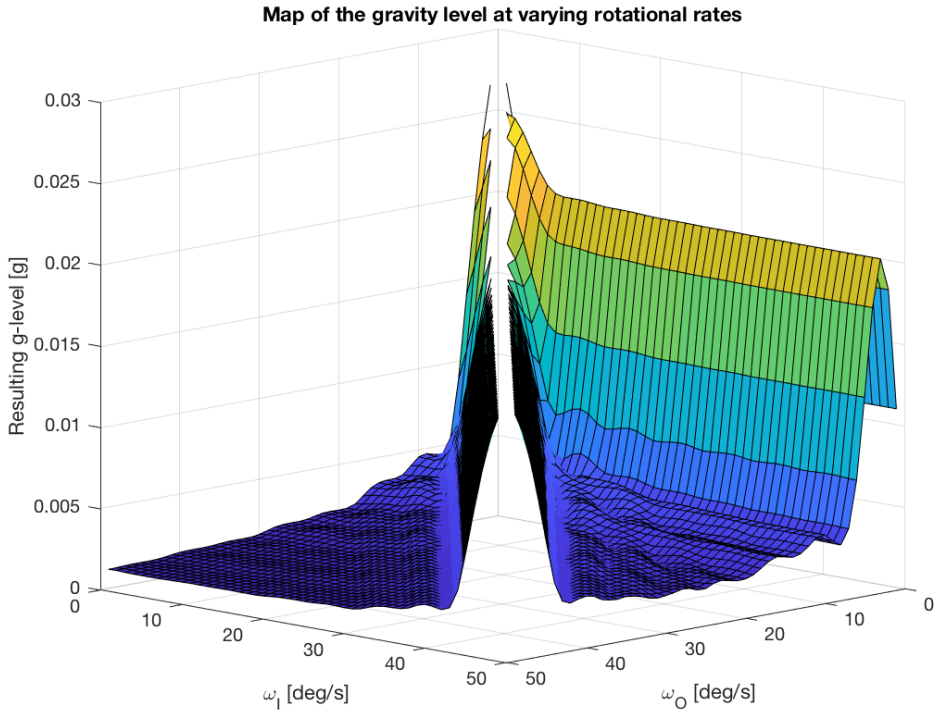

Figure 6.2: Map of the corresponding g-level after 25 min with varying the rotation rate of the frames between $1°s^{-1}$ and $50°s^{-1}$. The diagonal has been left out to show more details on the remaining options for rotational rates.

To further increase the level of detail, the low rates of the outer frame and additional values close to the diagonal have been left out. The perspective is also changed to a top view, and it can easily be seen that the lowest accelerations are at the fastest rates of the outer frame and low rates of the inner frame. Locally, it is also possible to achieve some lower g-levels at around $30°s^{-1}$ for the outer frame and high rates of the inner frame but these values are higher than the first option.

The lowest g-levels obtained are between $0.0013g$ and $0.0014g$. There are a total of 24 sets, where this level is achieved and the majority is when the outer frame rotates at $50°s^{-1}$. These are presented in Table B.1. The results, which extend beyond the few sets that are below $0.0014g$, can be used to choose the better-performing constant rates. Some of these have been chosen for the previous algorithm, which randomly picks the rotational rates of the frames from a small selection of options.

There are better ways to control the original two-framed RPM by not using constant rotation, however, with the three-framed RPM it is still possible to benefit from the simplicity of the constant rotational rates while also avoiding significant pole bias by adding the extra frame.

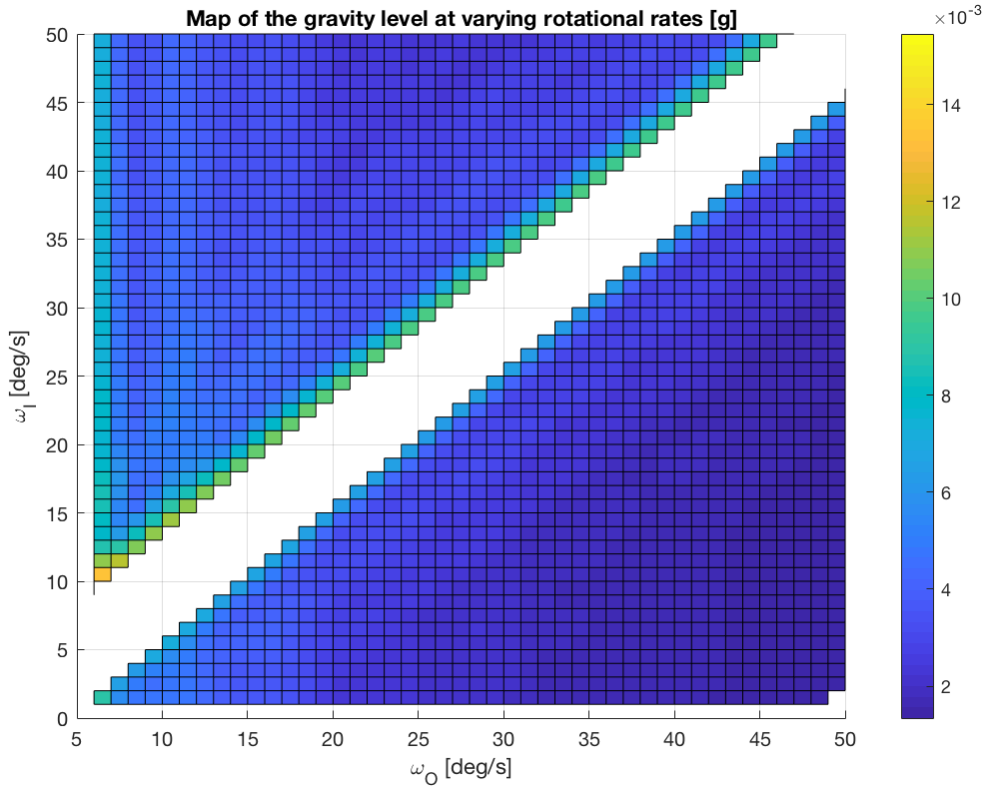

Figure 6.3: Map of the corresponding g-level after 25 min with varying the rotation rate of the frames between $1°s^{-1}$ and $50°s^{-1}$. The diagonal and values close to it, as well as the low rotational rates of the outer frame, have been left out to show more details on the remaining options for rotational rates.

The previous maps go to only $50°s^{-1}$ to keep the rotational rates sufficiently low to be able to put larger experiments on the RPM. Below in Figure 6.4, the map is extended to reach $70°s^{-1}$ to cover an even wider range that can be used for smaller experiments. The gain from going beyond $50°s^{-1}$ is very small at the centre of rotation, where the g-level only decreases to the lowest value of $0.0012g$. This is only $10^{-4}g$ better than the results at $50°s^{-1}$. However, the pattern is continued in this extended graph as expected, where the lowest values of the resulting acceleration appear at fast rotations of the outer frame and slow rotations of the inner frame.

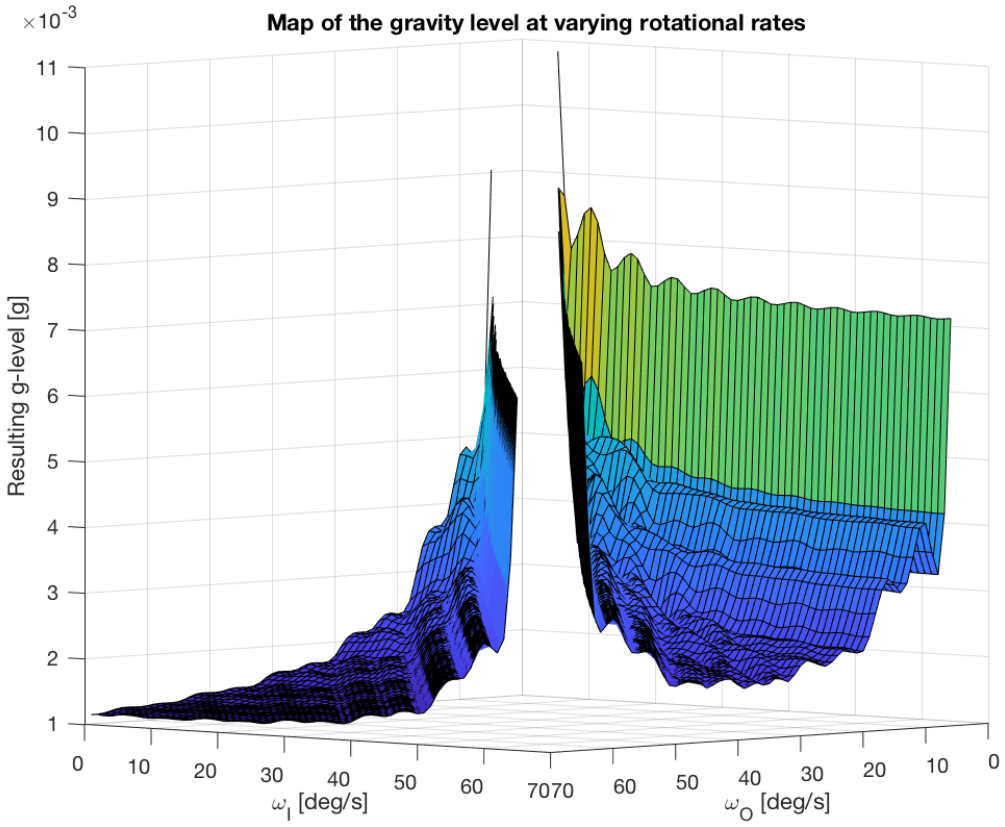

Figure 6.4: Map of the corresponding g-level after 25 min with varying the rotation rate of the frames between $1°s^{-1}$ and $70°s^{-1}$. The diagonal has been left out to show more details on the remaining options for rotational rates.

6.2. Sizing of an Experiment on the RPM

One essential aspect of performing experiments on the RPM is the size of the experiment and determining how large it can be. As the experiment grows bigger and moves further away from the centre of rotation, more significant residual accelerations are introduced during a run. In biological systems, it can be beneficial to put larger and more complex systems on the RPM to reveal phenomena and correlations that do not occur in smaller and simpler systems. Think about going from a single cell to a cluster of cells to an organoid to organs to small animals and finally to a human. Each step towards a full human being introduces more interaction between various subsystems. Some phenomena might happen at the cell level, while others can only be seen when studying a full organ. It can be difficult to isolate biomarkers and set a specific cause for a certain phenomenon as the interaction between elements in the sample is very integrated. A biomarker serves as an objective measure, which characterizes the state of a cell or organism at a given moment. Larger and more complex biological systems can help better understand the said system and its processes. Hence it is useful to know how large an experiment can be while still being exposed to a state of simulated microgravity.

The Yuri RPM only has a test area of 15×15 cm, which is not very big. This means, that practically the furthest distance from the centre of rotation will be in one of the corners around 7.5 cm away in both the x and y-direction. With space for hardware to hold a sample, this distance will be even less. The g-level depends on the position and velocity and is not necessarily limited for all RPMs. To indicate how the resulting g-level differs at varying distances and rotational rates, several options are shown in Table 6.1. The rotational rates vary around $10°s^{-1}$ per step but are selected to avoid the highest g-levels shown earlier that occur at almost similar rotational rates of the two frames. The interesting part is more on how the distance increases the resulting g-level, meaning it is secondary that the frames provide the optimal g-levels. Both the inner frame and the outer frame can be the fast-rotating one. The simulation covers an hour-long run and the g-level is taken as the average of the last 30 s of a run. The values indicate the increase in g from the centre of rotation.

Table 6.1: Gravity level at various rotational rates and distances from the centre of rotation. The values are the increase in g-level compared to the centre of rotation and the distance is taken strictly in the positive x-direction.

Gravity level increase at varying speeds and distances [g]

Rotational rates [$^\circ s^{-1}$]		Distance from centre of rotation [cm]						
		0	0.1	0.5	1	5	10	15
$\omega_O = 9$	$\omega_I = 13$	0.0031	0.0000	0.0000	0.0000	-0.0001	-0.0002	-0.0003
$\omega_O = 23$	$\omega_I = 18$	0.0019	0.0000	0.0000	0.0001	0.0006	0.0014	0.0022
$\omega_O = 31$	$\omega_I = 27$	0.0019	0.0000	0.0001	0.0002	0.0014	0.0032	0.0050
$\omega_O = 39$	$\omega_I = 43$	0.0020	0.0000	-0.0002	-0.0003	0.0011	0.0049	0.0089
$\omega_O = 53$	$\omega_I = 49$	0.0018	0.0001	0.0004	0.0009	0.0054	0.0112	0.0171
$\omega_O = 63$	$\omega_I = 58$	0.0017	0.0001	0.0007	0.0014	0.0079	0.0162	0.0245
$\omega_O = 67$	$\omega_I = 71$	0.0020	-0.0002	-0.0004	-0.0001	0.0080	0.0192	0.0305

Comparing these results to those shown in Figure 3.7, there is some discrepancy. Firstly, the values do not approach 10^{-5} or even $10^{-4}g$ for the lowest levels as the figure indicates they should. One reason could be that the duration of a run is significantly longer in the figure compared to the values in the table. However, there is good accordance between the data and the figure at higher rates and larger distances. The data in the table is limited to maximum $70^\circ s^{-1}$ to show the more useful rotational rates and their corresponding g-levels. At around $60^\circ s^{-1}$ and 10 cm from the centre, the figure show the g-level should be in the order of $10^{-2}g$, which is in aligment with the result of $0.0179g$ as shown in the table. At the same rate but 0.1 cm from the centre, the figure indicates a g-level of 10^{-4}, whereas the result is a magnitude higher in the table. This indicates that there, close to the centre of rotation, is a difference where the results, according to the model, cannot reach the low g-levels indicated by the figure. Some variation can be caused by the exact rotational rates used, whereas the time of a run will only have an effect on the results close to the centre of rotation. This can explain why the model differs close to the centre of rotation but not when moving further away. Extending the simulation of a run to close to three hours, leads to a gravity level in the order of 10^{-4} at a distance of 0.1 cm from the centre. Figure 3.7 can therefore still serve as a simplified overview to indicate the performance of the RPM. To gain more detail, the model would be the next step before starting an experiment.

Interestingly, it can be seen that at low rates, the simulated microgravity level actually decreases at increasing distances. This is due to the angular velocities being so low that the additional accelerations can develop and counteract the orientation of the resulting gravity level. The distances are applied in the positive x-direction, if they were applied in the negative x-direction, the very small additional accelerations would amplify the resulting g-level. For the case of 15 cm at the lowest rotational rates presented, the placement of a sample can cause a difference in the order of $10^{-3}g$, which is significant compared to the specific run, but less significant when it comes to simulating microgravity. This also means that it is not indifferent where the sample is placed, as the resulting g-level can be affected depending on the placement compared to the rotational direction. The case of amplifying or compensating for the g-level is only significant at very small rates. Even more interestingly, is it that both the direction from the centre of rotation and which frame is rotating faster, impacts this variation.

Not only does it matter how far from the centre the sample is, but it also matters where it is placed in relation to the rotational rates of the two frames. Whether the rotation is in one or the other way, and whether the outer frame or inner frame rotates faster, will affect the best placement of the sample. It can therefore be very difficult to give general guidelines on how to place a sample on the RPM. At lower rates, the difference is in the order of $10^{-3}g$, depending on where the sample is placed. This is not severe and the simulated gravity should from this aspect be good enough. As the rotation becomes faster, the additional accelerations also start increasing, and at these rates, it is more important where the sample is placed. At a certain point, the additional accelerations become dominant leading to a

large increase already 5 cm from the centre. This implies that any sample should generally be less than 5 cm from the centre at higher rotational rates above $50°s^{-1}$. Moving below $40°s^{-1}$ the sample size can be extended to 10 cm.

Keeping these interesting aspects in mind can help improve the design of experiments in the future and ensure that larger systems can be properly placed and tested on the RPM. Despite having a larger system rotating at faster rates is generally undesired, it is possible to place a larger system on the RPM if considering and taking advantage of the nature of the rotation and the resulting g-levels will differ depending on the exact location of the sample and not just the distance from the centre of rotation.

6.3. Using the RPM Across the Gravity Spectrum

Additional accelerations will be introduced in the RPM when moving away from the centre of rotation. For some aspects, this might be a bad thing and limits the size of an experiment, but it is possible to take advantage of this and potentially benefit from it as well. With the next steps of human space flight being the commercialisation of LEO and sending humans to the Moon as a stepping stone for going to Mars, there are two gravity levels of particular interest, namely Moon and Mars g-levels besides microgravity. One thing is that we do not have a vast number of different platforms that can provide partial g-levels, the other thing is that these three distinct gravity levels move across the gravity spectrum, allowing us to study the gravity dose response of biological samples and phenomena. In addition to this, it is possible with the RPM to scale, such that potentially hypergravity levels can be achieved in the same run as microgravity. This requires a significantly larger RPM but also allows studying the entire gravity spectrum using one single platform and during one single run. This is valuable as some systems, like organoids, tend to differ from batch to batch. This means that if an organoid is placed on an RPM for a month and afterwards a new one is placed from a batch one month younger, the results might be different, even though all parameters, except the organoid, are kept constant. For this reason, simultaneously running multiple experiments at different g-levels will be a very interesting possibility.

Being able to cover the entire gravity spectrum will allow the RPM to function similarly to a centrifuge in reaching hypergravity levels due to its rotational motion. Having an RPM that simulates multiple gravity levels can be seen as an alternative to having three RPMs running simultaneously, thereby reducing the cost as only one RPM has to be acquired. There can be many benefits to investigating how big an RPM needs to be in order to cover the entire gravity spectrum, hence the sizing of such an RPM is discussed here.

Earlier, it was shown that the current RPM from Yuri can generate a g-level of $0.044g$ when at the corner and rotating the frames at maximum, but still different, velocities. The rates were $120°s^{-1}$ for the outer frame, and $103°s^{-1}$ on the inner frame. It becomes very clear from this, that a significantly larger RPM is required to cover the entire gravity spectrum. The faster the rotation, the smaller the RPM need to be in order to cover the entire gravity spectrum. The results of a run at constant rotation close to $60°s^{-1}$ is shown in Figure 6.5, and in Table 6.2 the results are shown both for an RPM rotating at $60°s^{-1}$ and at $30°s^{-1}$. For the faster option, the RPM needs to be at least 12.5×12.5 m to reach $2.5g$, whereas for the slower option of $30°s^{-1}$ it needs to be 48×48 m. It is very evident that the main impact on the additional accelerations, and thereby the size of the RPM, is the rotational rates. By halving the speed, one needs to quadruple the size to achieve similar g-levels.

One important consideration when using the RPM for simultaneous experiments at different g-levels, is that the resulting acceleration will not be in the z-direction but partially in both the x and y-direction. This is shown in Figure 6.6, where the acceleration in the z-direction remains at $0g$, in the y-direction the sample will experience $0.12g$ and $0.16g$ in the x-direction. This is simulated at the corner position for an RPM of 1×1 m rotating at the previously used rates of $\omega_O = 63°/s$ and $\omega_I = 57°/s$. The placement of a sample should be adjusted accordingly during experiments such that the resulting acceleration will align accordingly to the z-axis of the sample and not of the RPM. It becomes possible to predict the correct angle for placement using the developed model.

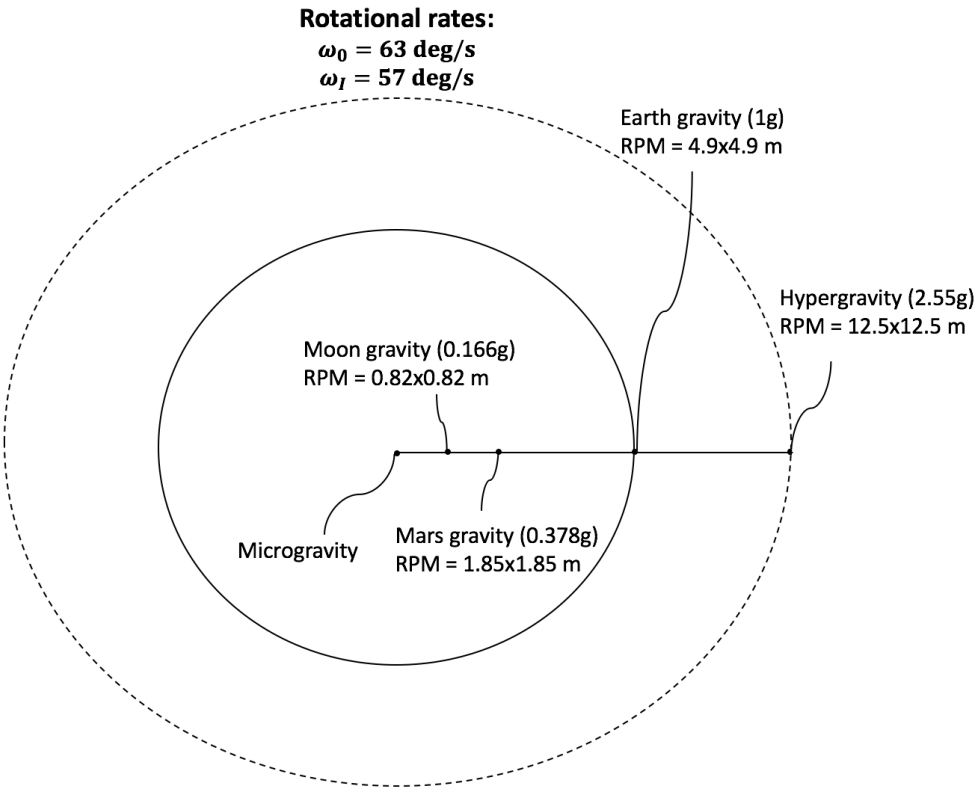

Figure 6.5: RPM sizing across the gravity spectrum, from microgravity to hypergravity during constant rotation at ω_O = $63°\text{s}^{-1}$ and ω_I = $57°\text{s}^{-1}$.

Table 6.2: Sizing of the RPM to support experiments across various gravity levels. The gravity levels are simulated at the corner of the RPM platform.

RPM sizing at $\omega_O = 63°/s, \omega_I = 57°/s$

Gravity level	Moon ($0.166g$)	Mars ($0.378g$)	Earth ($1g$)	Hypergravity ($2.5g$)
RPM size [$m \times m$]	0.82×0.82	1.85×1.85	4.9×4.9	12.5×12.5

RPM sizing at $\omega_O = 33°/s, \omega_I = 27°/s$

Gravity level	Moon ($0.166g$)	Mars ($0.378g$)	Earth ($1g$)	Hypergravity ($2.5g$)
RPM size [$m \times m$]	3.2×3.2	7.2×7.2	20×20	48×48

With a lot of benefits, the sizing of the RPM becomes an obstacle as it needs to be very big to reach hypergravity levels. Although the idea of building an RPM that covers the entire gravity spectrum is engaging, it will be very difficult to argue that it is better to build a really big RPM compared to using a variation of multiple RPMs and one or more centrifuges to cover the entire gravity spectrum. The RPM can be used together with the centrifuge to reach partial gravity but the centrifuge can also go to hypergravity level.

However, it does remain an option to scale an RPM to cover both microgravity and Moon gravity during operation. Before the desktop version of the RPM was developed to fit inside an incubator, three significantly larger RPMs were built for the Dutch Experiment Support Center, ETH-Zürich and the University of Sassari [98]. The RPM can therefore relatively easily be scaled to larger sizes but when incubators are required to control the environment of a sample, it becomes a little more tricky to design the RPM to apply with these added constraints. If the incubators are put on the RPM, the motors still need to reach the required speeds, the wiring for the incubator needs to be accommodated and the samples need to be fastened in the incubator so they do not move around. Incubators are generally

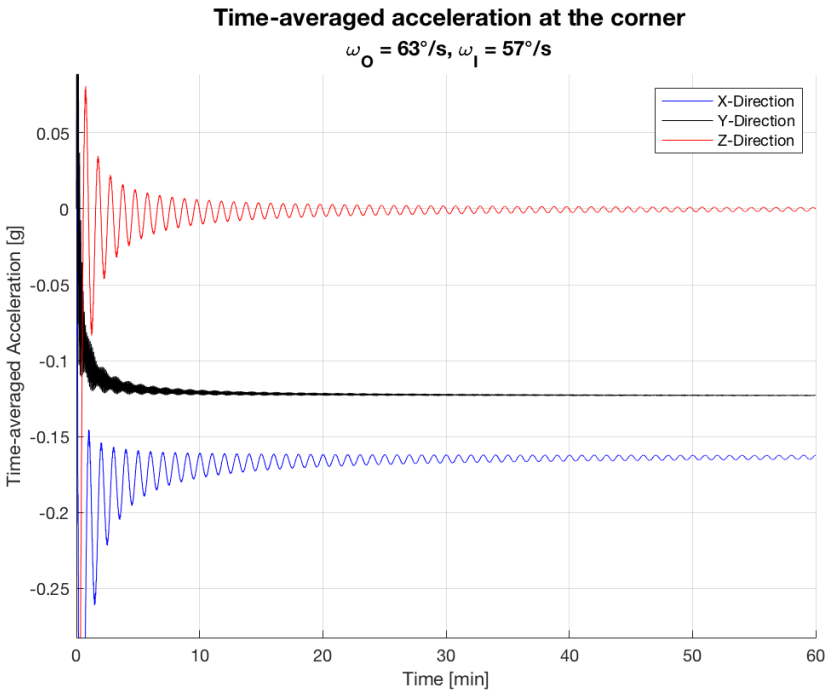

Figure 6.6: Resulting acceleration in each direction during a run on a $1\,\mathrm{m}\times1\,\mathrm{m}$ RPM. The resulting acceleration will be a mix of contributions in the x and y-direction.

quite big and heavy, which is why the desktop version was designed to fit inside an incubator. These issues can be solved, and for a lot of experiments the incubators will not be required, meaning that it can be feasible to build an RPM of 1×1 m to simultaneously simulate microgravity and Moon gravity. As mentioned earlier, it has also been proven possible to have an incubator connected to the inner frame [100].

Assuming a larger RPM of 1×1 m can run at the same rotational rates as the desktop version, it becomes possible to simulate a gravity level of $0.71g$ at the corner position during a run. This is a very fast rotation and will not be suitable for many experiments but it shows that it is possible to cover a large part of the hypogravity regime, whereas the RPM would still need to be even larger to move to hypergravity levels. Building such an RPM will therefore have its main use between microgravity and Moon gravity, while also allowing larger experiments to be performed. This can be in regards to more equipment on the RPM, larger equipment or even a small animal, such as a mouse or rat. These are frequently used as models for spaceflight and can give a better understanding of physiology across the gravity spectrum. It should be noted that placing animals on the RPM for extended periods can cause unnecessary stress, which can affect the measurements, however, they might be able to tell us more about some of the quicker changes happening in altered gravity.

7

Conclusion

The purpose of this thesis was to answer questions regarding the use and limitations of the RPM. Several aspects have been investigated through the developed dynamical model of the system, which was validated by measurements from different sensors and a motion capture system. The paragraph below serves as a small recap of the work in the thesis. More details on the results will follow in the subsequent paragraphs.

First, a literature study was done to explore which platforms were available for gravitational research. The RPM was particularly interesting and a set of research questions was established to outline the work for exploring its use. These questions will be listed and answered at the end of the conclusion. After the literature study, a model was presented to describe the performance of the RPM. This was validated through experimental data from two accelerometers and motion capture recordings. The model developed for this thesis outperformed other attempts in the literature to describe the RPM performance and demonstrated a high level of accuracy when applied to the collected data. Following this, control algorithms were explored, which resulted in the suggestion of building an RPM with three frames to overcome problems of pole bias during experiments. It should also be noted that completely random rotation is not ideal for controlling the RPM. Finally, information on the limitations of the RPM was explored for constant rotational rates and provided guidelines for sizing experiments as well as the RPM itself. These aspects are explored in more detail below.

Given the coordinate systems of the static global frame, the outer frame and the inner frame, the acceleration of a point *P* on the platform in the inner frame of the RPM can be described using Equation 7.1. This takes into account the acceleration of the global frame, which is imposed by gravity, the relative acceleration of the point *P* and the global frame, which can be found by applying the same equations at the rotating outer frame. As well as the final three terms consisting of the centripetal, Coriolis and Euler acceleration terms. When writing the equations, it is important to keep track of the frames and ensure the values are expressed in the correct frames.

$$\begin{aligned} {}_G\boldsymbol{a}_P = \boldsymbol{a}_G &+_G [{}_O\boldsymbol{\omega}_I \times ({}_O\boldsymbol{\omega}_I \times_O \boldsymbol{P}_P)]_O +_G [{}_O\dot{\boldsymbol{\omega}}_I \times_O \boldsymbol{P}_P]_O \\ &+_G \boldsymbol{\omega}_O \times ({}_G\boldsymbol{\omega}_O \times_G \boldsymbol{P}_I) + 2\, {}_G\boldsymbol{\omega}_O \times_G [{}_O\boldsymbol{\omega}_I \times_O \boldsymbol{P}_P]_O +_G \dot{\boldsymbol{\omega}}_O \times_G \boldsymbol{P}_I \end{aligned} \tag{7.1}$$

To determine the trajectory of the gravity vector, which gives an indication of how well gravity is distributed in the sample, one simply needs to track gravity using the rotational matrices and the corresponding angles. This is a very simple task and was shown to be extremely accurate when comparing it to the motion capture recordings.

The analysis showed that the RPM did not always reach the desired rotational rates, which resulted in the drifting of the frames and the trajectory. These are likely to cancel out, as they will most of the time be equal in all directions, but can result in some differences compared to the ideal model. It is possible to correct the model for the drifting but it can take a considerable amount of time to determine the actual rotational rates of the two frames when they differ from the input to the RPM.

This dynamical model describes why the RPM can be said to simulate microgravity from a mathematical viewpoint and makes it possible to predict and improve the performance of the RPM by allowing fast tests of control algorithms and access to evaluate these very easily. It also provides a basis to evaluate which experiments can be put on the RPM and how big they can be.

Furthermore, not all controls performed equally well. Some control algorithms are better than others, but the controls are highly experiment-specific and can be adjusted to certain experimental setups. Only the imagination sets boundaries on which controls can be tested using this code and can help decide whether a certain experiment can be carried out using the RPM before investing in one. The most important point is that rotating the two frames randomly is actually not the most optimal way of controlling them despite the name, whereas also rotating the two frames at the same, or almost the same, rates will be suboptimal.

Evaluating various control algorithms showed a clear problem of pole bias. This is due to the nature of the rotation of the two frames, which forces the gravity vector to point in one of two directions every time the outer frame reaches the vertical position. To overcome this problem, it was investigated whether a simple mathematical expression could be used to avoid pole bias by using a superposition of sinusoidal waves. This proved not to work optimally. Instead, the use of an RPM with three frames was suggested. Adding the third frame allows the trajectory to be uniformly distributed and avoids pole bias. This will be especially useful in 3-D cell cultures, where the highest quality of simulated microgravity is desired, and gravity should be uniformly distributed in all directions of the cell. The three frames were evaluated similarly to the two frames, and the expressions for the acceleration of the three frames are shown in Equation 7.2 to Equation 7.4.

$$
\begin{aligned}
{}_G\boldsymbol{a}_P = &\begin{bmatrix} 0 \\ 0 \\ -g \end{bmatrix} + [{}_O\boldsymbol{a}_P]_G + {}_G\boldsymbol{\omega}_O \times ({}_G\boldsymbol{\omega}_O \times {}_G\boldsymbol{P}_I) + 2\,{}_G\boldsymbol{\omega}_O \times ({}_M\boldsymbol{\omega}_P \times {}_M\boldsymbol{P}_P + {}_O\boldsymbol{\omega}_P \times {}_O\boldsymbol{P}_P) \\
&+ {}_G\dot{\boldsymbol{\omega}}_O \times {}_G\boldsymbol{P}_I
\end{aligned} \tag{7.2}
$$

$$
\begin{aligned}
[{}_O\boldsymbol{a}_P]_G = &[{}_M\boldsymbol{a}_P]_G + {}_G[{}_O\boldsymbol{\omega}_M \times ({}_O\boldsymbol{\omega}_M \times {}_O\boldsymbol{P}_I)]_O + {}_G[2\,{}_O\boldsymbol{\omega}_M \times ({}_M\boldsymbol{\omega}_P \times {}_M\boldsymbol{P}_P)]_O \\
&+ {}_G[{}_O\dot{\boldsymbol{\omega}}_M \times {}_O\boldsymbol{P}_I]_O
\end{aligned} \tag{7.3}
$$

$$
[{}_M\boldsymbol{a}_P]_G = {}_G[{}_M\boldsymbol{\omega}_I \times ({}_M\boldsymbol{\omega}_I \times {}_M\boldsymbol{P}_I)]_M + {}_G[{}_M\dot{\boldsymbol{\omega}}_I \times {}_M\boldsymbol{P}_I]_M \tag{7.4}
$$

Not only did the distance from the centre to the sample matter for the resulting g-level but also the exact placement in relation to the rotational direction and rates of the two frames would affect the experienced g-level. This makes it possible to manipulate the acceleration in ways that can improve the experimental settings and allow for a larger test area. This is very case-dependent and would have to be evaluated on a case-by-case basis if it will even be relevant for an experiment.

When it comes to sizing, a general rule of thumb is that faster than $50°\text{s}^{-1}$ requires the sample to be less than 5 cm from the centre of rotation. When moving below $40°\text{s}^{-1}$, it is possible to use a larger sample of approximately 10 cm without completely compromising the simulated microgravity. However, by placing it according to the rotation direction and rates, it might be possible to significantly increase the experimental dimensions. This is not the general case and should be done very carefully, but ideally, it should be avoided. This observation is in accordance with Figure 3.7, which indicates that at an angular velocity of $57°\text{s}^{-1}$, the g-level is a magnitude larger at a distance of less than 3 cm from the centre of rotation compared to at the centre itself.

Furthermore, it was shown that covering the entire gravity spectrum simultaneously during a single run on the RPM required the RPM to be 12.5 m$\times 12.5$ m. Having such a large platform would make it possible to simulate microgravity at the centre and hypergravity of $2.5g$ at the corner position. This is achievable with a rotational rate of the frames close to $60°\text{s}^{-1}$. If the rotation was halved, the dimensions of the RPM had to be quadrupled to achieve the same g-levels.

There are also other ways to reach hypogravity levels, such as by placing the RPM inside a centrifuge or having specific controls that ensure the gravity vector points more towards a certain direction, which

over time results in the desired partial g-level.

The above information outlines the most important conclusions of this thesis and can be used to answer the research questions below.

- **How can the rotational rates for predicting the resulting g-level be modelled?**
  - Setting up the RPM as a dynamical system and making a kinematic model of the system results in the description of the acceleration as shown in Equation 7.1. The rotational rates, the placement of a sample inside the RPM and the change in angular velocities will impact the resulting g-level as seen in the equation. It shows the complete description of the acceleration in the system.
- **What are the best combinations of rotational rates for an RPM to simulate microgravity using constant velocities?**
  - The best rates were shown to be with high angular velocity of the outer frame while the inner frame should rotate at low rates. The best options for simulating very low g-levels were ω_O = $50°s^{-1}$ and ω_I = 4 to $7°s^{-1}$. Increasing the rotational rates to exceed $50°s^{-1}$ proved to lower the resulting g-level further but only very limited.
- **How do the combinations of rotational rates relate to g-level?**
  - The specific combination of rotational rates of the outer and inner frame greatly affects the resulting g-level. When they are rotating at the same or even close to the same rates, the g-level is heavily increased resulting in suboptimal performance of the RPM. Rotating the outer frame below $5°s^{-1}$ also showed to increase the g-level irrespective of the rotation of the inner frame. There are therefore certain combinations that should be avoided when using the RPM, as those mentioned above.
- **To what extent can the g-level be improved using alternative control algorithms?**
  - Switching from constant rotational rates to alternative control algorithms will rarely lead to improved g-levels. Rather, the alternative controls can be used to improve the quality of the simulated microgravity by distributing gravity more uniformly in all directions but only advanced and carefully developed controls can lead to a reduction of the g-level compared to constant rotation.
- **How would the model change when considering Moon and Mars gravity levels?**
  - The model is written as a general expression and is not limited by any particular gravity levels. The acceleration is modelled based on the angular velocities, any change in these and the location inside the RPM and will remain applicable irrespective of the g-level.
- **To what extent are the optimal combinations useful in a real experiment on the RPM?**
  - The optimal combinations of rotational rates of ω_O = $50°s^{-1}$ and ω_I = 4 to $7°s^{-1}$ will rarely be used in real experiments with the two-framed RPM. This is due to the pole bias, which is created every time the outer frame is in the vertical position. As it rotates faster, this will occur more often and is an undesired effect of achieving the lowest possible g-level. However, adding a third frame to the RPM to overcome pole bias makes it possible to use these rotational rates to generate low g-levels through new control algorithms. One example is to have the third frame rotate at constant rotational rates, while the two other frames randomly select between certain sets of rotational rates that result in the lowest g-levels.
- **What effect does moving away from the centre of rotation have on the residual g-level?**
  - Moving away from the centre introduces additional accelerations to the system. This is one of the reasons, it has been difficult to use the RPM, as the effects of moving away from the centre have not fully been described. These additional accelerations will change the simulated g-level and can invalidate any experiment. The faster the rotation or the greater

the distance to the centre, the higher will these additional accelerations be.

- **At what point will the residual forces be so significant that microgravity is no longer achieved?**
  - This depends on the exact rotational rates. However, a general rule of thumb will be that rotating above $50°s^{-1}$ will restrain an experiment to be smaller than 5 cm, whereas if the rotation is slower than $40°s^{-1}$, the sample can be up to 10 cm in total. The exact g-level depends on the precise placement and rotational rates of the RPM.
- **How would the RPM be scaled if multiple g-levels should be simulated during the same?**
  - Increasing the distance to the centre will increase the acceleration levels. At certain distances other interesting g-levels can be achieved, which can be of use to study gravity-dose responses. Different rotational rates require different sizes of the RPM to reach certain g-levels. To cover the entire gravity spectrum at ω_O = $63°s^{-1}$ and ω_I = $57°s^{-1}$, the RPM need to be 12.5 m $\times$ 12.5 m. To reach $1g$, it needs to be 5 m $times$ 5 m. For Mars gravity of $0.378g$, it would need to be 1.85 m $times$ 1.85 m. Finally, to reach lunar g-level, the RPM would need to be 0.82 m $\times$ 0.82 m.

The RPM is a very versatile and relatively unexplored platform for gravitational research. While not being able to make spaceflights redundant, it holds the potential to significantly increase studies on the gravitational response of a large variety of systems. This is a more accessible and cheaper option compared to spaceflight and will allow a significant throughput in gaining a better understanding of age-related diseases on Earth and secure astronauts' health on missions to the Moon or Mars.

Discussion

One of the sensors had an accuracy of $10^{-2}g$, whereas many of the results were in the order of $10^{-3}g$. For future work to be done on the model, it can be suitable to use more precise sensors that can differentiate the small differences during a run. The accordance between the measurements and modelled accelerations for each individual direction was very high. The phase and magnitude were similar but there were small differences in the order of $10^{-3}g$, which could be spotted in the data. Overall, the instantaneous g-level would be a constant of $1g$ split across the x, y and z-directions. This was the case for the ideal model in the centre of rotation, whereas the sensors had some variation to gravity in their measurements likely due to either the accuracy of the sensors or their exact location. Additional accelerations could occur for the sensors depending on their exact location and cause some variation from $1g$, however, that alone will not be enough to explain the variation. Therefore it is likely the variation is also caused partly due to the accuracy of the sensors. Having an accuracy of $10^{-2}g$ seems reasonable but when considering the resulting g-level can go to $10^{-3}g$, these very small inaccuracies can be spotted in the measurements. Together with this, the sensor also seemed to have a bias that caused it to have higher g-levels at low rotational rates, whereas the g-level should have been low. This would be a systematic error of the sensor and there was no good way to correct this despite the sensor being calibrated before each run. The sensor managed to improve its measurements at faster rotations when compared to the measurements of the other sensor and the model.

The developed model does show good accordance with the second sensor, and especially the trajectory is modelled very accurately to the recordings. This supports the belief that the theoretically accurate description of the resulting acceleration is also true in practice. This model therefore gives a good basis to evaluate the performance of the RPM based on the rotational rates and the placement of a sample. It can be used to optimise the design of experiments on the RPM and evaluate whether some experiments are worth carrying out with an RPM or if a different platform should be used. This is quite a big step in terms of making the general scientist aware of the limitations and optimal usage of the RPM. So far, there has existed no detailed model and no guide to understanding the RPM and how it can be said to simulate microgravity. This has resulted in several papers that have used the RPM suboptimally through completely random rotation [11], [75], [110]. A closer look will likely reveal even more papers that do not have the required knowledge and understanding of the RPM to optimally use it for their experiments. This should not be seen as a critique towards the previous use of the RPM but rather

as the lack of knowledge, this thesis sets out to explore and fill. Using this newly gained knowledge can therefore benefit the future use of the RPM and advance new experiments for this platform, and generally make hypogravity more accessible in research.

One striking finding is the occurrence of pole bias, which most control algorithms with two frames show. This is a very disturbing feature about the two-framed RPM when considering gravity should ideally be uniformly distributed in all directions. The cause is very simple and it is therefore possible to control the algorithms to not generate poles by not having the outer frame reach the vertical position. There are no real limitations to developing controls for the RPM but some will perform better than others and can be developed for very specific experiments. Extending the future use of the RPM to involve more 3-D cell cultures such as organoids or spheroids requires overcoming pole bias for the best results. The simulation should be as accurate to real microgravity as possible, and since microgravity is uniform, the gravity vector orientation should ideally also be uniformly distributed. This is very difficult with only two frames while also achieving low gravity levels, which indicates that more advanced algorithms are needed. Instead of looking at the software, it is suggested to add a third frame to the RPM, which removes the natural cause of pole bias as the position of the former outer frame no longer dictates the gravity vector to point in two specific directions more than others. The three frames showed overwhelming results in distributing the gravity vector uniformly and were therefore seen as a better solution to overcome pole bias than developing very advanced control sequences of the two frames.

Adding a third frame limits parts of the use of the RPM as it can no longer be inside a standard-sized incubator due to the increase in its physical size. Alternatively, it is possible to make the platform larger so it can be used for larger experiments or across two different g-levels. The incubator can also be added as an integral part of the inner frame, such that the cell environment can still be controlled which has been done in a two-framed RPM [100]. This will come with some other considerations to the engineering aspects of the RPM, such that it can support the weight of the incubator and that the samples are fastened inside the incubator. There are many ways to overcome exceeding the dimensions of an incubator through engineering work but it is only possible to overcome pole bias through the development of very advanced controls. At least when the gravity vector should be uniformly distributed in all directions while also achieving low g-levels. Modifying the RPM to overcome pole bias results in increased use, especially when it comes to 3-D cell cultures. This means that in the future the RPM can potentially contribute more to cell-based therapy and experiments involving a 3-D structure can be exposed to a more accurate simulation of microgravity.

The model of the three frames follows the same principles as the two frames. In this thesis, the idea is presented alongside one suggestion on how to control the three frames for the best result. This is not necessarily the absolute best possible way to control the three frames and there can be a significant amount of work at a later point to further optimise the three-framed RPM. It is, however, a suggestion that distributes the gravity vector uniformly and results in a low g-level. For future work, an optimisation can be made to investigate which parameters and speeds the three frames perform better at. More advanced controls can also be included in an analysis to show the performance of the three frames at a large variety of controls. With an extra frame, there are even more possibilities than for the two frames as basically any type of control for any of the three frames is available. Therefore much work can be dedicated to optimise the RPM further.

Microgravity also holds the interesting aspect of accelerating ageing processes, which can be utilised to more quickly develop drugs and study age-related diseases at a higher pace. It is interesting if simulated microgravity holds the same attributes, which should be investigated in the future to further expand the use of the RPM. To prove the RPM can be used for more than just basic cell development, studies will need to show and compare to real space flight data. This can be both studies of more complex systems such as organoids, but might also just be limited to physically larger systems such as filtration of e.g. water.

Microgravity is a captivating environment due to its distinctive characteristics, including the absence of convection, sedimentation, and buoyancy. These unique features open up new possibilities within physical and chemical processes. Notably, the crystallization of proteins, a crucial aspect of drug development, experiences significant enhancement in microgravity conditions. In the microgravity en-

vironment of space, the crystallization process becomes more refined, allowing for the growth of larger and higher-quality crystals. This advancement holds great potential for improving drug development.

Recognizing the advantages of microgravity crystallization, there is an opportunity to leverage some of these aspects on the Earth's surface through the use of the RPM. While simulating microgravity on the RPM may not precisely replicate the conditions of true microgravity, it represents a substantial leap forward. If it proves possible to enhance the crystallization process on Earth, it could revolutionize the way we currently develop drugs. Although not a perfect substitute for real microgravity, the RPM offers a promising avenue to explore and refine Earth-based methodologies. This initiative extends beyond the realm of space flight and encompasses a broad spectrum of scientific endeavours. By harnessing the capabilities of the RPM, it is possible to catalyze significant scientific advances that transcend traditional boundaries and contribute to the collective progress of diverse scientific disciplines. Exactly for this reason has it been interesting to model the RPM and provide guidelines for its use, which can help expand its presence across disciplines allowing microgravity to become more accessible on Earth.

Not only in microgravity but also at other hypogravity levels can the RPM serve as a great platform for new discoveries. One of the difficult aspects of sending humans to Mars is to predict how human physiology reacts to this new gravity level. When humans went to the Moon, it was for example very difficult to get back up after a fall. So very little things can become extremely important. This can be very difficult to predict but with the RPM we at least have a platform where we can simulate these hypogravity levels and evaluate their consequences on human physiology. Only the simplest methods of achieving partial g-levels were presented here, so in the future, more work can be put into generating more complex and more true simulations of partial gravity levels. By putting more effort into it, the algorithm presented in this thesis can be significantly improved. However, the basis for this development remains the same, future algorithms need to manipulate the gravity vector such that it spends more time in certain directions compared to others to simulate e.g. Moon or Mars gravity.

Overall, the RPM is a very powerful platform within gravitational research but only a limited understanding of it exists. This might be a hindrance to some scientists but this thesis has outlined some guidelines and important considerations to the use of the RPM and the sizing of experiments to put on it. Using it suboptimally as has been seen in past experiments might have resulted in suboptimal results, whereas now the use can be improved more easily for each experiment. This is the first step to utilising the full potential of the RPM and contributing towards an improved understanding of gravity and its effects on life, physiology and technologies. Whether it is the development of SANS in astronauts, the development of new drugs in an accelerated ageing environment or the validation of technologies for future human space exploration, the RPM can potentially be used for significantly more than it currently is, which can improve life, not just on Earth but all the way to a future research base on Mars.

References

[1] T. H. Mader, C. R. Gibson, A. F. Pass, *et al.*, "Optic disc edema, globe flattening, choroidal folds, and hyperopic shifts observed in astronauts after long-duration space flight," *Ophthalmology*, vol. 118, pp. 2058–2069, Nov. 2011. DOI: 10.1016/j.ophtha.2011.06.021.

[2] Z. S. Patel, T. J. Brunstetter, W. J. Tarver, *et al.*, "Red risks for a journey to the red planet: The highest priority human health risks for a mission to mars," *npj Microgravity*, vol. 6, no. 1, 2020. DOI: 10.1038/S41526-020-00124-6.

[3] K. E. Hupfeld, H. R. McGregor, J. K. Lee, *et al.*, "The impact of 6 and 12 months in space on human brain structure and intracranial fluid shifts," *Cerebral Cortex Communications*, vol. 1, no. 1, Jun. 2020. DOI: 10.1093/texcom/tgaa023.

[4] A. G. Lee, T. H. Mader, C. R. Gibson, *et al.*, "Spaceflight associated neuro-ocular syndrome (sans) and the neuro-ophthalmologic effects of microgravity: A review and an update," *npj Microgravity*, vol. 6, 1 2020. DOI: 10.1038/s41526-020-0097-9.

[5] A. Van Ombergen, S. Jillings, B. Jeurissen, *et al.*, "Brain ventricular volume changes induced by long-duration spaceflight," *Proceedings of the National Academy of Sciences of the United States of America*, vol. 116, no. 21, pp. 10 531–10 536, 2019. DOI: 10.1073/pnas.1820354116.

[6] J. Ong, A. Tavakkoli, N. Zaman, *et al.*, "Terrestrial health applications of visual assessment technology and machine learning in spaceflight associated neuro-ocular syndrome," *npj Microgravity*, vol. 8, no. 1, 2022. DOI: 10.1038/s41526-022-00222-7.

[7] C. Krittanawong, N. K. Singh, R. A. Scheuring, *et al.*, "Human health during space travel: State-of-the-art review," *Cells*, vol. 12, 1 2023. DOI: 10.3390/cells12010040.

[8] M. Capri, M. Conte, E. Ciurca, *et al.*, "Long-term human spaceflight and inflammaging: Does it promote aging?" *Ageing Research Reviews*, vol. 87, 2023. DOI: 10.1016/j.arr.2023.101909.

[9] L. A. Low and M. A. Giulianotti, "Tissue chips in space: Modeling human diseases in microgravity," *Pharmaceutical Research*, vol. 37, 1 2020. DOI: 10.1007/s11095-019-2742-0.

[10] M. Wehland, P. Steinwerth, G. Aleshcheva, *et al.*, "Tissue engineering of cartilage using a random positioning machine," *International Journal of Molecular Sciences*, vol. 21, no. 24, 2020. DOI: 10.3390/ijms21249596.

[11] V. Mann, D. Grimm, T. J. Corydon, *et al.*, "Changes in human foetal osteoblasts exposed to the random positioning machine and bone construct tissue engineering," *International Journal of Molecular Sciences*, vol. 20, 6 2019. DOI: 10.3390/ijms20061357.

[12] K. Costello, P. Archila, and D. Brady, "Annual highlights of results from the international space station october 1, 2021 – september 30, 2022," National Aeronautics and Space Administration, 2022.

[13] F. Ferranti, M. D. Bianco, and C. Pacelli, "Advantages and limitations of current microgravity platforms for space biology research," *Applied Sciences (Switzerland)*, vol. 11, 1 2021. DOI: 10.3390/app11010068.

[14] NASA. "Space station research explorer." (2021), [Online]. Available: https://www.nasa.gov/mission_pages/station/research/experiments/explorer/search.html?#q=&i=&p=&c=&g=Facility&s=&a= (visited on 06/13/2023).

[15] X. W. Mao, S. Byrum, N. C. Nishiyama, *et al.*, "Impact of spaceflight and artificial gravity on the mouse retina: Biochemical and proteomic analysis," *International Journal of Molecular Sciences*, vol. 19, 9 2018. DOI: 10.3390/ijms19092546.

[16] D. Shiba, H. Mizuno, A. Yumoto, *et al.*, "Development of new experimental platform 'mars'-multiple artificial-gravity research system-to elucidate the impacts of micro/partial gravity on mice," *Scientific Reports*, vol. 7, 1 2017. DOI: 10.1038/s41598-017-10998-4.

[17] A. J. Ricco, J. W. Hines, M. Piccini, *et al.*, "Autonomous genetic analysis system to study space effects on microorganisms: Results from orbit," 2007. DOI: 10.1109/SENSOR.2007.4300065.

[18] A. Kanapskyte, E. M. Hawkins, L. C. Liddell, S. R. Bhardwaj, D. Gentry, and S. R. S. Maria, “Space biology research and biosensor technologies: Past, present, and future,” *Biosensors*, vol. 11, 2 2021. DOI: 10.3390/BIOS11020038.

[19] A. J. Ricco, S. R. Maria, R. P. Hanel, and S. Bhattacharya, “Biosentinel: A 6u nanosatellite for deep-space biological science,” *IEEE Aerospace and Electronic Systems Magazine*, vol. 35, 3 2020. DOI: 10.1109/MAES.2019.2953760.

[20] E. Messerschmid and R. Bertrand, *Space Stations*. Springer Berlin Heidelberg, 1999. DOI: 10.1007/978-3-662-03974-8.

[21] A. Andreev-Andrievskiy, A. Popova, R. Boyle, *et al.*, “Mice in bion-m 1 space mission: Training and selection,” *PLoS ONE*, vol. 9, 8 2014. DOI: 10.1371/journal.pone.0104830.

[22] G. Ruyters and U. Friedrich, “From the bremen drop tower to the international space station iss - ways to weightlessness in the german space life sciences program,” *Signal Transduction*, vol. 6, 6 2006. DOI: 10.1002/sita.200600108.

[23] NASA. “Commercial suborbital flight providers.” (2022), [Online]. Available: https://www.nasa.gov/directorates/spacetech/flightopportunities/flightproviders (visited on 11/09/2022).

[24] Blue Origin, “New shepard payload users guide,” Revision F, 2019.

[25] S. H. Collicott and A. Alexeenko, “Propulsion testing in commercial re-usable sub-orbital rockets,” in *AIAA Propulsion and Energy 2019 Forum*. 2019. DOI: 10.2514/6.2019-4354.

[26] E. B. Wagner, “Research flights on blue origin’s new shepard,” *Gravitational and Space Research*, vol. 9, no. 1, pp. 62–67, 2021. DOI: doi:10.2478/gsr-2021-0005.

[27] B. Califar, A. Zupanska, J. A. Callaham, *et al.*, “Shared metabolic remodeling processes characterize the transcriptome of arabidopsis thaliana within various suborbital flight environments,” *Gravitational and Space Research*, vol. 9, 1 2021. DOI: 10.2478/gsr-2021-0002.

[28] K. J. Stober, M. R. M. Apodaca, and D. Wood, “Paraffin & beeswax spaceflight experiments for improved understanding of centrifugal casting,” vol. 2022-March, 2022. DOI: 10.1109/AERO53065.2022.9843648.

[29] G. Seibert, “The history of sounding rockets and their contribution to european space research,” *European Space Agency - History Study Reports ESA HSR*, 38 2006.

[30] NASA, “Nasa sounding rockets annual report 2022,” 2022.

[31] R. H. Burth, P. G. Cathell, D. B. Edwards, *et al.*, “Nasa sounding rockets user handbook,” 2023.

[32] S. Westerlund, M. Abrahamsson, G. Florin, and C. Lockowandt, “Esrange space center – a european rocket and balloon launch and operation site north of the arctic circle,” 2018. DOI: 10.2514/6.2018-2701.

[33] JAXA. “SS-520 Sounding Rockets.” (2008), [Online]. Available: https://www.isas.jaxa.jp/e/enterp/rockets/sounding/ss520.shtml (visited on 06/15/2023).

[34] NASA. “NASA Sounding Rocket Science.” (2023), [Online]. Available: https://rscience.gsfc.nasa.gov/srrov.html (visited on 06/13/2023).

[35] ESA, “Esa user guide to low gravity platforms,” 2014.

[36] T. F. Kraft, J. J. V. Loon, and J. Z. Kiss, “Plastid position in arabidopsis columella cells is similar in microgravity and on a random-positioning machine,” *Planta*, vol. 211, 3 2000. DOI: 10.1007/s004250000302.

[37] R. Kirchhartz, M. HÃ¶rschgen-Eggers, and W. Jung, “Sounding rockets are unique experimental platforms,” 2018.

[38] V. Pletser and Y. Kumei, “Parabolic flights,” in *Generation and Applications of Extra-Terrestrial Environments on Earth*, D. A. Beysens and J. J. W. A. van Loon, Eds., Ålborg: River Publishers, 2015, ch. 7, pp. 61–73.

[39] V. Pletser, “Short duration microgravity experiments in physical and life sciences during parabolic flights: The first 30 esa campaigns,” *Acta Astronautica*, vol. 55, no. 10, pp. 829–854, 2004. DOI: https://doi.org/10.1016/j.actaastro.2004.04.006.

[40] V. Pletser, “European aircraft parabolic flights for microgravity research, applications and exploration: A review,” *REACH*, vol. 1, 2016. DOI: 10.1016/j.reach.2016.05.002.

[41] P. Niksirat, A. Daca, and K. Skonieczny, “The effects of reduced-gravity on planetary rover mobility,” *International Journal of Robotics Research*, vol. 39, 7 2020. DOI: 10.1177/0278364920913945.

[42] J. C. G. Petersen, A. R. Hargens, and L. G. Petersen, “Parabolic flight,” in *Handbook of Bioastronautics*, L. R. Young and J. P. Sutton, Eds. Cham, Switzerland: Springer Nature Switzerland AG, 2021, pp. 489–498. DOI: 10.1007/978-3-319-10152-1_62-1.

[43] Diamond Air Service. “Micro-Gravity Experiment.” (), [Online]. Available: https://www.mhi.com/group/das/business/gravity (visited on 06/22/2023).

[44] S. Rouquette, “30 years of cnes parabolic flights for the benefit of the scientific community,” *Comptes Rendus. Mécanique*, vol. 351, 2023. DOI: 10.5802/crmeca.144.

[45] P. von Kampen, U. Kaczmarczik, and H. J. Rath, “The new drop tower catapult system,” *Acta Astronautica*, vol. 59, 1-5 2006. DOI: 10.1016/j.actaastro.2006.02.041.

[46] NASA Glenn Research Center, “Zero gravity research facility user’s guide,” 2018.

[47] C. Lämmerzahl and T. Steinberg, “Drop towers,” in *Generation and Applications of Extra-Terrestrial Environments on Earth*, D. A. Beysens and J. J. W. A. van Loon, Eds., Ålborg: River Publishers, 2015, ch. 6, pp. 45–60.

[48] ZARM. “How does the GraviTower Bremen Pro work?” (), [Online]. Available: https://www.zarm.uni-bremen.de/en/drop-tower/general-information/how-does-the-gravitower-bremen-pro-work.html (visited on 06/21/2023).

[49] T. Könemann, U. Kaczmarczik, A. Gierse, *et al.*, “Concept for a next-generation drop tower system,” *Advances in Space Research*, vol. 55, 6 2015. DOI: 10.1016/j.asr.2014.12.028.

[50] C. Lotz, Y. Wessarges, J. Hermsdorf, W. Ertmer, and L. Overmeyer, “Novel active driven drop tower facility for microgravity experiments investigating production technologies on the example of substrate-free additive manufacturing,” *Advances in Space Research*, vol. 61, 8 2018. DOI: 10.1016/j.asr.2018.01.010.

[51] C. Lotz, T. Froböse, A. Wanner, L. Overmeyer, and W. Ertmer, “Einstein-elevator: A new facility for research from μg to 5g,” *Gravitational and Space Research*, vol. 5, pp. 11–27, 2 Dec. 2017. DOI: 10.2478/gsr-2017-0007.

[52] NASA Glenn Research Center. “ElectroMotive Drop Tower Initiative.” (2022), [Online]. Available: https://www1.grc.nasa.gov/facilities/emdt/ (visited on 06/23/2023).

[53] Leibniz University Hannover. “Einstein-Elevator.” (2023), [Online]. Available: https://www.hitec.uni-hannover.de/en/large-scale-equipment/einstein-elevator (visited on 06/23/2023).

[54] NASA Glenn Research Center. “2.2 second drop tower.” (2022), [Online]. Available: https://www1.grc.nasa.gov/facilities/drop/ (visited on 06/23/2023).

[55] A. Wollman and M. Weislogel, “New investigations in capillary fluidics using a drop tower,” *Experiments in Fluids*, vol. 54, 4 2013. DOI: 10.1007/s00348-013-1499-1.

[56] T. Steinberg, “Reduced gravity testing and research capabilities at queensland university of technology’s new 2.0 second drop tower,” 2007. DOI: 10.4028/www.scientific.net/amr.32.21.

[57] Hokkaido Aerospace Science and Technology Incubation Center. “Space Environment Utilization.” (2020), [Online]. Available: https://www.hastic.jp/development/space_environment (visited on 06/22/2023).

[58] X. Zhang, L. Yuan, W. Wu, L. Tian, and K. Yao, “Some key technics of drop tower experiment device of national microgravity laboratory (china) (nmlc),” *Science in China, Series E: Technological Sciences*, vol. 48, 3 2005. DOI: 10.1360/102004-21.

[59] T. Y. Liu, Q. P. Wu, B. Q. Sun, and F. T. Han, “Microgravity level measurement of the beijing drop tower using a sensitive accelerometer,” *Scientific Reports*, vol. 6, 2016. DOI: 10.1038/srep31632.

[60] V. V. Nikhil, A. Nair, P. Niketh, A. Kumar, and M. Muruganandam, “The 2.5 s microgravity drop tower at national centre for combustion research and development (nccrd), indian institute of technology madras,” *Microgravity Science and Technology*, vol. 30, 5 2018. DOI: 10.1007/s12217-018-9639-0.

[61] Gravitilab Aerospace Services. “Technology.” (2023), [Online]. Available: https://gravitilab.space/technology/ (visited on 06/23/2023).

[62] S. Kedarisetty and J. G. Manathara, “Acceleration control of a multi-rotor uav towards achieving microgravity,” *Aerospace Systems*, vol. 2, 2 2019. DOI: 10.1007/s42401-019-00031-z.

[63] A. R. Hargens and L. Vico, “Long-duration bed rest as an analog to microgravity,” *Journal of Applied Physiology*, vol. 120, 8 2016. DOI: 10.1152/japplphysiol.00935.2015.

[64] V. Koppelmans, J. J. Bloomberg, A. P. Mulavara, and R. D. Seidler, “Brain structural plasticity with spaceflight,” *npj Microgravity*, vol. 2, 1 2016. DOI: 10.1038/s41526-016-0001-9.

[65] T. F. Tsai and H. I. Maibach, “How irritant is water? an overview,” *Contact Dermatitis*, vol. 41, 6 1999. DOI: 10.1111/j.1600-0536.1999.tb06990.x.

[66] N. M. Navasiolava, M. A. Custaud, E. S. Tomilovskaya, *et al.*, “Long-term dry immersion: Review and prospects,” *European Journal of Applied Physiology*, vol. 111, 7 2011. DOI: 10.1007/s00421-010-1750-x.

[67] M. Pandiarajan and A. R. Hargens, “Ground-Based Analogs for Human Spaceflight,” *Frontiers in Physiology*, vol. 11, 2020. DOI: 10.3389/fphys.2020.00716.

[68] E. Tomilovskaya, T. Shigueva, D. Sayenko, I. Rukavishnikov, and I. Kozlovskaya, “Dry immersion as a ground-based model of microgravity physiological effects,” *Frontiers in Physiology*, vol. 10, MAR 2019. DOI: 10.3389/fphys.2019.00284.

[69] L. Ploutz-Snyder, “Evaluating countermeasures in spaceflight analogs,” *Journal of Applied Physiology*, vol. 120, 8 2016. DOI: 10.1152/japplphysiol.00860.2015.

[70] S. P. John and K. H. Hasenstein, “Effects of mechanostimulation on gravitropism and signal persistence in flax roots,” *Plant Signaling and Behavior*, vol. 6, 9 2011. DOI: 10.4161/psb.6.9.16601.

[71] R. Hemmersbach, M. V. D. Wiesche, and D. Seibt, “Ground-based experimental platforms in gravitational biology and human physiology,” *Signal Transduction*, vol. 6, 6 2006. DOI: 10.1002/sita.200600105.

[72] K. H. Hasenstein and J. J. van Loon, “Clinostats and other rotating systems-design, function, and limitations,” in *Generation and Applications of Extra-Terrestrial Environments on Earth*, D. A. Beysens and J. J. W. A. van Loon, Eds., Ålborg: River Publishers, 2015, ch. 14, pp. 147–156.

[73] S. Brungs, M. Egli, S. L. Wuest, *et al.*, “Facilities for simulation of microgravity in the esa ground-based facility programme,” *Microgravity Science and Technology*, vol. 28, 3 2016. DOI: 10.1007/s12217-015-9471-8.

[74] T. Hoson, S. Kamisaka, Y. Masuda, M. Yamashita, and B. Buchen, “Evaluation of the three-dimensional clinostat as a simulator of weightlessness,” vol. 203, 1997. DOI: 10.1007/pl00008108.

[75] L. Krause, M. Braun, J. Hauslage, and R. Hemmersbach, “Analysis of statoliths displacement in chara rhizoids for validating the microgravity-simulation quality of clinorotation modes,” *Microgravity Science and Technology*, vol. 30, 3 2018. DOI: 10.1007/s12217-017-9580-7.

[76] R. Herranz, R. Anken, J. Boonstra, *et al.*, “Ground-based facilities for simulation of microgravity: Organism-specific recommendations for their use, and recommended terminology,” *Astrobiology*, vol. 13, 1 2013. DOI: 10.1089/ast.2012.0876.

[77] D. M. Klaus, “Clinostats and bioreactors.,” *Gravitational and space biology bulletin : publication of the American Society for Gravitational and Space Biology*, vol. 14, 2 2001.

[78] T. G. Hammond and J. M. Hammond, “Optimized suspension culture: The rotating-wall vessel,” *American Journal of Physiology - Renal Physiology*, vol. 281, 1 50-1 2001. DOI: 10.1152/ajprenal.2001.281.1.f12.

[79] R. P. Schwarz, T. J. Goodwin, and D. A. Wolf, “Cell culture for three-dimensional modeling in rotating-wall vessels: An application of simulated microgravity,” *Journal of Tissue Culture Methods*, vol. 14, 2 1992. DOI: 10.1007/BF01404744.

[80] NASA. “NASA Life Sciences Portal.” (), [Online]. Available: https://nlsp.nasa.gov/view/lsdapub/lsda_image/IDP-LSDA_IMAGE-0000000000001394 (visited on 01/20/2023).

[81] D. Grimm, M. Egli, M. Krüger, *et al.*, “Tissue engineering under microgravity conditions-use of stem cells and specialized cells,” *Stem Cells and Development*, vol. 27, no. 12, 2018. DOI: 10.1089/scd.2017.0242.

[82] H. C. Jo, J. H. Kim, and D. Y. Kim, “In vivo observing effects of the microgravity environment on zebrafish eyes using optical coherence tomography,” 2022. DOI: 10.1117/12.2608621.

[83] C. Lorin, R. J. A. Hill, and A. Mailfert, “Magnetic levitation,” in *Generation and Applications of Extra-Terrestrial Environments on Earth*, D. A. Beysens and J. J. W. A. van Loon, Eds., Ålborg: River Publishers, 2015, ch. 8, pp. 75–89.

[84] H. Sanavandi and W. Guo, “A magnetic levitation based low-gravity simulator with an unprecedented large functional volume,” *npj Microgravity*, vol. 7, 1 2021. DOI: 10.1038/s41526-021-00174-4.

[85] Y. Liu, D. M. Zhu, D. M. Strayer, and U. E. Israelsson, “Magnetic levitation of large water droplets and mice,” *Advances in Space Research*, vol. 45, 1 2010. DOI: 10.1016/j.asr.2009.08.033.

[86] J. Z. Kiss, C. Wolverton, S. E. Wyatt, K. H. Hasenstein, and J. J. van Loon, “Comparison of microgravity analogs to spaceflight in studies of plant growth and development,” *Frontiers in Plant Science*, vol. 10, 2019. DOI: 10.3389/fpls.2019.01577.

[87] R. Hemmersbach, A. Simon, K. Waßer, *et al.*, “Impact of a high magnetic field on the orientation of gravitactic unicellular organisms - a critical consideration about the application of magnetic fields to mimic functional weightlessness,” *Astrobiology*, vol. 14, 3 2014. DOI: 10.1089/ast.2013.1085.

[88] R. K. Globus and E. Morey-Holton, “Hindlimb unloading: Rodent analog for microgravity,” *Journal of Applied Physiology*, vol. 120, 10 2016. DOI: 10.1152/japplphysiol.00997.2015.

[89] H. W. Zhao, J. Zhao, L. N. Hu, *et al.*, “Effect of long-term weightlessness on retina and optic nerve in tail-suspension rats,” *International Journal of Ophthalmology*, vol. 9, 6 2016. DOI: 10.18240/ijo.2016.06.06.

[90] S. Li, Q. Song, B. Wu, *et al.*, “Structural damage to the rat eye following long-term simulated weightlessness,” *Experimental Eye Research*, vol. 223, 2022. DOI: 10.1016/j.exer.2022.109200.

[91] National Research Council (U.S.), *Recapturing a Future for Space Exploration: Life and Physical Sciences Research for a New Era*. Washington DC: National Academies Press, 2011. DOI: https://doi.org/10.17226/13048.

[92] E. R. Morey-Holton and R. K. Globus, “Hindlimb unloading rodent model: Technical aspects,” *Journal of Applied Physiology*, vol. 92, 4 2002. DOI: 10.1152/japplphysiol.00969.2001.

[93] T. J. Wronski and E. R. Morey-Holton, “Skeletal response to simulated weightlessness: A comparison of suspension techniques,” *Aviation Space and Environmental Medicine*, vol. 58, 1 1987.

[94] T. A. Knight, “On the direction of the radicle and germen during the vegetation of seeds,” *Philosophical Transactions of the Royal Society of London*, vol. 96, pp. 99–108, 1806. DOI: http://doi.org/10.1098/rstl.1806.0006.

[95] H. Davy, G. Sinclair, and J. R. Bedford, *Elements of agricultural chemistry, in a course of lectures for the Board of agriculture*. London: Longman, Hurst, Rees, Orme, and Brown, 1813. DOI: 10.5962/bhl.title.41216.

[96] H. J. Muller, “Approximation to a gravity-free situation for the human organism achievable at moderate expense,” *Science*, vol. 128, no. 3327, pp. 772–772, 1958. DOI: 10.1126/science.128.3327.772.a.

[97] T. Hoson, S. Kamisaka, Y. Masuda, and M. Yamashita, “Changes in plant growth processes under microgravity conditions simulated by a three-dimensional clinostat,” *The Botanical Magazine Tokyo*, vol. 105, no. 1, 1992. DOI: 10.1007/BF02489403.

[98] R. Huijser, “Desktop rpm: New small size microgravity simulator for the bioscience laboratory,” *Fokker Space*, August 2000.

[99] S. Kopp, L. Slumstrup, T. J. Corydon, *et al.*, “Identifications of novel mechanisms in breast cancer cells involving duct-like multicellular spheroid formation after exposure to the Random Positioning Machine,” *Scientific Reports*, vol. 6, 2016. DOI: 10.1038/srep26887.

[100] S. L. Wuest, S. Richard, I. Walther, *et al.*, “A novel microgravity simulator applicable for three-dimensional cell culturing,” *Microgravity Science and Technology*, vol. 26, 2 2014. DOI: 10.1007/s12217-014-9364-2.

[101] S. L. Wuest, S. Richard, S. Kopp, D. Grimm, and M. Egli, “Simulated microgravity: Critical review on the use of random positioning machines for mammalian cell culture,” *BioMed Research International*, vol. 2015, 2015. DOI: 10.1155/2015/971474.

[102] N. H. Wubshet, E. Arreguin-Martinez, M. Nail, *et al.*, “Simulating microgravity using a random positioning machine for inducing cellular responses to mechanotransduction in human osteoblasts,” *Review of Scientific Instruments*, vol. 92, 11 2021. DOI: 10.1063/5.0056366.

[103] M.-Z. Shao and N. Badler, “Spherical sampling by archimedes’ theorem,” 1996.

[104] A. G. Borst and J. J. Van Loon, “Technology and developments for the random positioning machine, RPM,” *Microgravity Science and Technology*, vol. 21, no. 4, 2009. DOI: 10.1007/s12217-008-9043-2.

[105] J. J. van Loon, “Some history and use of the random positioning machine, rpm, in gravity related research,” *Advances in Space Research*, vol. 39, pp. 1161–1165, 7 2007. DOI: 10.1016/j.asr.2007.02.016.

[106] S. Altaie, A. Alrawi, and D. Xuexin, “A novel model of gravity challenge device,” *Biomedical Signal Processing and Control*, vol. 85, 2023. DOI: 10.1016/j.bspc.2023.104911.

[107] S. M. Kim, H. Kim, D. Yang, *et al.*, “An Experimental and Theoretical Approach to Optimize a Three-Dimensional Clinostat for Life Science Experiments,” *Microgravity Science and Technology*, vol. 29, no. 1-2, 2017. DOI: 10.1007/s12217-016-9529-2.

[108] T. Y. Kim, “Theoretical study on microgravity and hypogravity simulated by random positioning machine,” *Acta Astronautica*, vol. 177, 2020. DOI: 10.1016/j.actaastro.2020.07.047.

[109] Y. J. Kim, M. H. Lim, B. Jeon, *et al.*, “Manufacturing and Control of a Robotic Device for Time-averaged Simulated Micro and Partial Gravity of a Cell Culture Environment,” *International Journal of Control, Automation and Systems*, vol. 18, no. 1, 2020, ISSN: 20054092. DOI: 10.1007/s12555-019-0238-7.

[110] A. Manzano, R. Herranz, L. A. D. Toom, *et al.*, “Novel, moon and mars, partial gravity simulation paradigms and their effects on the balance between cell growth and cell proliferation during early plant development,” *npj Microgravity*, vol. 4, 1 2018. DOI: 10.1038/s41526-018-0041-4.

A

Additional Acceleration Plots

A.1. Combined Time-Averaged Acceleration With Bias

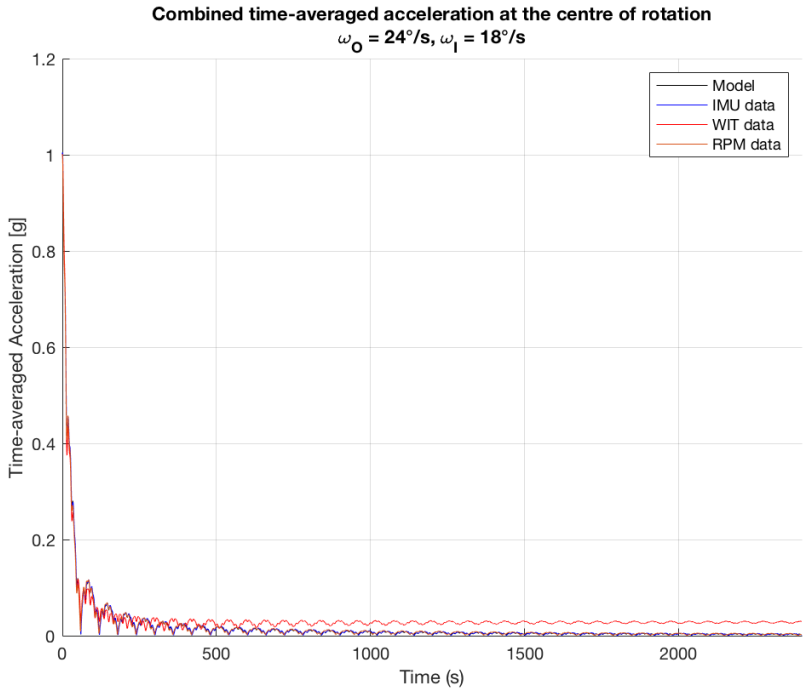

Figure A.1: The time-averaged acceleration without accounting for bias on the WIT sensor. The resulting g-level is averaging around $0.028g$ at the end of the run.

A.2. Time-averaged Acceleration in the Individual Directions

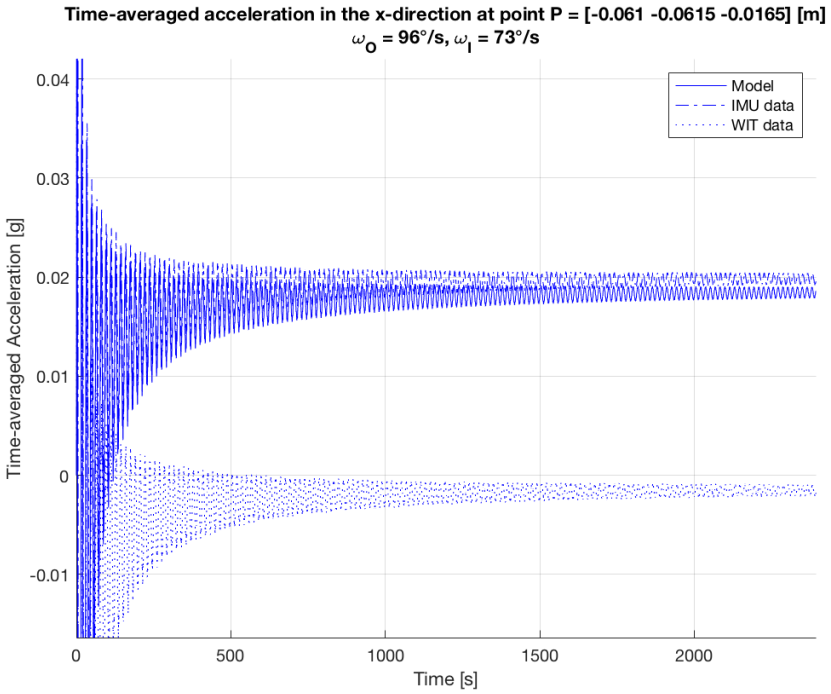

Figure A.2: The time-averaged acceleration in the x-direction at the corner location and rotational rates of ω_I = $73°s^{-1}$ and ω_O = $96°s^{-1}$.

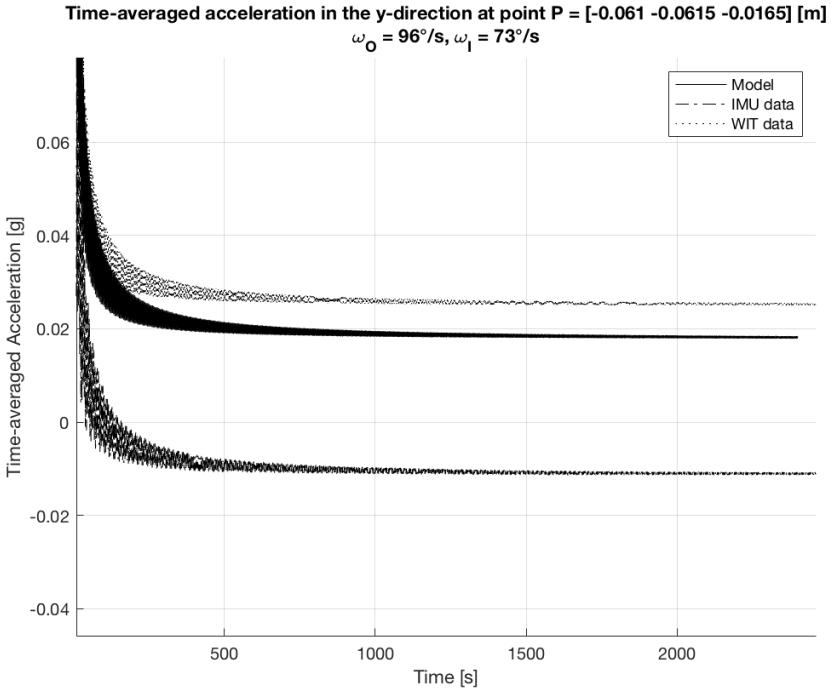

Figure A.3: The time-averaged acceleration in the y-direction at the corner location and rotational rates of ω_I = $73°s^{-1}$ and ω_O = $96°s^{-1}$.

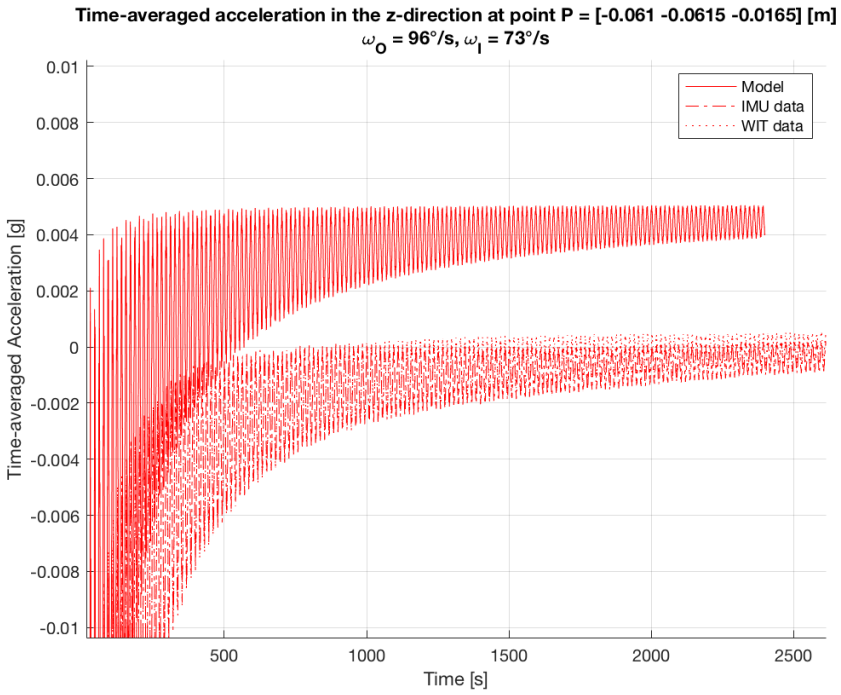

Figure A.4: The time-averaged acceleration in the z-direction at the corner location and rotational rates of ω_I = $73°s^{-1}$ and ω_O = $96°s^{-1}$.

A.3. Acceleration in the Individual Directions

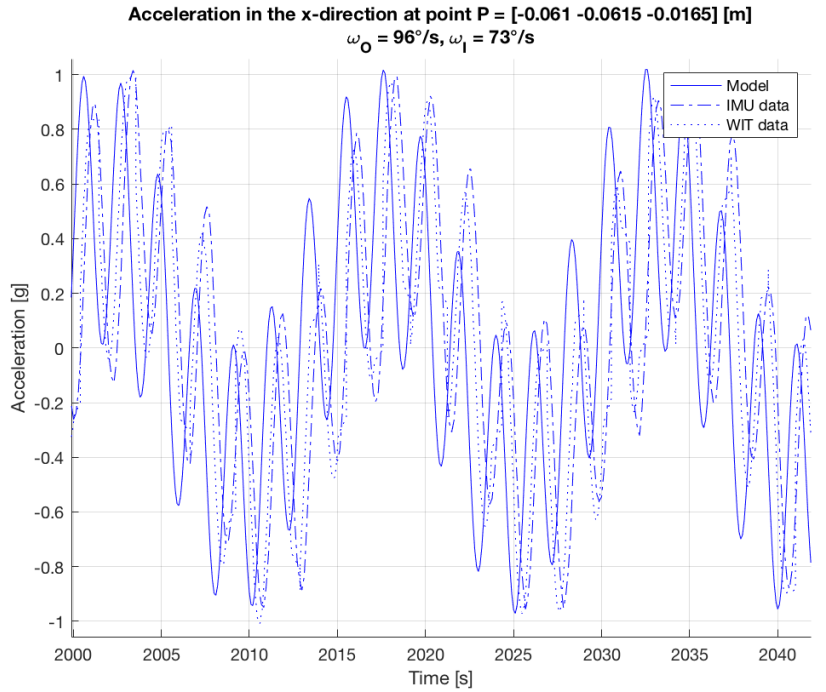

Figure A.5: Section of the measured acceleration in the x-direction at the corner location and rotational rates of ω_I = $73°s^{-1}$ and ω_O = $96°s^{-1}$.

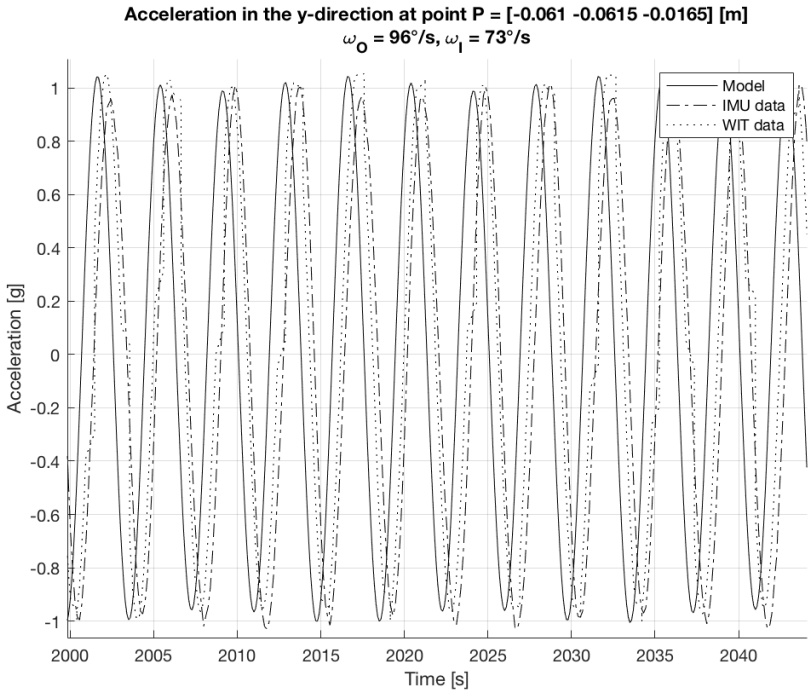

Figure A.6: Section of the measured acceleration in the y-direction at the corner location and rotational rates of ω_I = $73°s^{-1}$ and ω_O = $96°s^{-1}$.

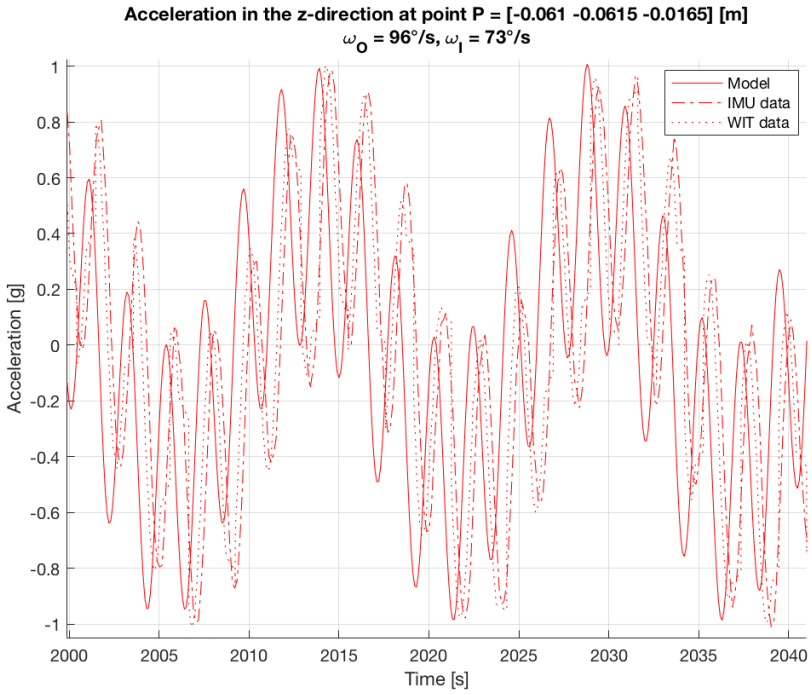

Figure A.7: Section of the measured acceleration in the z-direction at the corner location and rotational rates of ω_I = $73°s^{-1}$ and ω_O = $96°s^{-1}$.

A.4. Accelerations of the Alternative Model

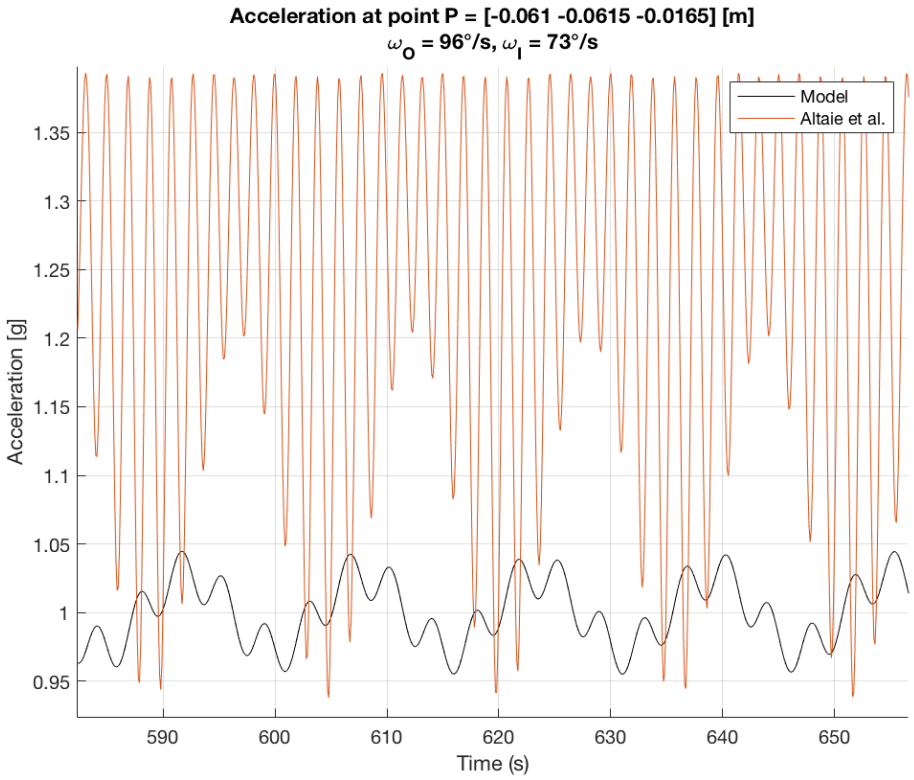

Figure A.8: Modelled g-level of the model presented in this thesis and the model presented in [106]. The modelled presented elsewhere cannot be used to investigate the accelerations in the RPM.

A.5. Time-Averaged acceleration of the sinusoidal control function

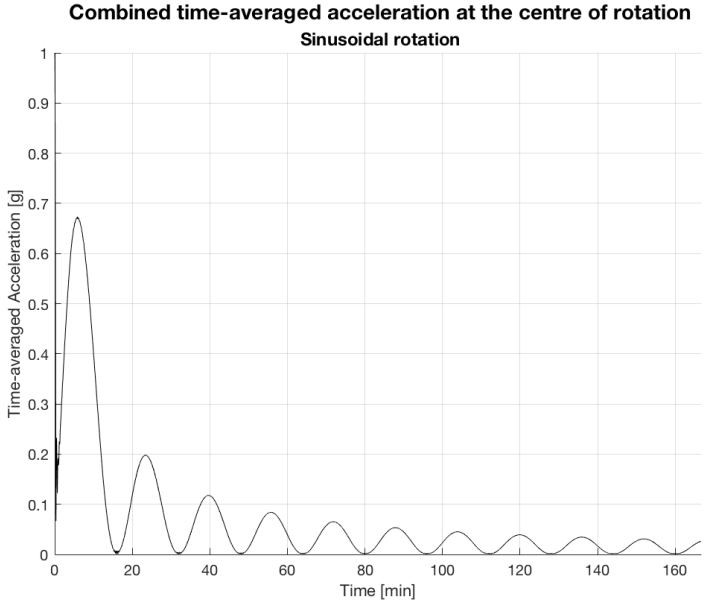

Figure A.9: Modelled g-level of the sinusoidal control algorithm. This approach shows large variations depending on the time.

B

Lowest Resulting g-Levels at Constant Rotation Rate

Table B.1: The lowest g-levels in the range of $1°s^{-1}$ to $50°s^{-1}$ after 25 min of a run.

Lowest g-levels		
ω_O [$°s^{-1}$]	ω_I [$°s^{-1}$]	**g-level** [g]
48	4	0.001393
48	5	0.001397
49	1	0.001382
49	3	0.001396
49	4	0.001371
49	5	0.001361
49	6	0.001352
49	7	0.001366
49	8	0.001399
50	1	0.001371
50	2	0.001386
50	3	0.001361
50	4	0.001345
50	5	0.001348
50	6	0.001343
50	7	0.001345
50	8	0.001360
50	9	0.001373
50	10	0.001387
50	13	0.001397
50	14	0.001399
50	17	0.001398
50	18	0.001399
50	19	0.001393